UNIVERSITÀ DEGLI STUDI DI PALERMO

Dottorato in Scienze Fisiche
Dipartimento di Fisica e Chimica
Settore Scientifico Disciplinare FIS/05

BROAD BAND SPECTRAL ANALYSIS AND X-RAY SPECTROSCOPY OF NEUTRON STAR LOW MASS X-RAY BINARIES

IL DOTTORE
Marco Matranga

IL COORDINATORE
Prof. Gioacchino Massimo Palma

IL TUTOR
Prof.ssa Tiziana Di Salvo

EVENTUALE CO TUTOR

CICLO XXIX
ANNO CONSEGUIMENTO TITOLO 2016/2017

Contents

Abstract

The main argument of this thesis concerned the spectroscopic, broad-band spectral analysis of X-ray binary systems hosting a neutron star, that accretes matter through an accretion disk, and a low mass companion star, with a mass less than 1 $M_{\odot}$; these systems are named Low Mass X-ray Binaries (hereafter LMXBs). In particular, the spectral study has been focused on the so-called reflection spectrum that is originated by the primary Comptonization spectrum that is intercepted and reprocessed by the cold matter on the surface of the accretion disk. The primary spectrum is originated very close to the neutron star by Inverse Compton scattering of low energy photons, characterized by a black-body distribution, coming from the surface of the neutron star and/or from the accretion disk.

The re-processed spectrum is thus composed by a continuum produced by Direct Compton of the primary spectrum (which is absorbed at lower energy by the photoelectric effect caused by the presence of cold atoms in the disk) and by the presence of emission lines and absorption edges due to the most abundant elements present in the disk. The most intense among these discrete features is the fluorescence Iron (Fe) line (at 6.4 - 6.95 keV, where the line energy of 6.4 keV corresponds to the emission from neutral Iron, while the 6.7 and 6.95 keV lines correspond to He-like and H-like Fe, respectively). This line has usually a large width, probably broadened by Doppler and (special and general) relativistic effects caused by the high-velocity of the plasma in the disk. Studying these features (as well as the entire reflection spectrum) can give important information on the matter in the inner accretion disk, such as the chemical composition and ionization state of the matter in the disk, the disk emissivity law, the inner and the outer radius of the disk and the inclination of the system with respect to the line of sight.

Since in these systems the accretion disk can extend up to very close to the compact object (in theory up to its surface) the analysis of such lines can provide an upper limit to the neutron star radius, that can be very important in order to

obtain constrains on the equation of state for ultra-dense matter. This research therefore fits into an important debate in the international scientific community because the results could potentially provide important information on the equation of state of neutron stars, which form the final stable state of matter, subject to strong gravitational and magnetic fields, before gravitational collapse into a black hole. The conditions of matter in such systems, which experiences the most intense magnetic and gravitational fields present in the Universe, are impossible to replicate in any laboratory on Earth, and provides therefore a fundamental tool able to investigate physics laws in extreme environments. It is worth noting that the spectral fitting performed in this thesis, with multiple spectral components and many parameters, are complex and the evaluation of the uncertainties in the fitting parameters requires large amount of computer time, up to a month, besides the fact that there is also the need to evaluate different models.

This PhD thesis is dedicated to the spectral study of a sample of properly chosen neutron star Low Mass X-ray Binaries (LMXB). The sources in the analyzed sample are 4U 1705-44 (observed during the hard state and over a broad band energy range by the Japanese satellite Suzaku), Serpens X-1 (observed during a soft state by the NASA satellite NuSTAR and by the ESA satellite XMM-Newton), and the transient source EXO 1745-248. The aim is the characterization of their broad-band X-ray spectrum with particular attention to spectroscopy of emission lines and of the so-called reflection spectrum.

In the case of 4U 1705-44 the broad-band ($0.5 - 200$ keV) spectrum was acquired with the Japanese X-ray observatory *Suzaku* with the aim of studing the reflection spectrum in this source during a hard state and to make a comparison of the derived spectral parameters with those obtained during the more luminous soft state of the source. We find that the reflection parameters are very similar in the two states of the source, the main difference being in the ionization parameters which is much higher during the soft state, as expected. Other parameters, such as the inclination angle of the system with respect to the line of sight or the inner disk radius, were instead very similar. In particular, the accretion disk in the hard state appears to be truncated at a radius comparable to that found during the soft state, indicating that the disk does not recedes significantly in the hard state, where the mass accretion rate is lower than in the soft state.

Serpens X-1 was observed with the NASA X-ray observatory NuSTAR ($3-200$ keV energy) during a high luminosity state, with the aim to fit its broad-band spectrum, derive the reflection parameters, and compare these with the results obtained by (Miller et al., 2013) who have analyzed the same data. (Miller et al.,

2013) found that fitting the NuSTAR spectrum with relativistically blurred disk reflection models suggest that the disk likely extends close to the innermost stable circular orbit (ISCO) or stellar surface. We have re-analysed these data together with XMM-Newton data from a previous observation of this source and fitted these spectra with slightly different continuum and reflection models with respect to those previously adopted for this source, yielding consistent spectral results for the NuSTAR and XMM-Newton spectra. Our results are less extreme with respect to those found by Miller et al. (2013). In particular, we find that the inner disk radius is relatively far form the ISCO, at $\sim$ 30 km from the neutron star center, in line with what is usually found for neutron star systems.

Finally, in collaboration with Dr. Alessandro Papitto at the Institute of Space Sciences in Barcelona (Spain), I have analyzed the high resolution and broad band spectra of EXO 1745-248, observed with the instruments on board of the ESA satellites XMM-Newton and INTEGRAL. The spectral analysis of this interesting source has shown the presence, at the same time, of narrow lines at 6.4 and 7.05 keV, identified as the Kα and Kβ transitions of neutral iron, together with a broad emission line at 6.7 keV, identifies as the Kα transition of He-like Fe, which appears broad and is probably produced by reflection off the inner accretion disk. Besides these complex iron emission lines, we also detect the presence of broad low-energy emission lines, identified as Kα transitions of SXVI, ArXVII and CaXIX-XX. The analysis has shown that there are at least two different emission regions in this source: one with weakly ionized plasma that produces the narrow features, and the other strongly ionized that produces the broad features which is likely localized at the inner edge of the accretion disk. For this source, as well as for the other two sources of our sample, we have performed a detailed spectral analysis, the X-ray spectra of these sources have been fitted using both phenomenological models (where the emission lines are modelled either with Gaussians or Disklines) and with self-consistent reflection models, although in the case of EXO 1745-248 the analysis has been complicated by the presence of additional discrete features in the final best-fit model.

The main results of the spectral and analysis of the three sources of our sample, together with a discussion of these results, are described in details in the main chapters of this thesis.

Chapter 1

Fundamental Physics of Accretion

Between one-third and two-thirds of all stars are in binary stellar systems. In such a system, two stars are gravitationally bound to each another. For the nineteenth century physicists, gravity was the only conceivable source of energy in celestial bodies, but gravity, through the so-called KelvinHelmholtz contraction mechanism, was inadequate to power the Sun for its known lifetime. Indeed the true source of the Sun's energy remained uncertain until the 1930s, when it was shown by Hans Bethe to be due to nuclear fusion of Hydrogen into Helium in its core. In contrast, at the beginning of the twenty-first century it is to gravity that astronomers look to power the most luminous objects in the Universe, for which the nuclear sources of the stars are wholly inadequate. The extraction of gravitational potential energy from material accreting on to a gravitating body is now known to be the principal source of power in several types of close binary systems. This increasing recognition of the importance of accretion has accompanied the dramatic expansion of observational techniques in astronomy, in particular the exploitation of the full range of the electromagnetic spectrum from the radio to X-rays and gamma-rays. At the same time, the existence of compact objects has been placed beyond doubt by the discovery of the pulsars, which are rotating neutron star (hereafter NS) with a dipole magnetic field misaligned with its rotation axis, and by the discovery of binary systems in which the compact object has a mass exceeding the limiting mass for a NS, which confirmed the existence of the so-called black holes. Thus, the new role for gravity arises because accretion on to compact objects is a natural and powerful mechanism for producing X-rays radiation (see e.g. Fig. 1.1).

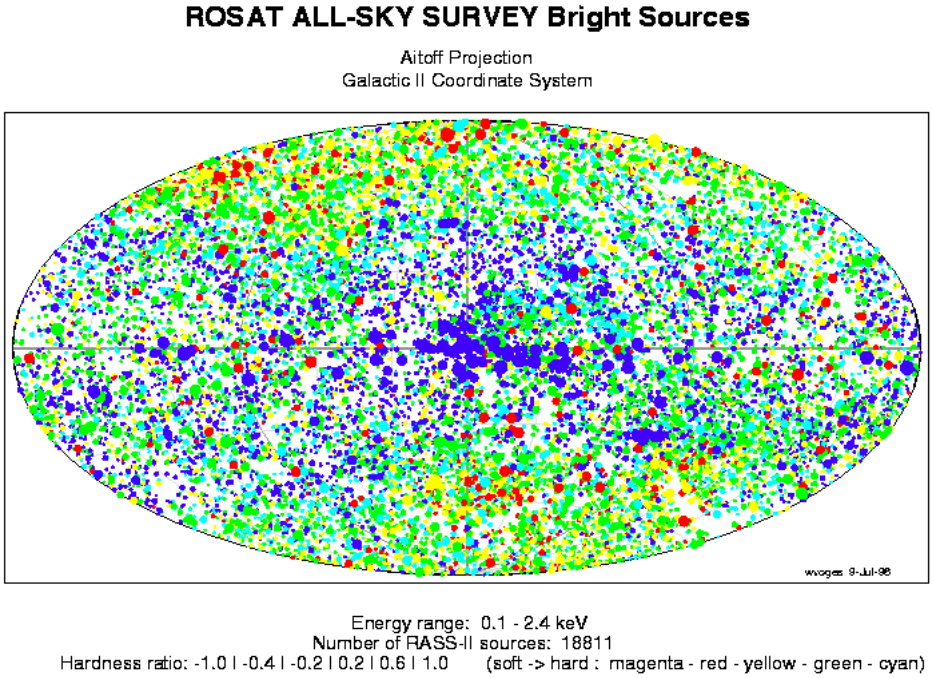

Figure 1.1: Colored dots show the X-ray Bright Source Catalogue of the ROSAT All-Sky Survey in Galactic coordinates Voges et al. (1999)

1.1 Efficiency of Accretion

Accretion of matter onto objects is an efficient and natural mechanism to explain the x-ray emission of objects among the most luminous in the Galaxy. For an object of mass M and radius R, the gravitational potential energy released at its surface by the accretion of a test mass m from a large distance is: $\Delta E_{acc} = GMm/R$, where G is the gravitational constant. It is then emitted as radiation with a luminosity: $L_{acc} = GM\dot{M}/R$, where $\dot{M}$ is the accretion rate. The accretion luminosity can be written in terms of rest energy of the accreted matter as: $L_{acc} = \eta\dot{M}c^2$, where c is the speed of light and $\eta = GM/Rc^2$ is the efficiency of the conversion of accreted mass into luminous energy. Therefore the efficiency depends on the ratio between the mass and the radius that is usually called 'compactness' of the accreting object. In the case of a NS, using typical values $R = 10^6$ cm, $M = 1.4M_\odot$, we obtain an efficiency of about 0.1. For comparison the efficiency of a thermonuclear fusion reaction is only about 0.007, about 1/20 that of accretion onto a NS.

1.2 Mass Transfer in Binary Systems

The effective gravitational potential in a binary system is determined by the masses of the stars and the centrifugal force arising from the motion of the two stars around one another. In order to simplify the problem, we introduce a Cartesian reference frame centered on star 1 and rotating with star 2, with an orbital separation, 'a'. One may write this potential as:

$$\Phi = -\frac{GM_1}{r_1} - \frac{GM_2}{r_2} - \frac{\Omega^2 r_3^2}{2} \tag{1.1}$$

where $r_1 = \sqrt{x^2 + y^2 + z^2}$ and $r_2 = \sqrt{(x-a)^2 + y^2 + z^2}$ are the distance to the center of the stars with mass M_1 and mass M_2, respectively. Moreover Ω is the angular velocity of rotation about the center of mass whereas r_3 is the distance of the rotational axis of the binary from the reference frame. Now, we assume the they are in a circular orbit. This is usually a good approximation, as tidal effects tend to circularize their orbits and bring the two stars into synchronized co-rotation in relatively small time. With this assumptions we have $\Omega = \sqrt{GM/a^3}$.

In this way we obtain the equipotential surface shown in Fig 1.4. The largest closed equipotential surface around each star is called Roche lobe, whereas the point of intersection of the the two Roche lobes is called inner Lagrangian point, L_1. Lagrangian points are those in which the effective force (gravity plus centrifugal) vanishes. Because the effective force vanishes at L_1, if one of the stars fills its entire Roche lobe the pressure gradient will push the gas through L_1 into the Roche lobe of the companion, originating a mass transfer phase.

During the evolution of a binary system, there are many causes for which matter starts to flow through the inner Lagrangian point, starting the processes called *Roche Lobe Owerflow - RLO*. One of these is the evolution of one of the stars of the binary which leaves the main sequence. Fig. 1.2 shows the evolutionary tracks in the Hertzsprung-Russell diagram for six different values of the star mass: 1, 2, 5, 12, 20, 50 $M_\odot$. (Tauris and van den Heuvel, 2006) these tracks being calculated using Eggleton's evolutionary code (e.g., (Pols et al., 1995, 1998). The observable stellar parameters are the radius R, the effective surface temperature T_{eff}, and from these the luminosity is derived: $L = 4\pi R^2 \sigma T_{eff}^4$ were σ is the Stefan-Boltzmann constant. Fig. 1.3 shows a calculation of the stellar radius as a function of age for the particular case of a 5 $M_\odot$ star (Tauris and van den Heuvel, 2006). Important evolutionary stages are indicated in the figures. Between points 1 and 2 the star is in the long-lasting phase of core hydrogen burning (nuclear timescale). At point 3 hydrogen ignites in a shell around the helium core. For

stars more massive than 1.2 $M_\odot$ the entire star briefly contracts between points 2 and 3, causing its central temperature to rise. When the central temperature reaches about 10^8 K, core helium ignites (point 4). At this moment the star has become a red giant, with a dense core and a very large radius. During helium burning it describes a loop in the H-R diagram. Stars with $M \geq 2.3\ M_\odot$ move from point 2 to 4 on a thermal timescale and describe the helium-burning loop on a (helium) nuclear timescale following point 4. Finally, during helium shell burning the outer radius expands again and at carbon ignition the star has become a red supergiant on the asymptotic giant branch (AGB).

Usually a star born in a close binary system with a radius smaller than that of its Roche lobe, either because of expansion of its envelope at a later evolutionary stage or because the binary shrinks enough as a result of orbital angular momentum losses, may begin RLO. The further evolution of the system will now depend on the evolutionary state and structure of the donor star at the start of the overflow, which is determined by the mass of the donor and the distance between the two component, *a*. Kippenhahn and Weigert (1990) defined three types of RLO: case A, when the system is so close that the donor star begins to fill its Roche lobe during core-hydrogen burning; case B when the primary star begins to fill its Roche lobe after the end of core-hydrogen burning but before helium ignition; and finally case C when it overflows its Roche lobe during helium shell burning or beyond.

Fig. 1.3 shows clearly that cases B and C occur over a wide range of radii (or orbital periods); case C even up to orbital periods of about 10 years. The precise orbital period range for cases A, B and C depend on the initial donor star mass and on the mass ratio. Once the RLO has started it continues until the donor has lost its hydrogen-rich envelope (typically > 70 % of its total mass) and subsequently no longer fills its Roche lobe. Generally, accretion disc forms because, falling on a central object matter always has some angular momentum, so it cannot accrete directly unless, in someway, gets rid of it. As a result, matter settles into a flat rotating configuration, or a disc. After settling into a disc shape, accretion primarily proceeds through such a disc by redistribution of angular momentum. In fact the matter nearer the central object falls onto its surface giving up angular momentum to outer parts of the disc. During this process the disc spreads, because a small amount of matter will carry all the angular moment outwards, while the rest of the mass, losing angular momentum, falls onto the compact star (Papaloizou and Pringle, 1977; Lin and Papaloizou, 1979).

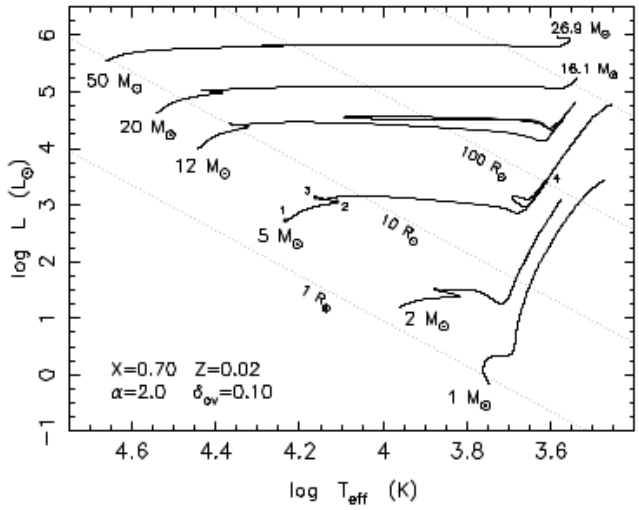

Figure 1.2: Stellar evolutionary tracks in the H-R diagram.

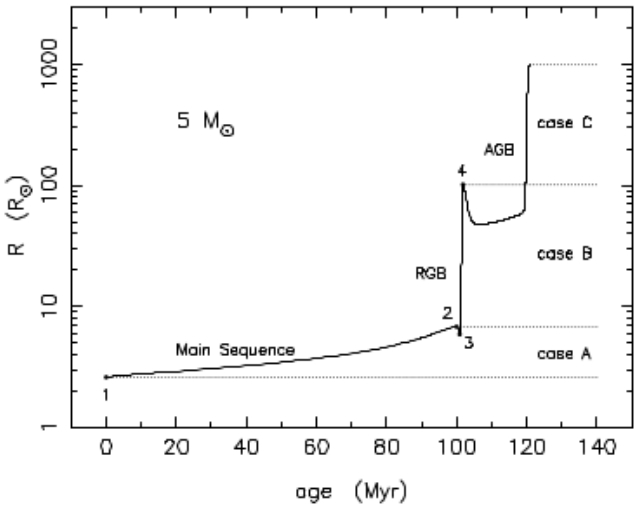

Figure 1.3: Evolutionary change of the radius of the 5 $M_\odot$ star shown in Fig.1.2. The range of radii for mass transfer to a companion star in a binary system according to RLO cases A, B and C are indicated (see text).

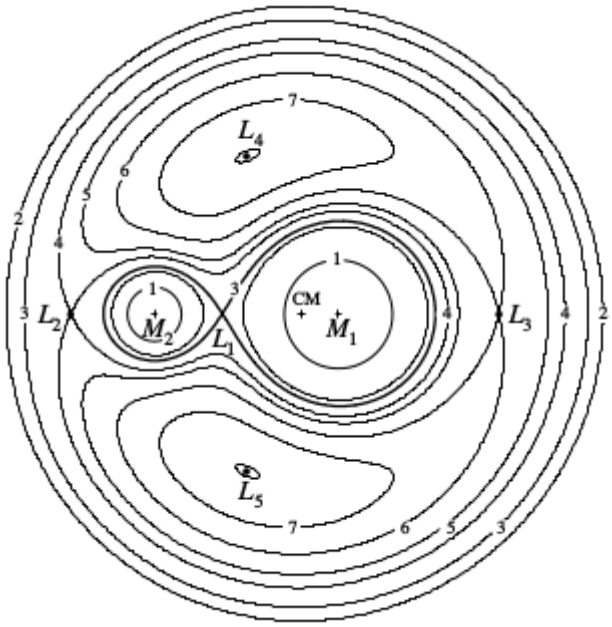

Figure 1.4: Sections in the orbital plane of the Roche equipotential surfaces. The figure also shows the Roche lobes, the center of mass (CM) of the system and the 5 Lagrangian points. (from King et al. 1985).

1.3 The Eddington Limit

For a given value of mass and radius of a star the luminosity of the system depends on the acctretion rate $\dot{M}$, but it cannot grow indefinitely. In fact at high luminosities the accretion rate can be reduced by the large radiation pressure: the photons emitted by the source interact with the infalling matter through processes of scattering and absorption, resulting in an upper limit on the luminosity of these systems. This limiting luminosity, the Eddington luminosity, is now derived for steady state and spherical accretion of matter consisting of protons and electrons. The radiation emitted by the central source interacts mostly with electrons by Thomson scattering. At the Eddington limit, the radiation pressures is balanced by the gravitational force exerted on the protons, $GMm_p/R^2 = L_{Edd}\sigma_T/(4\pi R^2 c)$, where R is the distance to the stellar center and σ_T is the Thomson scattering cross section. The Eddington limit is therefore:

$$L_{Edd} = 4\pi GMm_p c/\sigma_T \simeq 1.3 \times 10^{38}\, M/\mathrm{M}_\odot erg/s \tag{1.2}$$

.

The Eddington luminosity sets an upper limit to the luminosity of an accreting compact object since for $L >> L_{Edd}$ further accretion of matter will be inhibited

by the radiation pressure, although super-Eddington luminosities are sometimes observed. These can be due either to a sudden increase of accretion rate or to a non-spherical geometry. Also note that the Eddington limit can be increased by the presence of a strong magnetic field, because of the reduction of the scattering cross section (e.g., Herold, 1979)

We can then calculate the blackbody temperature corresponding to emission from the NS surface at the Eddington luminosity, which is ~ 2 keV. This temperature is indeed a lower limit to the temperature of the system, given that the blackbody is the most efficient emission mechanism. Note that it is in the X-ray range, so we expect that binary systems containing compact objects will emit most of the accretion energy in the X-ray range.

1.4 X-ray Binaries

X-ray binary systems consist of two objects: a compact object (black hole or neutron star) and a companion star, which both orbit the center of mass of the system. The X-ray emission originates from the conversion of the gravitational energy of the accreted matter into luminosity, through viscous processes or shocks occurring in the accretion disk. Depending on the mass of the companion star, X-ray binaries are classified as low-mass X-ray binaries or high-mass X-ray binaries (hereafter LMXBs or HMXBs, respectively). In LMXB, the secondary has a mass $< 1\,M_\odot$ and the matter is accreted onto the compact object through Roche lobe overflow and via an accretion disk. Whereas for HMXBs, the secondary has a mass $> 1\,M_\odot$ and the matter is mainly accreted via a stellar wind. Fig. 1.5 shows a sketch of typical configuration for both classes of binary systems.

1.4.1 LMXBs

Most of the LMXBs are located in the Galactic bulge and in globular clusters, and thus appear to belong to an old stellar population. Orbital periods have been measured for $30 - 40$ of these systems. They range from 11 minutes to 17 days. The emission from these systems are sometimes characterized by sudden increase of luminosity, called type-I X-ray bursts, that are due to thermonuclear fusion of accreted matter at the surface of the neutron star. The bursting activity is related to the strength of the magnetic field, as for $B > 10^{11}$ G the bursting activity usually stops (Lewin and Joss, 1983). Typical values of magnetic field are relatively low for LMXBs, $\sim 10^9 - 10^{11}$ G. This is due to the fact that they are old binaries, and have time to dissipate the magnetic field during their accretion

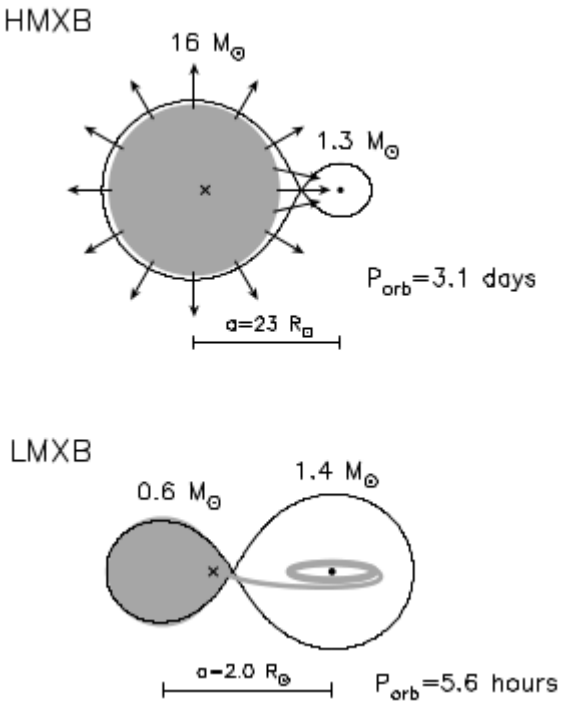

Figure 1.5: Examples of a typical HMXB (top) and LMXB (bottom). The neutron star in the HMXB is fed by a strong, high-velocity stellar wind and/or by a Roche-lobe overflow. The neutron star in an LMXB is surrounded by an accretion disk which is fed by Roche-lobe overflow.

induced activity (Taam and van den Heuvel, 1986), (Geppert and Urpin, 1994), Konar and Bhattacharya (1997), Cumming et al. (2001a).

An LMXB system can be formed by two different paths: either the binary may be formed by capture of a second star, or the two stars may be gravitationally bound from birth. In the second case, the more massive star evolves faster to reach the giant phase, during which a large portion of its envelope is either transferred to the companion, lost from the binary as the companion spirals in, or lost from the binary by stellar wind. Then, it undergoes a supernova explosion. If less than half of the binary mass is lost in this extremely violent event, the binary survives. In the opposite case, the binary can only survive if a kick velocity from the explosion happens in the right direction. In conclusion, if the binary system survives the supernova explosion, the system remains bound, and contains the new-born compact object and the companion star. In the first case, a massive star lives alone and becomes a compact object. Because of a high star density environment, a star can be captured (in a close encounter). This happens mainly in globular clusters. However, the vast majority of the binaries which exist in our Galaxy must have been born in a bound state.

1.4.2 HMXBs

There are 40 pulsating HMXB sources with typical pulse periods between 10 and 300 seconds (the entire observed range spans between 0.069 seconds and more than 20 minutes). They are characterized by a hard X-ray emitted spectrum ($kT > 15$ keV). The X-ray and/or optical light curves are characterized by the occurrence of regular X-ray eclipses and double-wave ellipsoidal light variations produced by tidally deformed (pear-shaped) giant or sub-giant companion stars with masses $> 10\,M_{\odot}$. Fig. 1.6 shows a sketch of a HMXB containing an X-ray pulsar, and in Tab. 1.1 the most important differences between HMXB and LMXB systems are reported.

Table 1.1: Classification of NS X-ray binaries

Properties	HMXBs	LMXBs
Donor star	O-B ($M > 5\mathrm{M}_\odot$)	K-M or WD ($M < 1\mathrm{M}_\odot$)
Population	I (10^7 yr)	II (5–15 $\times$ 10^9 yr)
$\mathrm{L}_X/\mathrm{L}opt$	0.001 - 10	100 - 1000
Optical spectrum	stellar-like	reprocessing
Accretion disk	sometimes, small	yes
X-ray spectrum	hard ($kT > 15$ keV)	soft ($kT < 10$ keV)
Orbital period	$1 - 100$ days	0.069 seconds - 10 days
X-ray eclipse	common	rare
Magnetic field	strong ($\approx 10^{12}$) G	weak (10^8–10^9) G
X-ray pulsations	common (0.1–1000 sec)	rare (0.1–100 sec)
Type-I X-ray burst	absent	common
X-ray QPOs	rare (0.001–1 Hz)	common (1–1000 Hz)

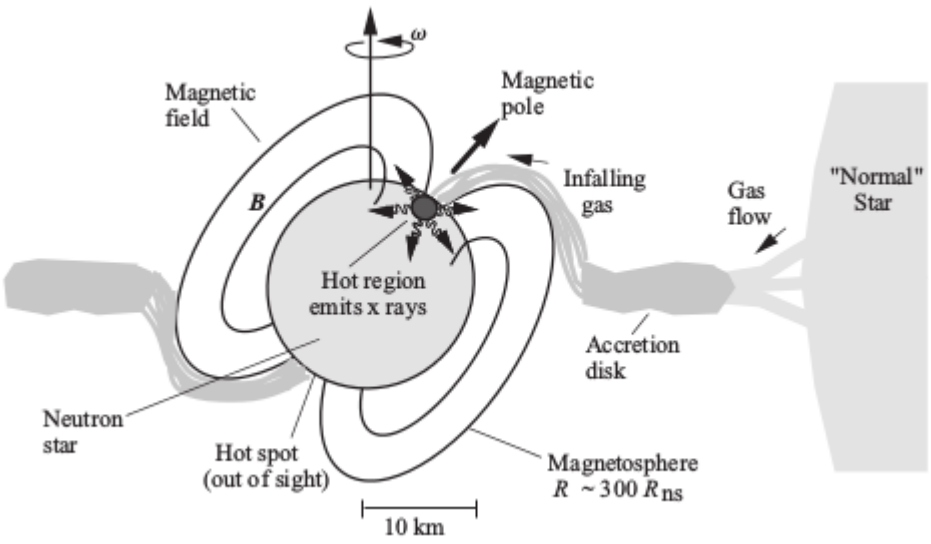

Figure 1.6: High-mass x-ray binary with X-ray pulsar. Gaseous matter accretes from the large normal star, 10^9 m, to the compact neutron star, size of about 10^4 m. The gas accumulates in an accretion disk and eventually is guided to the magnetic pole of the neutron star by the strong magnetic field. The hot region on the star is seen as a pulsing source as it comes into and out of sight while the neutron star rotates.

Chapter 2

Spectral characteristics of X-ray binary systems

2.1 Introduction

Several strong X-ray sources have been established to be in binary systems with objects more massive than the maximum mass from a neutron star, which is $\approx 3M_{\odot}$ (Kalogera and Baym, 1996), these are black-hole candidates (hereafter BH). Unfortunately for many X-ray binary systems the mass determination is difficult or impossible, because this measurement is only possible when the optical counterpart is observed. Thus some other methods have been proposed to identify systems containing BHs based on X-ray observational properties. Some arguments are based on the X-ray spectra of accreting BH, which are often very similar to the spectra of LMXBs containing a weakly magnetized neutron star.

In fact, as NS/LMXBs, galactic BH candidates exhibit at least two spectral states. The first state called 'soft/high state' dominated by thermal emission at $\approx 1-2$ keV, probably emitted by the accretion disk, together with a steep power law tail (with photon index $\alpha = 2-3$), and a second state, called 'hard/low state' where the accretion disk thermal emission is lower (0.1-0.5 keV) and the power-law tail is much harder (with photon index $\alpha \approx 1.7$), so it dominates the total emission from the source. This hard power law shows an esponetial cutoff at temperature of $\approx$ 100keV and it is generally interpreted as emission due to the thermal Comptonization of soft photons in a hot electron gas close to the compact object. It has been proposed that, in the framework of the thermal Comtonization model, the electron temperature of the scattering cloud, kT_e should be systematically lower for NSs than for BHs, and in fact typical values found for NS are $kT_e^{NS} < 20$ keV whereas for BHs they are $kT_e^{BH} > 50$

keV (Tavani et al., 1997; Churazov et al., 1997). This might be a consequence of the additional cooling provided by the NS surface which emits soft X-ray photons and regulates the maximum temperature achievable in these systems (Kluzniak, 1993; Sunyaev and Titarchuk, 1989).

Therefore spectral studies may be important to distinguish between systems containing BH or NS as compact object. In the following sections we give an overview of the spectral characteristics of NS/LMXBs, enlightening when possible the differences with respect to systems containing stellar mass BH.

2.2 Spectral/temporal Classification of Low Mass X-ray Binaries

The modern classification of NS LMXBs relies upon the branching displayed by individual sources in the X-ray color-color diagram (CD) assembled by using the sources' count rate over a classical X-ray energy range (typically 2-20 keV). This classification has proven very successful in relating the spectral and time variability properties (Hasinger and van der Klis, 1989a; van der Klis, 2000) of these systems, based on the pattern described by each source in the X-ray CD. It comprises a Z-class (sources luminosity close to the Eddington limit, L_{Edd}) and the the so-called atoll class (with luminosity usually well below the Eddington limit, L_{Edd}). Most atolls emits Type-I bursts that are thermonuclear flashes in the layers of freshly accreted material onto the neutron star surface. Considerable evidence has been found that the mass accretion rate (but not necessarily the X-ray luminosity) of individual Z-sources increases from the top left to the bottom right of the Z pattern (Hasinger et al., 1990), i.e. along the so called horizontal, normal and flaring branches (hereafter HB, NB, and FB, respectively; see Fig. 2.1). Similarly, in atoll sources the accretion rate increases from the so-called island to the top of the upper-banana branch.

2.3 The X-ray Broad-band Spectrum

X-ray spectra emitted by Low Mass X-Ray Binaries (LMXBs) of the atoll class (Hasinger and van der Klis, 1989a) are usually characterized by two states of emission: the soft and the hard state. During soft states the spectrum can be well described by a soft thermal component, usually a blackbody or a disk multi-color blackbody, possibly originated from the accretion disk, and a harder component, usually a saturated Comptonization spectrum. In some cases, a hard power-law

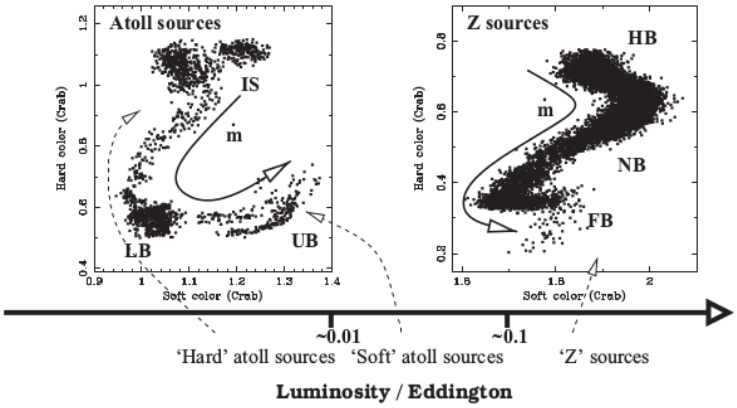

Figure 2.1: Color-color diagrams (CDs) associated with atoll sources (left panel) and Z sources (right panel). The arrow at the bottom indicates the increasing mass accretion rate direction. Two states are defined for atoll sources, the island state (IS) and the banana state (LB, Lower Banana, and UB, Upper Banana), corresponding to hard and soft states, respectively. As for Z sources, three branches are distinguishable: the horizontal branch (HB), the normal branch (NB), and the flaring branch (FB)

.

tail has been detected in the spectra of these sources during soft states both in Z sources (Di Salvo et al., 2000a), and in atoll sources (e.g., Piraino et al., 2007), usually interpreted as Comptonization off a non-thermal population of electrons. On the other hand, during hard states the hard component of the spectrum can be described by a power law with high energy cutoff, interpreted as unsaturated Comptonization, and a weaker soft blackbody component (e.g., Di Salvo et al., 2015a). The hard component is generally explained in terms of inverse Compton scattering of soft photons, coming from the neutron star surface and/or the inner accretion disk, by hot electrons present in a corona possibly located in the inner part of the system, surrounding the compact object (D'Aì et al., 2010a).

In addition to the continuum, broad emission lines in the range 6.4-6.97 keV are often observed in the spectra of LMXBs (see e.g. Cackett et al., 2008; Pandel et al., 2008a; D'Aì et al., 2009a, 2010a; Iaria et al., 2009; Di Salvo et al., 2005a, 2009a; Egron et al., 2013a; Di Salvo et al., 2015a). These lines are identified as Kα transitions of iron at different ionization states and are thought to originate from reflection of the primary Comptonization spectrum over the accretion disk. These features are powerful tools to investigate the structure of the accretion flow close to the central source. In particular, important information can be inferred from the line width and profile, since the detailed profile shape is determined by the ionization state, geometry and velocity field of the emitting plasma (see

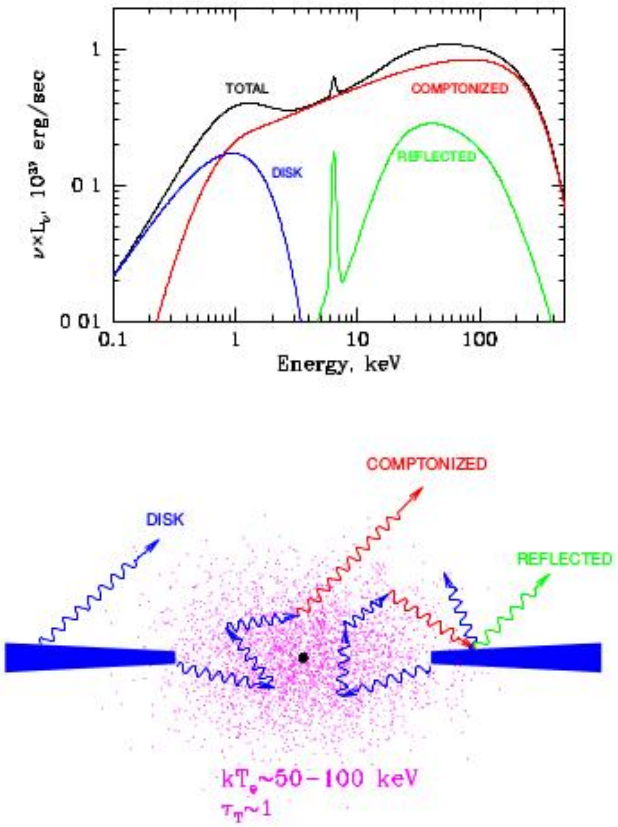

Figure 2.2: Schematic plot of the interactions between the disk and the corona

e.g. Fabian et al., 1989). Indeed, when the primary Comptonization spectrum illuminates a colder accretion disk, other low-energy discrete features (such as emission lines and absorption edges) are expected to be created by photoionization and successive recombination of abundant elements in different ionizations states as well as a continuum emission caused by direct Compton scattering of the primary spectrum off the accretion disk. All these features together form the so-called reflection spectrum, and the whole reflection spectrum is smeared by the velocity-field of the matter in the accretion disk.

2.4 The 'Hard-Tail' in Low Mass X-ray Binary Spectra

Hard X-ray components estending up to energies of several hundreds of keV, have been revealed in about 20 NS LMXBs of the atoll class. In these systems the

power-law like component, with a typical slope of $1.5-2.5$, is followed by an exponential cutoff, the energy of which is often between ≈ 20 and many tens of keV. This component is interpreted in terms of unsaturted thermal Comptonisation. There are instances in which no evidences for a cutoff is found up to 100-200 keV. This is the so called 'the hard state' of atoll sources, and it is similar to the hard state of BH systems. There are sources that appear to spend most of the time in this state (Piraino et al., 1999). In others a gradual transition from the soft to the hard state has been observed in response to a decrease of the luminosity and/or the source drifting from the banana branch to the island state. This transition is often modelled in terms of gradual decrease of the electron temperature of the Comptonising region.

As first noted by van Paradijs and van der Klis (1994), there is a clear trend for the spectral hardness of these sources over the ranges $13-25$ keV and $40-80$ keV to be higher for lower X-ray luminosities. This is in agreement with the observation that Z-sources usually show much softer X-ray spectra with characteristic temperature of $3-6$ keV. The first detection of a hard component in Z-source was in Sco X-1 (Peterson and Jacobson, 1966). More recently, a hard tail component has been detected in GX 17+2 (Di Salvo et al., 2000a), GX349+2 (Di Salvo et al., 2001b), Cyg X-2 (Di Salvo et al., 2001b), as well as in the peculiar bright LMXB Cir X-1 (Iaria et al., 2001, 2002) and during type II bursts on Rapid Buster (Masetti et al., 2000). The fact that a similar hard component has been observed in several Z sources indicates that this is a common feature for these binaries. This hard component can be fitted by a power law with photon index in the range $1.9-3.3$ and contributes up to $\sim 10\%$ of the bolometric luminosity. The presence of the hard tail is related to the position in the CD plot. (Di Salvo et al., 2000b) have showed that in the case of GX 17+2 the hard component (a power-law with index of 2.7) showed the strongest intensity in HB and a factor of ~ 20 decrease when the source moved from HB to NB (i.e. from low to high accretion rate).

The origin of this hard-tail in spectra on NS binaries is still poorly understood. In BH the steep power-law was interpreted in terms of Comptonization in a converging bulk flow in the vicinity of the event horizon. Close to the event horizon, the strong gravitational field is expected to dominate the pressure forces, and this will result in a free fall of the accreting material into the BH. The inverse Componization of the low energy photons from fast moving electrons should produce the steep power-law with photon index ≈ 2.5, mostly determined by values of mass accretion rate typical of BH in hard state (Titarchuk et al., 1997;

Titarchuk and Zannias, 1998). On the contrary, for other compact objects the pressure forces are dominant close to their surfaces and therefore a free fall state should be absent. However, the observation of hard power-law components in bright NS system, contradicts this expectation. (Di Salvo et al., 2000b), suggest to prefer models which do not rely on the presence of the event horizon of BH. They prefer the interpretation of the hard power-law as non thermal Componization, probably on fast moving electrons that are part of an outflow or a jet.

In the following sections we give same basic description of the most important spectral components used for the spectral modeling of the sources analysed in this thesis.

2.5 Interstellar Absorption

Due to the interstellar medium the radiation that we collect in our detector is attenuated as the photons undergo photoelectric absorption by an atom or an ion. Since the absorption cross section depends on the atomic number of the elements as Z^{4-5}, heavier element contributions to the total absorption cross section is more significant at X-ray energies, even though they are less abundant than hydrogen. The photoelectric absorbing cross section is given by (Heitler, 1954):

$$\sigma_i = 4\sqrt{2}\sigma_T \alpha^4 Z^5 \frac{m_e}{h\nu} \tag{2.1}$$

where α is the fine structure constant and σ_T is the Thomson cross section.

The absorption coefficient, obtained adding the contributions from all ions, is then:

$$\zeta_{TOT} = N_H \Sigma_i \frac{N_{Zi}}{N_H} \sigma_i(\omega) \tag{2.2}$$

The attenuation of intensity due to a slab of thickness x is:

$$I(x) = I_0 \exp^{(-x\zeta_{TOT})} \tag{2.3}$$

The exponent is therefore proportional to the hydrogen density multiplied by the distance travelled by X-ray light to the observer. The value $N_H x$ is called equivalent hydrogen column density and is the usual quantity used to parametrize X-ray extinction due to photoelectric absorption in astrophysical sources.

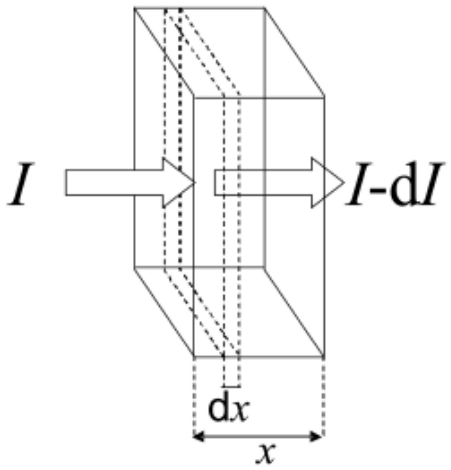

Figure 2.3: Attenuation of Intensity due to a slab of thickness x

2.6 Black-body Component

A photon gas in perfect thermal equilibrium with its surroundings at some temperature T will exhibit an energy spectrum of a specific shape known as the blackbody spectrum:

$$\rho(\nu) = \frac{2h\nu^3}{c^2}\frac{1}{e^{h\nu/k_BT-1}} \tag{2.4}$$

From this the Stefan-Boltzman Law can be derived:

$$F(T) = \int \rho_\nu(T)d\nu = \sigma T^4 \tag{2.5}$$

where σ is 5.67 $\times 10^{-5}$ ergs cm^{-2} sec^{-1} K^{-4}.

In some cases, the disk X-ray emission can be described by the so-called multi-color disk blackbody model. Generally the disk is optically thick, that means that photons undergo many interactions before exiting the emission region. Moreover, since matter is in thermal equilibrium, it will reach a well defined temperature T. Every element of the disk will emit as a blackbody with a temperature distribution depending on the distance R from the center.

Generally, the standard disk model adopted for LMXBs is the so-called alpha disc of Pringle and Rees (1972) and Shakura and Sunyaev (1973), where heating is produced by viscosity. In this case, considering that the accretion luminosity is given by $L_{acc} = \frac{d}{dt}(\Delta E_{acc}) = \frac{GM\dot{M}}{R}$, it is easy to show that the temperature profile in the disk as a function of its radius is

$$T(r) \approx r^{-3/4} \tag{2.6}$$

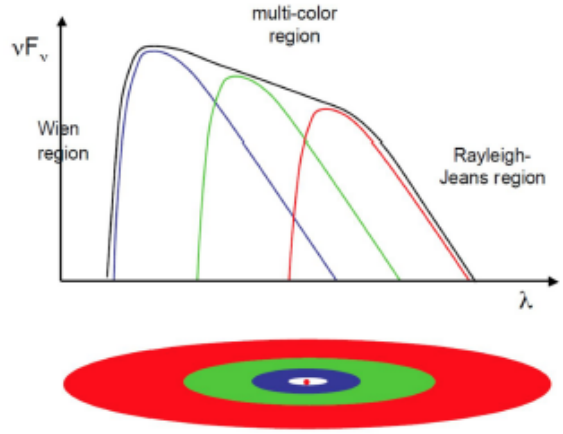

Figure 2.4: Different contributions as a function of the radius for a multicolor disk blackbody model.

meaning that the temperature increases going towards small radii.

2.7 Compton Scattering

A cloud of photons passing thorough a region containing free electrons will find its spectrum modified as a result of Thomson/Compton scattering given sufficient optical depth. If the electrons overall are more energetic than the photons, the photons will, on average, be scattered to higher energies. If, on the other hand, the electrons are less energetic, the photons will be scattered to lower energies.

2.7.1 Direct Compton Scattering

If a photon with initial energy $E = h\nu_0$ interacts with a stationary electron, it loses a certain fraction of its momentum and energy which is transferred to the electron. Calling θ the angle between the new and old direction of the photon, ϕ the angle of the scattered electron, and assuming the conservation of energy and momentum, we can write:

$$h\nu_0 + m_e c^2 = h\nu + \gamma m_e c^2 \tag{2.7}$$

$$\frac{h\nu_0}{c} = \frac{h\nu}{c}\cos\theta + \gamma m_e v \cos\phi \tag{2.8}$$

$$0 = \frac{h\nu}{c}\sin\theta + \gamma m_e v \sin\phi \tag{2.9}$$

After the scattering, the energy of the photon will be:

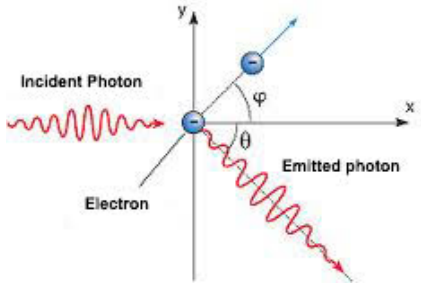

Figure 2.5: Schematic view of the collision between a high-energy photon and a free stationary electron in direct Compton scattering.

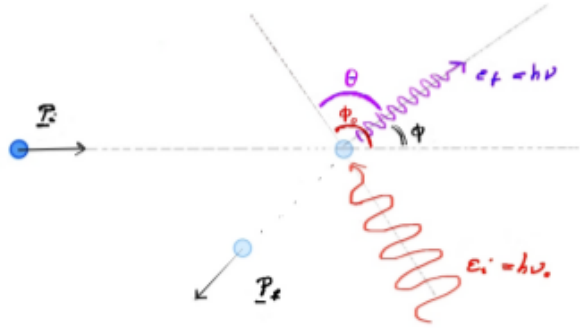

Figure 2.6: Schematic view of the collision between a photon and a high-energy electron in inverse Compton scattering.

$$h\nu = \frac{h\nu_0}{1 + \frac{h\nu_0}{m_e c^2}(1 - \cos\theta)} \tag{2.10}$$

In the case $h\nu_0 << m_e c^2$, the energy of the photon will remain the same, and this is called Thomson scattering. When $h\nu_0 \geq m_e c^2$, the photon will lose energy which will be gained by the electron, and this is called Compton scattering.

2.7.2 Inverse Compton Scattering

Generally Inverse Compton scattering of low energy photons in a hot electrons plasma is associated with the disk corona interaction. A sketch of a possible disk-corona geometry is reported in Fig. 2.7.

In order to estimate the amount of energy lost by the electron, we firstly assume that the reference frame is locked to the electron (where the electron experiences a direct Compton interaction) an then we come back to the laboratory frame system taking into account the relative movement of the two frame systems (Doppler Shift). In the frame system locked to the electron we can write:

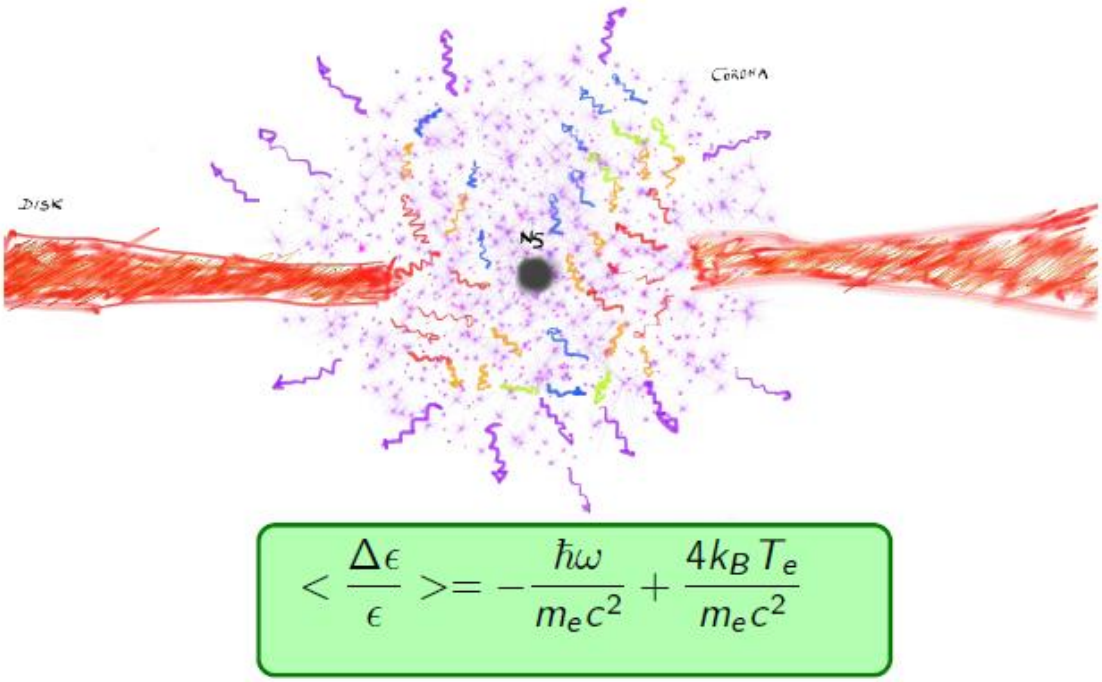

$$< \frac{\Delta\epsilon}{\epsilon} >= -\frac{\hbar\omega}{m_e c^2} + \frac{4k_B T_e}{m_e c^2}$$

Figure 2.7: Schematic view of a possible disk-corona geometry. Soft photons from the disk may interact with hot electrons in the corona, which is the place where the inverse Compton scattering occurs.

$$h\nu' = \frac{h\nu'_0}{1 + \frac{h\nu'_0}{m_e c^2}(1 - \cos\theta')} \tag{2.11}$$

In the case of *Thomson Regime*, that is when $\frac{h\nu'_0}{m_e c^2} \ll 1$, we can do some approximations:

$$h\nu' \approx h\nu'_0 \tag{2.12}$$

$$h\nu'_0 = \gamma h\nu_0(1 - \beta\cos\phi_0) \tag{2.13}$$

$$h\nu = \gamma h\nu'(1 + \beta\cos\phi') \tag{2.14}$$

Thus the new value of the photon energy after the scatter is:

$$h\nu = \gamma^2 h\nu_0(1 - \beta\cos\phi_0)(1 + \beta\cos\phi') \tag{2.15}$$

Therefore, in the inverse Compton scattering, the photon can gain a large amount of energy depending on the scattering angles. The most efficient case is that of a head collision ($\phi_0 = \pi$) with a back scattering of the photon ($\phi = 0$). In this case, the photon attains the highest energy after the scattering, $h\nu \simeq 4\gamma^2 h\nu_0$.

2.7.3 Comptonization

The modification of the photon spectrum by direct and inverse Compton scattering is called Comptonization. For Compton diffusion, in direct Compton scattering the average amount of energy lost by the photon and averaged over the scattering angle ϕ, is

$$< \frac{\Delta\epsilon}{\epsilon} >_\phi = -\frac{\hbar\omega}{m_e c^2} \tag{2.16}$$

Instead in the case of Inverse Compton scattering the averaged gained energy is

$$\frac{dE_{ph}}{dt} = \frac{4}{3}\sigma_T c U_{rad}\beta^2\gamma^2 \tag{2.17}$$

where U_{rad} is the radiation energy density of the photon field.

Now assuming that $\gamma \sim 1$ and a thermal distribution of the electron velocities, the average relative gain in energy for inverse Compton scattering is

$$< \frac{\Delta\epsilon}{\epsilon} >_\phi = \frac{4k_B T_e}{m_e c^2} \tag{2.18}$$

We can therefore summarize the energy exchange between the photon and the electron as follows:

$\hbar\omega < 4k_BT_e \rightarrow$ Energy transferred to the photon

$\hbar\omega = 4k_BT_e \rightarrow$ Compoton Saturation

$\hbar\omega > 4k_BT_e \rightarrow$ Energy transferred to the electron

When electrons are more energetic than photons (inverse Compton dominating), the variation of the energy of the photons due to N collisions can be written as

$$\frac{\epsilon}{\epsilon_0} = (1 + \frac{4k_BT_e}{m_ec^2})^N \tag{2.19}$$

In the approximation $k_BT_e \ll m_ec^2$ we have:

$$\frac{\epsilon}{\epsilon_0} = exp(4Y_C) \tag{2.20}$$

where $Y_c = \frac{k_BT_e}{m_ec^2} max(\tau; \tau^2)$ is the Compton y parameter. Therefore the incident photon spectrum will be significantly changed by Comptonization when $Y_c \geq 1/4$.

2.8 Reflection Spectrum

The reflection spectrum is formed when hard photons (generated in the disk-corona interaction via inverse Compton) intercept the disk and interact with cold material forming the optically thick accretion disk. For photon energies below about 10 keV the optical depth of photo-absorption dominates over the optical depth for Compton scattering. Therefore these photons are absorbed by the cold matter rather than reflected. On the other hand, photons with energy $\geq$ 15 keV will be predominantly Compton scattered, losing part of their energy. The resulting spectrum is a broad bump between about 10 keV and about 50 keV, as illustrated in Figure 2.8.

An important consequence of the photo-absorption at low energies is the presence of absorption edges and the emission of fluorescence lines from the most abundant elements present in the accreting material. Because of its relatively high abundance and fluorescence yield, these features are particularly strong for the K-shell of iron (Fe): in particular the predicted equivalent width of the Fe Kα line can be as strong as 150 eV. The reflection component gives important information about the matter in the reflector and the geometry of the system. A low energies the reflected spectrum depends on photo-electric absorption, and therefore is a function of the ionization state and elemental abundances of the

matter in the reflector (e.g. George and Fabian 1991; Matt, Perola, and Piro 1991). The overall strength of the reflection component depends on the solid angle subtended by the reflector as seen by the corona and the inclination angle of the disk with respect to the line of sight, and hence gives information on the geometry of the system.

The high orbital velocities of the matter in the disk, especially when the disk extends to radii close to the compact object, give a strong Doppler blueshift and intensity boost to the reflected line produced by material moving towards the observer, while the line produced by material moving away from us is redshifted and suppressed. Gravitational redshift is also important. The expected reflected line profiles are therefore broad and shifted to lower energies (e.g. Fabian et al. (2000)). The line profile is shaped by the effects of Doppler shifts and gravitational redshift. The resulting line profile is shown in Figure 2.9. The Fe line profile is therefore an important diagnostic tool since it gives information on the velocity field in the disk and on how close it extends towards the compact object. The fitting of these relativistically smeared profile can give information on the inner and outer radii of the emitting region in the disk, the inclination angle of the disk with respect to the line of sight and the emissivity law in the disk as a function of its radius.

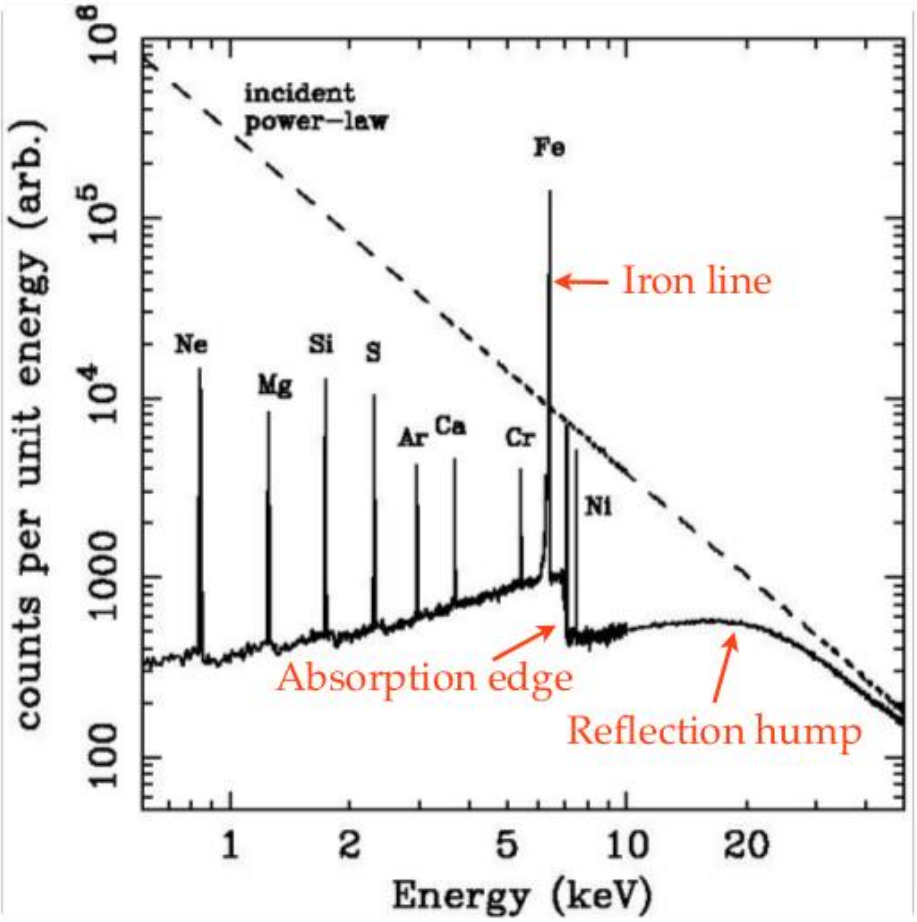

Figure 2.8: Montecarlo simulation showing the reflection spectrum obtained assuming as incident spectrum a power-law (dashed-line)

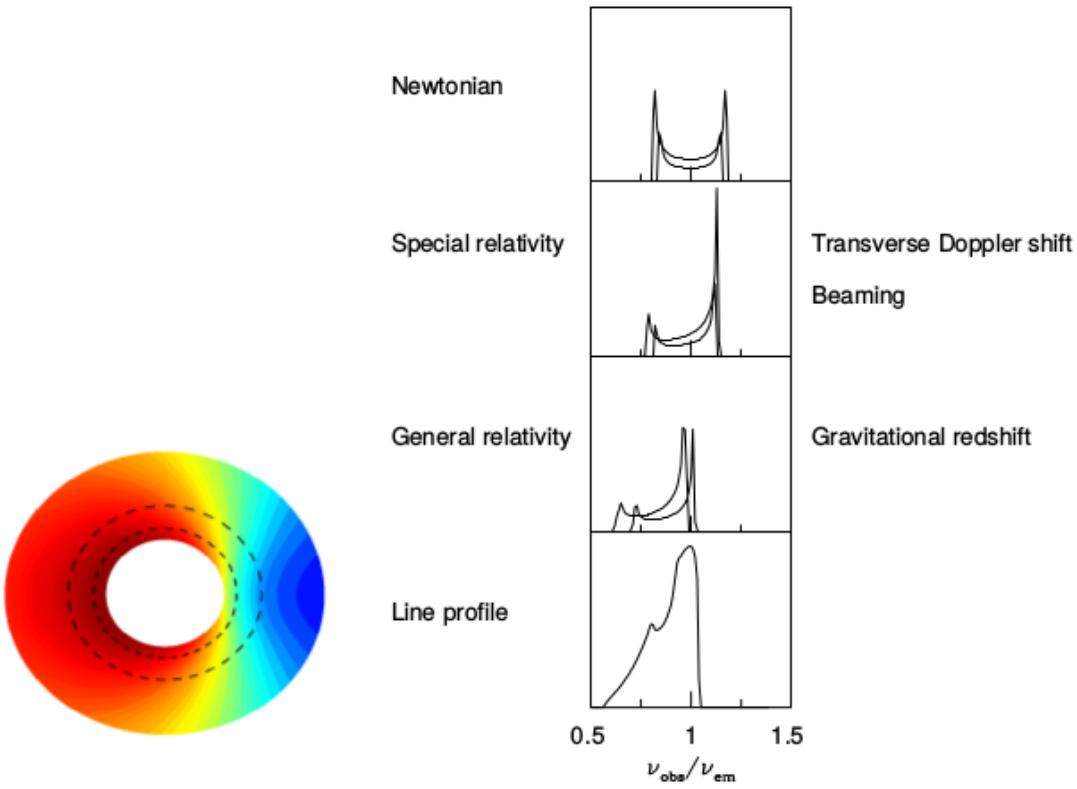

Figure 2.9: The line profile is shaped by the effects of Doppler shifts and gravitational redshifting. In a non relativistic disk, each radius of the disk produces a symmetric double-horned line profile corresponding to emission from material on both the approaching (blueshifted) and receding (redshifted) sides. The inner regions of the disk, where the material is moving the fastest, produce the broadest parts of the line (Fabian et al., 2000)

Chapter 3

Suzaku broad band spectrum of 4U 1705–44: Probing the Reflection component in the hard state

3.1 Abstract

Iron emission lines at $6.4 - 6.97$ keV, identified with Kα radiative transitions, are among the strongest discrete features in the X-ray band. These are one of the most powerful probes to infer the properties of the plasma in the innermost part of the accretion disk around a compact object. In this chapter we present a recent *Suzaku* observation, 100–ks effective exposure, of the atoll source and X-ray burster 4U 1705–44, where we clearly detect signatures of a reflection component which is distorted by the high–velocity motion in the accretion disk. The reflection component consists of a broad iron line at about 6.4 keV and a Compton bump at high X-ray energies, around 20 keV. All these features are consistently fitted with a reflection model, and we find that in the hard state the smearing parameters are remarkably similar to those found in a previous *XMM-Newton* observation performed in the soft state. In particular, we find that the inner disk radius is $R_{in} = 17 \pm 5\ R_g$ (where R_g is the Gravitational radius, GM/c^2), the emissivity dependence from the disk radius is $r^{-2.5\pm0.5}$, the inclination angle with respect to the line of sight is $i = 43^\circ \pm 5^\circ$, and the outer radius of the emitting region in the disk is $R_{out} > 200\ R_g$. We note that the accretion disk does not appear to be truncated at large radii, although the source is in a hard state at $\sim 3\%$ of the Eddington luminosity for a neutron star. We also find evidence of a

broad emission line at low energies, at 3.03 ± 0.03 keV, compatible with emission from mildly ionized Argon (Ar XVI-XVII). Argon transitions are not included in the self–consistent reflection models that we used and we therefore added an extra component to our model to fit this feature. The low energy line appears compatible with being smeared by the same inner disk parameters found for the reflection component.

3.2 Introduction

Neutron Star Low Mass X-ray Binaries (hereafter NS LMXBs) are binary systems in which a weakly magnetic NS accretes matter from a low mass ($< 1 M_{\odot}$) companion star via Roche-Lobe overflow. In these systems the accretion disk can approach the compact object, as testified by the very fast time variability observed up to kHz frequencies (see van der Klis, 2006, as a review). Broad emission lines (FWHM up to $\sim$ 1 keV) at energies in the range 6.4 – 6.97 keV are often observed in the spectra of NS LMXBs (see e.g. Di Salvo et al. (2005b); Piraino et al. (2007); Bhattacharyya and Strohmayer (2007); Cackett et al. (2008); Pandel et al. (2008b); Di Salvo et al. (2009b); D'Aì et al. (2009b); Iaria et al. (2009); Papitto et al. (2009a); Cackett et al. (2009a); Shaposhnikov et al. (2009); Papitto et al. (2010a); Egron et al. (2011a); Piraino et al. (2012); Papitto et al. (2013a); Miller et al. (2013). These lines are identified with the Kα radiative transitions of iron at different ionization states. These features are powerful tools to investigate the structure of the accretion flow close to the central source; in particular, important information can be obtained from the detailed spectroscopy of the line profile, since it is determined by the ionization state, geometry and velocity field of the reprocessing plasma. In fact, the broad iron line observed in NS LMXBs is thought to originate from reflection of the primary X-ray continuum off the inner accretion disk and the width of the line is expected to be a signature of the Keplerian motion of matter in the inner accretion disk at (mildly) relativistic velocities. In this model, the combination of Doppler effects from the high orbital velocities and Special and General relativistic effects arising from the strong gravity in the vicinity of the NS smears and shifts the reflected features. As a consequence, the line will have a characteristically broad and asymmetric profile, the detailed shape of which depends on the inclination and on how deep the accretion disk extends into the NS gravitational potential (e. g. Fabian et al. (1989); Matt et al. (1992)).

If the origin of this line is from disk reprocessing, one would also expect the

presence of other discrete features (such as emission lines and absorption edges from the most abundant elements) and a bump between 20 and 40 keV due to direct Compton scattering of the primary spectrum by the electrons in the disk. Indeed this reflection bump has been observed in the spectra of some NS LMXBs (see e.g. Barret et al. (2000); Piraino et al. (1999); Yoshida et al. (1993); Fiocchi et al. (2007); Egron et al. (2013a); Miller et al. (2013)), usually with reflection amplitudes (defined in terms of the solid angle $\Omega/2\pi$ subtended by the reflector as seen from the corona) lower than 0.3. In some cases an anti-correlation has been claimed between the photon index of the primary spectrum and the reflection amplitude of the reprocessed component Zdziarski et al. (1999); Barret et al. (2000); Piraino et al. (1999), the same observed in Seyfert galaxies and galactic Black Hole (hereafter BH) candidates. This is probably caused by variations in the position of the inner rim of the disk.

The disk origin of the iron line in NS LMXBs is, however, debated in literature because of the brightness of these sources, which may cause photon pile-up and systematics in CCD spectra Ng et al. (2010), making the detection of any asymmetry in the line profile somewhat controversial. However, a large number of simulations using a statistical model of photon pile-up to assess its impacts on relativistic disk line and continuum spectra suggest that severe photon pile-up acts to falsely narrow emission lines, leading to falsely large disk radii Miller et al. (2010). These simulations also indicate that relativistic disk spectroscopy is generally robust against pile-up when this effect is modest. Moreover, several authors (e.g. Cackett et al. (2012); Egron et al. (2013a)) have shown that the CCD-based spectra from *Suzaku* and *XMM-Newton* are compatible with gas-based spectra from EXOSAT, BeppoSAX, and RXTE, demonstrating that the broad profiles seen are intrinsic to the line and not due to instrumental issues. They also report that a few BeppoSAX observations show evidence for asymmetric lines, with a relativistic diskline model providing a significantly better fit than a Gaussian line (see also Piraino et al. (1999)).

Nevertheless alternatives have been proposed to explain the profiles of these features. In particular, Ng et al. (2010) propose that Compton broadening may be sufficient to explain the large width of the line. However, when self-consistently included in the fit, Compton broadening alone appears to be insufficient to explain the observed line profile (see e.g. Reis et al. (2009); Egron et al. (2013a); Sanna et al. (2013)). Also, Cackett and Miller (2013) have explored the observational signatures expected from broadening in a wind. In this case the iron line width should increase with increasing the column density of the absorber (due to an

increase in the number of scatterings). They show that there is no significant correlation between line width and column density, favoring an inner disk origin for the line broadening rather than scattering in a wind.

4U 1705–44 is a well-studied atoll source Hasinger and van der Klis (1989b); Olive et al. (2003), which also shows type-I X-ray bursts. Similarly to X-ray binaries containing BHs, this source regularly shows state transitions: from a high/soft state, where the X-ray spectrum is dominated by soft spectral components with typical temperatures less than a few keV, to low/hard states where the X-ray spectrum is dominated by a hard thermal Comptonisation (e.g. Barret and Olive (2002); Piraino et al. (2007)). The presence of broad discrete features in this source has been often reported in literature. A broad iron line was observed, in the soft and/or hard state, with moderate/high spectral resolution by the Chandra/HETG Di Salvo et al. (2005b), BeppoSAX Piraino et al. (2007), Suzaku Reis et al. (2009), and XMM/pn Di Salvo et al. (2009b); D'Aì et al. (2010b); Egron et al. (2013a). The XMM observation, taken in August 2008 during a soft state (45 ks effective exposure time), showed one of the highest signal-to-noise ratio iron line profile ever observed in a NS LMXB. The line profile is clearly broad and could be fitted equally well with a relativistic line profile, such as *diskline* Fabian et al. (1989) or *relline* Dauser et al. (2010), or with self-consistent reflection models, such as *reflionx* Ross and Fabian (2005a), *refbb* Ballantyne (2004), and *xillver* García and Kallman (2010). All these models gave parameters of the inner disk with unprecedented precision and all compatible with each other within the small statistical uncertainties (see Di Salvo et al. (2009b); D'Aì et al. (2010b); Egron et al. (2013a)). The line is identified with the Kα transition of highly ionised iron, Fe XXV; the inner disk radius is $R_{in} = 14 \pm 2$ R$_g$ (where R$_g$ is the Gravitational radius, GM/c^2), the emissivity index of the disk is -2.27 ± 0.08 (compatible with a disk illuminated by a central source), the inclination angle with respect to the line of sight is $i = 39 \pm 1$ degrees. This, together with the presence of other low-energy features from S XVI, Ar XVIII, Ca XIX and a smeared iron edge at 8.4 keV, which all are compatible with being smeared with the same inner disk parameters, makes 4U 1705–44 the best source for a detailed spectroscopic study, in order to address the disk origin of the observed iron line and of the whole reflection component.

In this thesis we present a high statistics, 100-ks effective exposure, *Suzaku* observation of 4U 1705–44 during a hard state: these data allow us a detailed study of the reflection features and the fit, with a self-consistent reflection model, of both the iron line profile and the associated Compton reflection bump at en-

ergies above 10 keV. In this spectrum, which includes hard-band data (up to 200 keV), the overall fractional amount of reflection is well determined by fitting the Compton bump. We can therefore test whether the observed iron line is consistent with this fractional amount of reflection. In this way we confirm independently (fitting a different spectral state and using different instruments) the inner disk parameters already obtained with *XMM-Newton* in the soft state.

3.3 Observations

Suzaku (Mitsuda et al., 2007) observed 4U 1705–44 on 2012 March 27 as the result of a Target of Opportunity (ToO) program during a hard state for a total observing time of 250 ks, corresponding to an effective exposure time of about 100 ks because of observational gaps caused by Earth occultations along the low equatorial orbit of the *Suzaku* satellite. Both the X-ray Imaging Spectrometers (XIS, 0.2-12 keV; Koyama et al. (2007)) and the Hard X-ray Detector (HXD, 10-600 keV; Takahashi et al. (2007)) instruments were used during these observations. There are four XIS detectors, numbered as 0 to 3. XIS0, XIS2 and XIS3 all use front-illuminated CCDs and have very similar responses, while XIS1 uses a back-illuminated CCD. At the time of this observation the available CCDs were three due to the loss of the XIS2. The HXD instrument consists of two types of collimated (non-imaging) detectors, the PIN diodes (10-70 keV) and the GSO scintillators (30-600 keV).

We reprocessed the data using the *aepipeline* tool provided by *Suzaku FTOOLS version 20* updated with the latest calibration files (2013 November). As second step, in order to obtain a more accurate estimate of the *Suzaku* attitude, we have calculated a new attitude using the free tool *aeattcor.sl* created by J. E. Davis. Then we have applied the new attitude to XIS event files using the FTOOLS *xiscoord*. During the observation, XIS0, XIS1, and XIS3 were operated using the 1/4 window option. The effective exposure time of each XIS CCD is 96.67 ks. In order to estimate the pile-up in the XIS spectra we have used the public available tool *pile-estimate.sl* created by M. A. Novak. Using a circular region with radius equal to 105", we have found that in each XIS CCD, the pile-up fraction is $\sim 3\%$ at most. The pile-up fraction is sufficiently small that we can neglect its effects on our spectral fitting results. In fact, we have checked that spectral results do not change significantly if we exclude a central circle in the extraction region in order to further reduce the pile-up fraction. Therefore, we have extracted the source and background spectra from a circular extraction region of radius 105"

each, the background circle being centered close to the edge of the CCD, where no significant contaminating photons from the source were present. The response files of each XIS spectrum have been generated using the *xisrmfgen* and *xisarfgen* tools. Since the response of XIS0 and XIS3 are very similar, we have combined their spectra and responses using the tool *addascaspec*.

The PIN spectrum has been extracted using the tool *hxdpinxbpi*. Both the non X-ray and cosmic X-ray backgrounds are taken into account. The non X-ray background (NXB) is calculated from the background event files distributed by the HXD team. The cosmic X-ray background (CXB) is from the model by Boldt and Leiter (1987). The response files provided by the HXD team are used. We selected the HXD/PIN events in the energy range 12-30 keV and produced the HXD/PIN background-subtracted light curve using the SUZAKU tool `hxd-pinxblc` and adopting the background event files distributed by the HXD team. Since this light curve follows the XIS0 light curve, we conclude that no contaminating flare was present in the data. We have also extracted the GSO spectrum running the tool *hxdgsoxbpi*. For the background we have used the 'tuned' non X-ray background, whereas for the response file we have used the latest version provided on 2011-06-01.

We have extracted the XIS0 light curves in the energy range $0.9-2.8$, $2.8-10$ and $0.9-10$ keV, respectively (see Fig. 1). Nine type-I X-ray bursts are observed in the total 250-ks light curve. The source (persistent) count rate gradually increases by about 40% during the observation. Since no changes are observed in the hardness ratio (given by the ratio of the source counts in the $2.8-10$ keV range to the source counts in the $0.9-2.8$ keV, (see Fig. 3.1) we conclude that the X-ray spectral shape of the source does not change significantly during the observation.

3.4 Spectral Analysis and Results

In order to extract spectra for the persistent emission, we have excluded the type-I bursts that occurred during the observation. In particular we have excluded approximately 100 s of data starting from the onset of each burst. We adopt $0.7-11$ keV energy range for the XIS0+XIS3 (hereafter XIS03) and XIS1 spectra, $15-50$ keV energy range for the HXD/PIN spectrum and $50-200$ keV energy range for the HXD/GSO spectrum. We excluded the energy interval between 1.7 and 2.0 keV from the XIS03 and XIS1 spectra because of the presence of systematic features associated with neutral silicon and neutral gold which give a

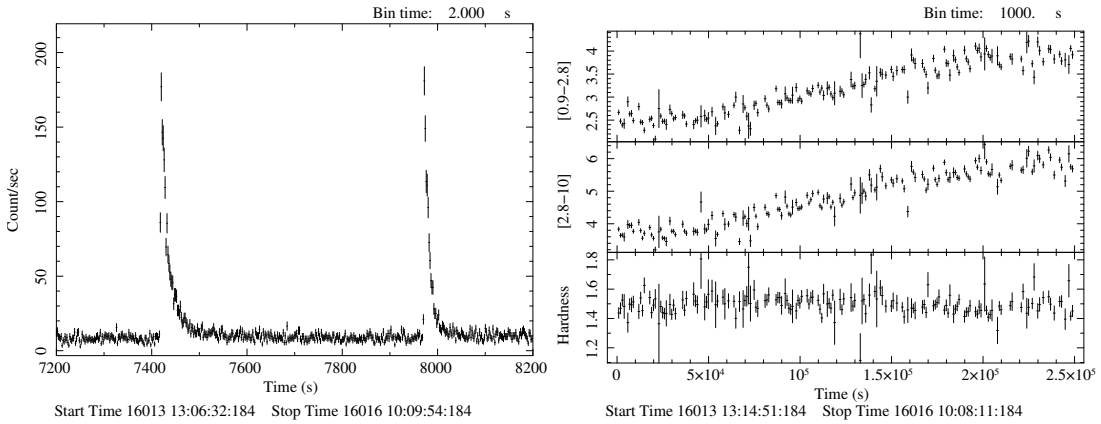

Figure 3.1: Left: *Suzaku* XIS0 light curve in the energy range 0.9 - 10 keV showing two of the nine type-I bursts which occurred during the 250-ks observation. **Right:** *Suzaku* XIS0 light curves in the energy range $0.9 - 2.8$ keV (top panel), $2.8 - 10$ keV (middle panel), and the corresponding hardness ratio (bottom panel).

mismatch between the two spectra. The XIS spectra were grouped by a factor 4 in order not to oversample too much the instrumental energy resolution. The HXD/PIN and HXD/GSO spectra were grouped in order to have at least 25 photons per energy channel. We fitted the spectra using XSPEC version 12.7.0.

We started to fit the continuum in the 0.7–200 keV energy range with the typical model used for NS LMXBs of the atoll class, which revealed to be the best fit continuum for this source too (see e.g. Di Salvo et al., 2009b; Piraino et al., 2007; Barret and Olive, 2002). This model consists of a soft blackbody and a thermal Comptonised component, in this case modelled by `nthComp` (Życki et al., 1999a), modified at low energy by photoelectric absorption caused by neutral matter and modeled by `phabs` in XSPEC. This continuum model gave, however, an unacceptable fit, corresponding to a $\chi^2/dof = 2425.13/1511$, because of the presence of evident localised residuals at 2.5–3.5 keV, 6–9 keV and 15–30 keV. The most prominent is a clear iron line profile at energies from 5 to 7 keV and an absorption feature at 7–8 keV (see Fig. 3.2).

In order to fit these residuals, we first added to our continuum model the `pexriv` component (Magdziarz and Zdziarski, 1995) which takes into account the iron edge and Compton bump present in the residuals. Note that pexriv does not self-consistently include any emission line. The photon index and the high energy cutoff of the pexriv component were linked to those of the nthComp component. Here and in the following we neglect any reflection of the soft (blackbody) component, which in any case contributes to a small fraction of the total flux and

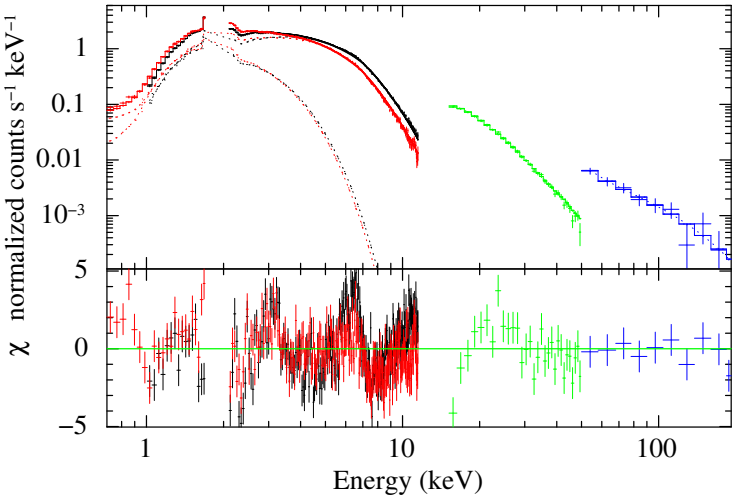

Figure 3.2: *Suzaku* data in the energy range 0.7 - 200 keV (top) and residuals in units of σ with respect to the simpler phenomenological model (bottom) of 4U 1705–44. The model consists of a blackbody (dotted lines) and the Comptonization component *nthComp*, both multiplied by photoelectric absorption.

most of its flux is at soft energies (below $4-5$ keV). The addition of this component gave a significant improvement of the fit reducing the χ^2/dof to the value 2009.67/1509 ($\Delta\chi^2 = 415$ for the addition of two parameters). Therefore, the presence of the Compton hump and the iron edge are detected with high statistical significance (an F-test would give a probability of chance improvement of the fit negligibly small, $\sim 2.7 \times 10^{-62}$). We then added a Gaussian line at 6.4 keV obtaining again an improvement of the fit. As a first step we decided to fix the energy of the line at 6.4 keV because, otherwise, it tends to get broad (Gaussian sigma about 1 keV) and its energy tends to decrease to 6.2 keV. This fit gives a $\chi^2/dof = 1956.50/1507$ ($\Delta\chi^2 = 53$ for the addition of two parameters). This line can be identified with fluorescence from neutral iron. The addition of another Gaussian at about 3 keV again improves the fit, giving $\chi^2/dof = 1829.89/1504$ ($\Delta\chi^2 = 127$ for the addition of three parameters). This line can be identified with emission from mildly ionized Argon, Ar XVI–XVII. In order to check whether the iron line energy was stable or not, we let the iron line energy free to vary obtaining $\chi^2/dof = 1818/1503$. We also tried to substitute the Gaussian line at ~ 6 keV with a diskline. In this case we had to fix all the smearing parameters but the inner radius of the disk. This did result in a slight improvement of the fit, since we get $\chi^2/dof = 1803/1503$ fixing the emissivity index at -2.4, the outer radius at 400 R_g, the inclination angle at 40 deg. Also in this case the centroid energy of the line remained at $6.1-6.3$ keV, but we get an upper limit to the inner radius

Table 3.1: The best fit parameters of the spectral fitting of the *Suzaku* spectrum of 4U 1705–44 in the $0.7 - 200$ keV energy range with phenomenological models. The blackbody luminosity is given in units of L_{35}/D_{10}^2, where L_{35} is the bolometric luminosity in units of 10^{35} ergs/s and D_{10} the distance to the source in units of 10 kpc. The blackbody radius is calculated in the hypothesis of spherical emission and for a distance of 7.4 kpc. Fluxes in the nthComp and pexriv components are calculated in the $1-16$ keV range, while total flux is calculated in the $1-10$ keV band. Uncertainties are given at 90% confidence level.

Component	Parameter	Basic Model	Pexriv	Pexiriv + 2Gauss	Smeared (Pex + 2Gaus)
phabs	N_H ($\times 10^{22}$ cm^{-2})	1.899 ± 0.025	2.13 ± 0.05	2.02 ± 0.05	2.04 ± 0.06
bbody	kT_{BB} (keV)	0.503 ± 0.015	$0.265^{+0.004}_{-0.026}$	0.39 ± 0.04	0.35 ± 0.04
bbody	L_{BB} (L_{35}/D_{10}^2) / Norm	8.8 ± 0.6	3.6 ± 0.8	5.3 ± 1.3	4.0 ± 0.6
bbody	R_{BB} (km)	7.6 ± 0.5	17.6 ± 4.4	9.8 ± 2.3	10.6 ± 2.5
nthComp	kT_{seed} (keV)	0.90 ± 0.04	0.569 ± 0.014	0.69 ± 0.06	0.64 ± 0.04
nthComp	Γ	2.05 ± 0.03	2.081 ± 0.018	2.05 ± 0.04	2.08 ± 0.03
nthComp	kT_e (keV)	101^{+100}_{-74}	$63.2^{+12}_{-2.4}$	$80.7^{+59}_{-9.9}$	89^{+28}_{-20}
nthComp	Flux (10^{-10} ergs cm^{-2} s^{-1})	4.73	4.67	4.66	4.61
pexriv	ξ (erg cm s^{-1})	–	< 1	< 1	< 1
pexriv	Incl (deg)	–	40 (fixed)	40 (fixed)	40 (fixed)
pexriv	Flux (10^{-10} ergs cm^{-2} s^{-1})		0.9	0.56	0.73
gauss	E_{line} (keV)	–	–	3.00 ± 0.04	3.02 ± 0.04
gauss	σ_{line} (keV)	–	–	0.28 ± 0.03	–
gauss	I_{line} ($\times 10^{-4}$ ph cm^{-2} s^{-1})	–	–	3.3 ± 0.9	2.4 ± 0.5
gauss	EqW (eV)	–	–	24.0 ± 7.6	18.3 ± 3.5
gauss	E_{Fe} (keV)	–	–	6.21 ± 0.08	6.27 ± 0.06
gauss	σ_{Fe} (keV)	–	–	0.46 ± 0.07	–
gauss	I_{line} ($\times 10^{-4}$ ph cm^{-2} s^{-1})	–	–	$1.58^{+1.2}_{-0.19}$	$1.9^{+0.7}_{-0.4}$
gauss	EqW (eV)	–	–	33 ± 17	52 ± 21
rdblur	*Betor*	–	–	–	-2.2 ± 0.5
rdblur	R_{in} (GM/c^2)	–	–	–	< 29
rdblur	R_{out} (GM/c^2)	–	–	–	360^{+360}_{-160}
rdblur	Incl (deg)	–	–	–	54^{+17}_{-9}
total	Flux (10^{-10} ergs cm^{-2} s^{-1})	3.3 ± 0.7	3.34 ± 0.02	3.34 ± 0.03	3.34 ± 0.03
total	χ^2 (dof)	2425 (1511)	1990 (1509)	1818 (1503)	1783 (1501)

of the disk of 25 R_g. On the other hand, we get a more significant improvement of the fit if we add a (mild) relativistic smearing to the whole reflection component (i.e. the emission lines at ~ 3 and ~ 6 keV and the pexriv component) convolving all these three components with `rdblur`, the kernel of `diskline`. In this case we get $\chi^2/dof = 1783/1501$ ($\Delta\chi^2 = 35$ for the addition of three parameters, corresponding to an F-test probability of chance improvement of $\sim 4 \times 10^{-7}$). The results of these phenomenological models are reported in Table 3.1.

In order to fit the high-quality *Suzaku* spectrum with more consistent physical models, we substitute the pexriv + Fe line components with the self-consistent

reflection model `reflionx` (Ross and Fabian, 2005a), modified by a relativistic blurring component (again modeled with rdblur) to consider the relativistic and/or Doppler effects produced by the motion in the inner disk close to the compact object. In this model, emission lines from the most abundant elements or ions are also self-consistently calculated. In the reflionx model the emergent (reflected) spectrum is calculated for an optically-thick atmosphere (such as the surface of an accretion disk) of constant density illuminated by radiation with a power-law spectrum, whose photon index is fixed to that of the nthComp component, and a high-energy exponential cutoff with e-folding energy fixed at 300 keV. In order to take into account the high-energy cutoff in the illuminating spectrum, we have multiplied the reflionx spectrum by a high energy cutoff with the e-folding energy fixed to the value of the e-folding energy of the primary (nthComp) component. Since the reflionx model does not take into account transitions from Ar and Ca, we fitted the emission line at ~ 3 keV with a diskline, fixing all the smearing parameters to those used for the reflionx component. The continuum emission is fitted with the same model as before, and we used for the soft component alternatively the bbody or the diskbb model. The results of these fits are shown in Table 3.2. We also checked the possibility of iron overabundance with respect to cosmic abundances (as claimed by Egron et al., 2013a, for the soft state), fixing the iron abundance alternatively to the cosmic value and twice the cosmic value. We find a slightly better fit when we fix the iron abundance to the cosmic value and we use a blackbody to fit the soft thermal component (see Table 3.2). The total $0.5 - 200$ keV luminosity of the source during the *Suzaku* observation was 6.15×10^{36} ergs/s assuming a distance to the source of 7.4 kpc.

Finally, we fitted the reflection component in the *Suzaku* spectrum of 4U 1705–44 with the convolution model `rfxconv` (Kolehmainen et al., 2011a), which has the advantage to take into account the exact shape of the illuminating continuum. For sake of completeness we also tried the self-consistent reflection model `relxill` by García et al. (2014), whose novelty is that for each point on the disk the proper reflection spectrum is chosen for each relativistically calculated emission angle. In the relxill model we fixed the photon index and e-folding energy of the reflected spectrum to those of the nthComp component. Both these models include emission lines from the most abundant elements or ions, as in the case of `reflionx`. Again we obtain a good fit of the 4U 1705–44 spectrum, with best-fit values of the reflection and smearing parameters well in agreement with those obtained with other reflection models (see Tab. 3.3, cf. with Tab. 3.1 and 3.2).

Table 3.2: The best fit parameters of the spectral fitting of the *Suzaku* spectrum of 4U 1705–44 in the $0.7 - 200$ keV energy range with the self-consistent reflection model `reflionx`. The blackbody luminosity is given in units of L_{35}/D_{10}^2, where L_{35} is the bolometric luminosity in units of 10^{35} ergs/s and D_{10} the distance to the source in units of 10 kpc. The blackbody radius is calculated in the hypothesis of spherical emission and for a distance of 7.4 kpc. The disk blackbody normalization is given by $(R_{in}(km)/D_{10})^2 \cos i$, where i is the inclination angle of the binary system. The disk blackbody inner radius R_{in} (km) is calculated for an inclination angle of 40°. Flux is calculated in the $1 - 10$ keV band. Uncertainties are given at 90% confidence level.

Parameter	BBODY [Fe = 1]	DISKBB [Fe = 1]	BBODY [Fe = 2]	DISKBB [Fe = 2]
N_H ($\times 10^{22}$ cm^{-2})	2.11 ± 0.04	2.27 ± 0.04	2.09 ± 0.04	2.25 ± 0.04
kT_{BB} (keV)	0.38 ± 0.03	0.53 ± 0.07	0.38 ± 0.03	0.52 ± 0.08
L_{BB} (L_{35}/D_{10}^2) / Norm	5.5 ± 0.7	58 ± 22	4.9 ± 0.5	61^{+42}_{-18}
R_{BB} (km) / R_{in} (km)	10.6 ± 1.8	6.4 ± 1.2	10.0 ± 1.7	$6.6^{+2.3}_{-1.0}$
kT_{seed} (keV)	0.68 ± 0.03	0.70 ± 0.06	0.66 ± 0.03	0.67 ± 0.06
Γ	2.01 ± 0.02	2.01 ± 0.02	1.95 ± 0.01	1.95 ± 0.01
kT_e (keV)	47^{+19}_{-11}	47^{+17}_{-10}	27 ± 5	27 ± 5
ξ (erg cm s^{-1})	< 13	< 19	< 24	22 ± 4
Betor	-2.5 ± 0.5	-2.5 ± 0.5	-2.4 ± 0.4	-2.5 ± 0.5
R_{in} (GM/c^2)	17^{+4}_{-6}	16^{+4}_{-7}	16^{+4}_{-5}	16^{+4}_{-7}
R_{out} (GM/c^2)	370^{+8000}_{-180}	370^{+370}_{-170}	330^{+8000}_{-200}	350^{+350}_{-170}
Incl (deg)	43 ± 5	42 ± 5	41 ± 4	42 ± 4
E_{line} (keV)	3.03 ± 0.03	3.03 ± 0.03	3.04 ± 0.03	3.04 ± 0.03
I_{line} ($\times 10^{-4}$ ph cm^{-2} s^{-1})	2.4 ± 0.4	2.3 ± 0.4	2.4 ± 0.4	2.3 ± 0.4
EqW (eV)	18.2 ± 3.6	17.0 ± 3.4	18.6 ± 3.5	17.5 ± 3.7
Flux (10^{-10} ergs cm^{-2} s^{-1})	3.34 ± 0.04	3.34 ± 0.15	3.34 ± 0.04	3.34 ± 0.14
total χ^2 (dof)	1831 (1503)	1841 (1503)	1846 (1503)	1852 (1503)

Table 3.3: The best fit parameters of the spectral fitting of the *Suzaku* spectrum of 4U 1705–44 in the $0.7-200$ keV energy range with the self-consistent reflection models `rfxconv` and `relxill`. The blackbody luminosity is given in units of L_{35}/D_{10}^2, where L_{35} is the bolometric luminosity in units of 10^{35} ergs/s and D_{10} the distance to the source in units of 10 kpc. The blackbody radius is calculated in the hypothesis of spherical emission and for a distance of 7.4 kpc. Flux is calculated in the $0.7-200$ keV band. Uncertainties are given at 90% confidence level.

Parameter	RFXCONV [Fe = 1]	RELXILL [Fe = 1]
N_H ($\times 10^{22}$ cm^{-2})	2.05 ± 0.04	2.06 ± 0.05
kT_{BB} (keV)	0.37 ± 0.03	0.36 ± 0.04
L_{BB} (L_{35}/D_{10}^2) / Norm	4.6 ± 0.6	4.1 ± 0.7
R_{BB} (km) / R_{in} (km)	10.2 ± 1.8	10.3 ± 2.5
kT_{seed} (keV)	0.67 ± 0.03	0.63 ± 0.04
Γ	2.01 ± 0.01	1.979 ± 0.009
kT_e (keV)	34^{+5}_{-4}	43 ± 9
ξ (erg cm s^{-1})	60^{+20}_{-30}	12^{+9}_{-4}
Refl Amplitude	0.34 ± 0.04	0.34 (fixed)
Refl Norm	–	0.161 ± 0.017
Betor	-2.5 ± 0.5	$-3.2^{+0.4}_{-0.2}$
R_{in} (GM/c^2)	17^{+4}_{-7}	14 ± 2
R_{out} (GM/c^2)	> 202	260 (fixed)
Incl (deg)	43 ± 5	$31.6^{+1.9}_{-1.5}$
E_{line} (keV)	3.04 ± 0.04	3.10 ± 0.03
I_{line} ($\times 10^{-4}$ ph cm^{-2} s^{-1})	2.5 ± 0.4	2.2 ± 0.4
EqW (eV)	19.3 ± 0.3	17^{+3}_{-2}
Flux (10^{-10} ergs cm^{-2} s^{-1})	9.0 ± 0.3	$9.33^{+0.17}_{-0.36}$
total χ^2 (dof)	1832 (1503)	1818 (1504)

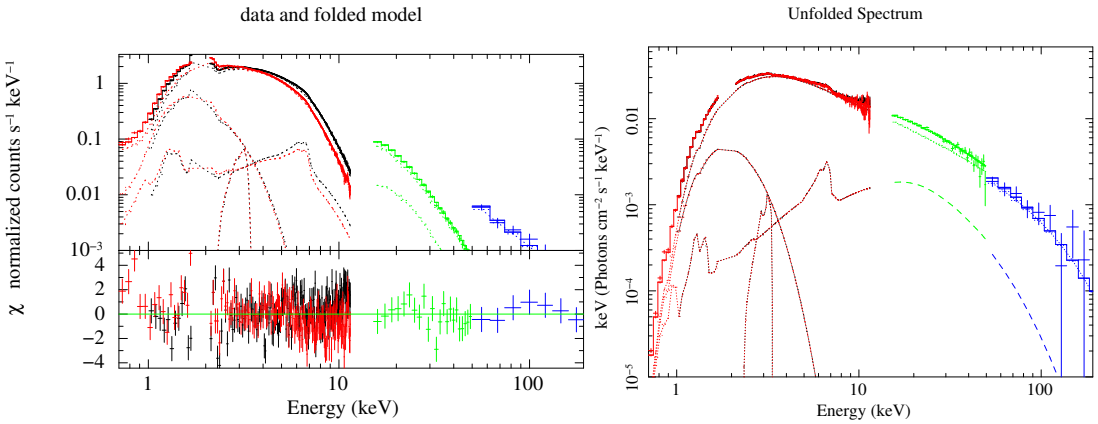

Figure 3.3: Left: *Suzaku* data in the energy range 0.7 - 200 keV (top) and residuals in units of σ with respect to the best-fit model (bottom) of 4U 1705–44 (see Table 3.2, first column). **Right:** *Suzaku* unfolded spectrum in the energy range 0.7 - 200 keV with respect to the best-fit model shown in the first column of Table 3.2. The model components are also shown. From the left to the right we see the blackbody component, the emission line at ~ 3 keV (smeared with the same smearing parameters used for the reflection component), the smeared reflection component modeled by *reflionx*. The main Comptonization component and the total model are plotted on top of the data.

3.5 Discussion

Similar to BH X-ray Binaries, NS LMXBs show clear differences in the spectral parameters during hard and soft states. Studying these differences is important in order to address different geometry or physical properties of the inner central emitting region in these two spectral states and in order to understand what causes the spectral transition. In fact, there is no general consensus on the hot corona–accretion disk geometry in these two spectral states. Theoretically the hard Comptonized component may come from either a patchy corona, possibly powered by magnetic flares (e.g. Beloborodov, 1999) or the base of a centrally located jet (e.g. Markoff et al., 2005). In both the cases, the thin accretion disk may extend close to the last marginally stable orbit or the NS surface. Alternatively the thin disk may be truncated at large distances from the compact object, with the central region replaced by an advection-dominated accretion flow (ADAF) where, at high accretion rates, material may condense to form an inner optically thick disk (see e.g. Esin et al., 1997). This hot, inner flow can also act as the launching site of the jet. In this respect, much information may come from the study of the so-called reflection component in different spectral states of a source (see Done et al., 2007, as a review).

In this chapter we have reported the results of the spectral analysis of a long *Suzaku* observation of the LMXB of the atoll class 4U 1705–44. This was the result of a ToO program intended to observe the source during a hard state. *Suzaku* observed the source for a total of 250 ks yielding a net exposure time of 100 ks. During the observation 9 type-I bursts were observed. We present here the spectral analysis of the persistent emission, while we will discuss the characteristics of the observed type-I bursts elsewhere. We have fitted the persistent emission spectrum in the broad band range between 0.7 and 200 keV using the continuum model which gave the best fit of previous high-quality spectra of this source obtained with RXTE, BeppoSAX, *XMM-Newton*, and Chandra (see e.g. Egron et al., 2013a, and references therein). The continuum model consists of a soft component modeled by `bbody` and a Comptonization component modeled by `nthComp`, both multiplied by the `phabs` component which takes into account photoelectric absorption by neutral matter in the interstellar medium. A smeared reflection component was necessary to obtain an acceptable fit of the broad–band *Suzaku* spectrum. This component was necessary to fit high-energy residuals above about 15 keV and a broad iron edge at about $8-9$ keV – the addition of the `pexriv` component to fit these two features gave a significant improvement of the quality of the fit with a probability of chance improvement, calculated with an F-test, which resulted to be negligibly small.

We detect other reflection features, such as a broad emission line at about 6.4 keV from neutral iron and a broad emission line at about 3 keV that we tentatively identify with the Kα transition from Ar XVI-XVII. These two features could be well fitted by broad `Gaussians`. Note that this Ar line is quite strong with respect to the observed iron line. If we consider the product of the element abundances ($\sim 4.7\times10^{-5}$ and $\sim 3.6\times10^{-6}$ for iron and argon, respectively) by the fluorescence yields (which can be calculated using the empirical formula yield $= Z^4/(30^4+Z^4)$, where Z is the atomic number), we obtain $\sim 1.7\times10^{-5}$ and $\sim 4\times10^{-7}$ for iron and argon, respectively. This means that the Ar line strength should be $\sim 2.4\%$ of Fe line strength. This in the hypothesis that all the atoms of these elements are in the ionization state producing the line. Note also that the observed line may depend on the illuminating continuum at that energy. In the case of 4U 1705–44 in the soft state, where Ar and Ca lines are clearly detected by *XMM-Newton* together with an Fe line, we find small differences in the line intensities (a factor 2 at most) and higher differences in the line equivalent width (up to a factor 8). However, when the spectrum is fitted to a self-consistent reflection model, a suitably modified version of the `xillver` model by García and Kallman (2010)

which includes Ar and Ca transitions, we find that the Ar line is well fitted by the reflection model with a slight overabundance by a factor 1.8 with respect to Solar abundances (see Egron et al., 2013a). We conclude therefore that the simple calculation above is merely an order of magnitude estimation and that the consistency of the Ar line with other reflection features should be checked using self-consistent reflection models including Ar and Ca transitions.

We also tried to fit all the reflection features (the Compton hump, the iron edge and the iron line) with a self-consistent reflection model such as `reflionx`, which we have modified with a high energy cutoff at the electron temperature of the Comptonizing corona to take into account the curvature of the Comptonization spectrum with respect to a simple power-law (used as illuminating spectrum in the reflionx model). The smearing of the reflection component has been taken into account multiplying it by the `rdblur` component. In this case we had to add a diskline to the model to fit the Ar line at 3 keV, since transitions from Ar are not taken into account in the reflionx model. Anyway, all the smearing parameters of the diskline used to fit the Ar line have been fixed to those used for the reflection component. In this case, we used a `bbody` or a `diskbb` to fit the soft thermal component and tried to vary the iron abundance fixing this value to 1 or 2 times the cosmic abundance. The best fit corresponds to a bbody component for the soft thermal emission and to an iron abundance of 1 (see Table 3.2). We also tried to fit the reflection component with the self-consistent convolution model `rfxconv`, which consistently takes into account the curvature of the illuminating spectrum caused by the high-energy rollover at the electron temperature in the corona producing the primary Comptonized spectrum, or with the `relxill` model, in which the cutoff energy in the reflected spectrum is fixed at the electron temperature of the primary Comptonized component, fitted with `nthComp`. Note that both rfxconv and relxill, as well as reflionx, all include Compton broadening effects caused by Compton scattering in the surface layers of the accretion disc. The results of these fits are reported in Table 3.3 and are perfectly consistent with those obtained with all the other reflection models that we tried.

In order to check the stability of the best fit model with respect to the smearing parameters of the reflection component, we have let all these parameters free to vary. The most uncertain of these parameters, as expected, is the outer radius of the disk, for which we find only loose constraints. Interestingly, all of the smearing parameters of the best fit model of this observation are in good agreement with the smearing parameters already obtained with other instruments, e.g. *XMM-*

Table 3.4: Comparison of the best-fit continuum and reflection parameters obtained for the soft state (SS) as observed in the 60-ks *XMM-Newton* observation and for the hard state (HS) observed by *Suzaku* (this thesis). Continuum parameters for the SS observed by *XMM-Newton* are taken by Egron et al. (2013a), who use a similar model
for the continuum, while smearing parameters of the reflection component are taken from Di Salvo et al. (2009b) where these parameters are obtained with smaller uncertainties. L_X is the X-ray luminosity extrapolated in the $0.1 - 150$ keV range for the SS, as reported by Egron et al. (2013a), and in the $0.5 - 200$ keV range for the HS (this work). L_{Edd} is the Eddington luminosity for a $1.4\ M_\odot$ NS, $L_{Edd} = 2.5 \times 10^{38}$ ergs s^{-1}
(van Paradijs and van der Klis, 1994).

Parameter	SS (*XMM-Newton*)	HS (*Suzaku*)
N_H ($\times 10^{22}$ cm^{-2})	2.08 ± 0.02	2.11 ± 0.04
bbody kT (keV)	0.56 ± 0.01	0.38 ± 0.03
bbody L_X (L_{37}/D_{10}^2)	2.58 ± 0.01	0.055 ± 0.007
R_{BB} (km)	33.3 ± 1.2	10.6 ± 1.8
nthComp kT_{seed} (keV)	1.30 ± 0.02	0.68 ± 0.03
nthComp kT_e (keV)	3.0 ± 0.1	47^{+20}_{-10}
ξ (erg cm s^{-1})	> 500	< 13
Betor	-2.27 ± 0.08	-2.5 ± 0.5
R_{in} (GM/c^2)	14 ± 2	17^{+4}_{-6}
R_{out} (GM/c^2)	3300^{+1500}_{-900}	370^{+8000}_{-180}
Incl (deg)	39 ± 1	43 ± 5
L_X/L_{Edd}	72%	2.9%

Newton and BeppoSAX (Di Salvo et al., 2009b; Egron et al., 2013a), during a soft state. In order to facilitate the comparison, we report in Table 3.4 the best fit parameters of the reflection (modeled by reflionx) and the relativistic smearing components obtained with *XMM-Newton* during a soft state (from Di Salvo et al., 2009b; Egron et al., 2013a) and obtained with *Suzaku* during a hard state (this work). Although the uncertainties in the spectral parameters in the hard state are larger than in the soft state (because of the lower source flux in the hard state), we find a very good agreement in all the parameters. In particular, the inclination angles of the system we obtain in the two cases are compatible well within the 90% c.l. uncertainty. The main difference in the reflection component between the hard and the soft state is in the ionization parameter ξ, which is much larger in the soft state than in the hard state, as expected because of the higher incident flux in the soft state. Also the continuum parameters are different; in particular, the temperatures of the soft components of the continuum (i.e. of the soft blackbody component and of the seed photons for the Comptonization) result higher in the soft state, while the electron temperature of the Comptonizing cloud results higher in the hard state, in agreement with what is expected.

We note that there is no clear indication of a receding inner accretion disk radius in the hard state, corresponding to a luminosity of $\sim 3\%$ of the Eddington luminosity, with respect to the soft state, which was observed at about 70% of L_{Edd}. On the contrary, the inner disk radius as inferred from the reflection component is consistent to be the same in the two spectral states, at about 34 km from the NS center. A similar indication comes from the inner radius of the disk as inferred from the blackbody component, that we interpret as the direct emission from the accretion disk. Both in the soft and in the hard state the blackbody radius is a few tens of km, in agreement with the estimate we get from the reflection component. We caution the reader, however, that neither the color factor or the geometry of the system has been taken into account in this calculation. What is reported is just a zero-order estimation of the radius of the region (assumed to be spherical) emitting the blackbody component. In particular, the spectral hardening factor may depend on luminosity (see e.g. Merloni et al., 2000) explaining why the inner disk radius may appear larger at higher luminosities.

This result is in agreement with what is found by Egron et al. (2013a) who studied *XMM-Newton*, BeppoSAX, and RXTE spectra of 4U 1705–44 in the hard state and in the soft state. In particular, in the hard state, the inner disk radius as measured by the smearing of the reflection component resulted at $19 - 59$ R_g, which is compatible with the inner disk radius derived in the soft state (13 ± 3

R_g), while more uncertain results came from the evaluation of the blackbody radius in the hard state. D'Aì et al. (2010b) also analyzed the same *XMM-Newton* observation during a hard state used by Egron et al. (2013a). These authors discussed the possibility of a truncated disk in the hard state based on the best fit value of the inner disk radius as found from the Fe line width, which was about 30 R_g, that means about 60 km. However, in that case, the lack of broad–band coverage and the limited statistics, gave a large uncertainty on the inner disk radius, whose 90% c.l. range was from 6 to 90 R_g. Considering the large uncertainty on this measurement we cannot state that the result was in contrast with more recent results (Egron et al., 2013a, and this work). Note also that the best-fit blackbody radius reported by D'Aì et al. (2010b) has a value around 14 ± 5 km, indicating that the disk may be truncated quite close to the NS surface. Similarly, Lin et al. (2010) could not determine with high precision the inner radius of the disk using a diskline model for the Fe line in *Suzaku* and BeppoSAX spectra of 4U 1705–44 taken during a hard state. Therefore, the inner radius of the disk was fixed to 6 R_g, and the fit results, such as Fe line flux and equivalent width, were not sensitive to this parameter.

Similar results for the inner disk radius were obtained also in the case of 4U 1728–34, the prototype of the atoll sources. The *XMM-Newton* spectrum reported by Egron et al. (2011a) taken during a low-luminosity state of the source (probably a hard state) showed a relatively broad iron line (Gaussian $\sigma \sim 0.6$ keV), which was fitted to a series of models (diskline, relline, and reflionx) yielding in all the cases an inner disk radius between 12 and 22 R_g. In this case a blackbody component was not significantly detected. Cackett et al. (2010) present a comprehensive, systematic analysis of *Suzaku* and *XMM-Newton* spectra of 10 NS LMXBs, in order to study their Fe $K\alpha$ emission lines. In most cases they find a narrow range of inner disk radii ($6 - 15$ R_g), implying that the accretion disk extends close to the NS surface over a range of luminosities.

In this respect, it may be useful to compare these results to those obtained for BH X-ray Binaries, since much work has been done to determine the inner radius of the disk in these systems both from the iron line and the reflection component and from the blackbody component (e.g. Done et al., 2007; Reis et al., 2010, and references therein). Also for these systems there is growing evidence that the disk may not be truncated far from the last stable orbit. The broad-band ($0.1 - 200$ keV) BeppoSAX spectrum of one of the best studied galactic BH candidates, Cygnus X–1, taken during a hard state showed evidence of a complex reflection component. In this spectral deconvolution the inner radius of the disk,

as inferred from the smeared reflection, is found between 6 and 20 R_g (Di Salvo et al., 2001a). This result is in agreement with the results of Young et al. (2001) who fitted ASCA, Ginga and EXOSAT data of Cygnus X–1 in both soft and hard spectral states to a model of an ionized accretion disk, whose spectrum is blurred by relativistic effects. They found that relativistic blurring provided a much better fit to the low/hard state and that data of both states were consistent with an ionized thin accretion disk with a reflected fraction of unity extending to the innermost stable circular orbit around the BH (see, however, Barrio et al., 2003, for a different interpretation). Up to date, one of the strongest evidence of a truncated disk, based on Fe line profile measurements, in a BH hard state is that of GX 339-4 (Tomsick et al., 2009). In that case, from *Suzaku* and RXTE spectra, it was found that R_{in} was a factor > 27 higher than in the bright state when the luminosity was about at 0.14% of the corresponding Eddington limit.

More recently Reis et al. (2010) have analyzed a sample of stellar mass BHs, including Cygnus X–1, in the low-hard state, down to luminosities of $\sim 10^{-3}$ L_{Edd}, finding no clear evidence of a truncation of the inner disk at radii larger than 10 R_g. Furthermore, the thermal-disk continuum yields colour temperatures consistent with the relation $L \propto T^4$, implying that the emitting surface is consistent with being constant with luminosity. A similar relation, $L \propto T^{3.2}$, seems also to hold in the case of 4U 1705–44 at least for the soft state (Lin et al., 2010). The authors suggest that the deviation may be caused by a luminosity-dependent spectral hardening factor. On the other hand, the relatively low reflection amplitude ($\Omega/2\pi \simeq 0.34$) we find in the hard state of 4U 1705–44 fitting its spectrum to self-consistent reflection models, such as rfxconv, is compatible with a spherical geometry with the hot (spherical) corona inside an outer accretion disk. In this case, the small inner radius of the disk we find ($R_{in} \sim 17$ R_g, corresponding to approximately $30 - 35$ km for a 1.4 $M_\odot$ NS) would indicate a very compact hot corona filling the central part of the accretion disk, which in the case of a NS may be identified with a boundary layer between the inner accretion disk and the NS surface. This might represent an important difference between BH and NS systems, since for a BH, in the absence of a boundary layer, the inner disk should extend down to the last stable orbit. Note, however, that alternative explanations for this weak reflection cannot be ruled out. This can be caused by a highly ionized inner disk (e.g. Ross et al., 1999) or mildly relativistic outflow of the hot corona away from the disk (Beloborodov, 1999). In the latter case, it was shown that reflection fractions as low as ~ 0.3 can be obtained in the low-hard state without invoking a truncated disk.

In summary, we have analyzed a deep (100 ks exposure time) ToO *Suzaku* observation of 4U 1705–44 during a low-luminosity hard state (corresponding to a luminosity of $\sim$ 3% L_{Edd}). The broad-band spectrum shows a prominent Compton hump at hard energies, a Fe absorption edge and two relatively weak emission lines at $\sim$ 3 and $\sim$ 6.4 keV, identified with fluorescent emission from mildly ionized Ar and neutral Fe, respectively. We used all the available to date self-consistent reflection models to fit these reflection features finding in all cases best-fit parameters that are compatible with each other and consistent with those reported in literature for the soft state. In particular the inclination angles found from the reflection component for the hard and the soft state are perfectly compatible with each other. It is worth noting that we obtain similar smearing parameters in the soft and in the hard state even if in the soft state the reflection component is dominated by the Fe line, while in the hard state other features are dominant. In fact the Fe line is the least important feature in the statistical sense (since the addition of other reflection features, such as the Compton hump plus the Fe edge, gave the most important improvement of the fit). We also find very similar inner disk radii in the hard and soft state, indicating that the inner disk rim does not change significantly at different spectral states down to a luminosity of $\sim$ 3% the Eddington limit.

fig

Chapter 4

A re-analysis of the NuSTAR and XMM-Newton broad-band spectrum of Ser X-1

4.1 Abstract

Context - High resolution X-ray spectra of neutron star Low Mass X-ray Binaries (LMXBs) in the energy range 6.4-6.97 keV, are often characterized by the presence of Kα transition features of iron at different ionization stages. Since these lines are thought to originate by reflection of the primary Comptonization spectrum over the accretion disk, the study of these features allows us to investigate the structure of the accretion flow close to the central source.Thus, the study of these features gives us important physical information on the system parameters and geometry. Ser X-1 is a well studied LMXB which clearly shows a broad iron line. Several attempts to fit this feature as a smeared reflection feature have been performed on *XMM-Newton*, *Suzaku*, *NuSTAR*, and, more recently, on *Chandra* data, finding different results for the inner radius of the disk and other reflection or smearing parameters. For instance, Miller et al. (2013) have presented broad-band, high quality *NuSTAR* data of Ser X-1. Using relativistically smeared self-consistent reflection models,they find a value of R_{in} close to 1.0 R_{ISCO} (corresponding to 6 R_g, where R_g is the Gravitational radius, defined as usual $R_g = GM/c^2$), and a low inclination angle of less than $\sim 10°$.

Aims - Are to probe to what extent the choice of reflection and continuum models (and uncertainties therein) affect conclusions about the disk parameters.

Methods - We use slightly different continuum and reflection models with respect to those adopted in literature for this source. In particular we fit the

iron line and other reflection features with self-consistent reflection models as reflionx (with a power-law illuminating continuum modified with a high energy cutoff to mimic the shape of the incident Comptonization spectrum) and rfxconv. With these models we fit *NuSTAR* and *XMM-Newton* spectra yielding consistent spectral results.

Results - Our results are in line with those already found by Miller et al. (2013) but less extreme. In particular, we find the inner disk radius at $\sim 13\,R_g$ and an inclination angle with respect to the line of sight of $\sim 27°$.

4.2 Introduction

X-ray spectra emitted by Low Mass X-Ray Binaries (LMXBs) of the atoll class (Hasinger and van der Klis, 1989a) are usually characterized by two states of emission: the soft and the hard state. During soft states the spectrum can be well described by a soft thermal component, usually a blackbody or a disk multi-color blackbody, possibly originated from the accretion disk, and a harder component, usually a saturated Comptonization spectrum. In some cases, a hard power-law tail has been detected in the spectra of these sources during soft states both in Z sources (Di Salvo et al., 2000a), and in atoll sources (e.g., Piraino et al., 2007), usually interpreted as Comptonization off a non-thermal population of electrons. On the other hand, during hard states the hard component of the spectrum can be described by a power law with high energy cutoff, interpreted as unsaturated Comptonization, and a weaker soft blackbody component (e.g., Di Salvo et al., 2015a). The hard component is generally explained in terms of inverse Compton scattering of soft photons, coming from the neutron star surface and/or the inner accretion disk, by hot electrons present in a corona possibly located in the inner part of the system, surrounding the compact object (D'Aì et al., 2010a).

In addition to the continuum, broad emission lines in the range 6.4-6.97 keV are often observed in the spectra of LMXBs (see e.g. Cackett et al., 2008; Pandel et al., 2008a; D'Aì et al., 2009a, 2010a; Iaria et al., 2009; Di Salvo et al., 2005a, 2009a; Egron et al., 2013a; Di Salvo et al., 2015a). These lines are identified as Kα transitions of iron at different ionization states and are thought to originate from reflection of the primary Comptonization spectrum over the accretion disk. These features are powerful tools to investigate the structure of the accretion flow close to the central source. In particular, important information can be inferred from the line width and profile, since the detailed profile shape is determined by the ionization state, geometry and velocity field of the emitting plasma (see

e.g. Fabian et al., 1989). Indeed, when the primary Comptonization spectrum illuminates a colder accretion disk, other low-energy discrete features (such as emission lines and absorption edges) are expected to be created by photoionization and successive recombination of abundant elements in different ionization states as well as a continuum emission caused by direct Compton scattering of the primary spectrum off the accretion disk. All these features together form the so-called reflection spectrum, and the whole reflection spectrum is smeared by the velocity-field of the matter in the accretion disk.

Ser X-1 is a persistent accreting LMXB classified as an atoll source, that shows type I X-ray bursts. The source was discovered in 1965 by Friedman et al. (1967). Li et al. (1976) firstly discovered type-I X-ray bursts from this source that was therefore identified as an accreting neutron star. Besides type-I bursts with typical duration of few seconds (Balucinska and Czerny, 1985), a super-burst of the duration of about 2 hours has also been reported (Cornelisse et al., 2002). Recently Cornelisse et al. (2013), analyzing optical spectra collected by the Gran Telescopio Canarias (GTC), detected a two-hours periodicity. They tentatively identified this periodicity as the orbital period of the binary and hence proposed that the secondary star might be a main sequence K-dwarf.

Church and Balucińska-Church (2001) have performed a survey of LMXBs carried out with the *ASCA* satellite. The best-fit model used by these authors to fit the spectrum of Ser X-1 was a blackbody plus a cutoff power-law with a Gaussian iron line. Oosterbroek et al. (2001) have analyzed two simultaneous observations of this source collected with BeppoSAX and RXTE. The authors fitted the broad-band (0.1-200 keV) BeppoSAX spectrum with a model consisting of a disk blackbody, a reflection component described by the XSPEC model pexrav, and a Gaussian line. However, in that case the improvement in χ^2 with respect to a model consisting of a blackbody, a Comptonization spectrum modeled by compST, and a Gaussian was not significant, and therefore it was not possible to draw any definitive conclusion about the presence of a reflection continuum.

Bhattacharyya and Strohmayer (2007) carried out the analysis of three *XMM-Newton* observations of this system. They managed to fit the EPIC/pn spectrum with a model consisting of disk blackbody, a Comptonization continuum modeled with compTT and a diskline, i.e. a Gaussian line distorted and smeared by the Keplerian velocity field in the accretion disk (Fabian et al., 1989). They found strong evidence that the Fe line has an asymmetric profile and therefore that the line originates from reflection in the inner rim of the accretion disk. Fitted with a Laor profile (Laor, 1991), the line shape gave an inner disk radius of

$4 - 5\,R_g$ or $16\,R_g$ (depending from the observation) and an inclination angle to the binary system of $40 - 50°$. Cackett et al. (2008), from data collected by *SUZAKU*, performed a study of the iron line profiles in a sample of three LMXBs including Ser X-1. From the analysis of XIS and PIN spectra, they found a good fit of the broad-band continuum using a blackbody, a disk blackbody and a power-law. Two years later Cackett et al. (2010) re-analyzed *XMM-Newton* and *SUZAKU* data of a sample of 10 LMXBs that includes Ser X-1, focusing on the iron line - reflection emission. In particular, for Ser X-1, they analyzed 4 spectra: three Epic-PN spectra obtained with *XMM-Newton* and one obtained with the XIS and the PIN instruments on board of *SUZAKU*. Initially, they fitted the spectra of the continuum emission using a phenomenological model, consisting of a blackbody, a disk-blackbody and a power-law. Then, they started the study of the Fe line adding first a diskline component and after a reflection component convolved with `rdblur` (that takes into account smearing effects due to the motion of the emitting plasma in a Keplerian disk). They obtained different results for the smearing parameters both for different observations and for different models used on the same observation. For sake of clarity these results are summarized in Table 4.1.

Miller et al. (2013) analyzed two NuSTAR observations carried out on July 2013. They fitted the continuum emission using a model consisting of a blackbody, a disk blackbody and a power-law. With respect to this continuum model, evident residuals were present around 6.40-6.97 keV, suggesting the presence of a Fe line. Therefore they added a `kerrdisk` component to the continuum to fit the emission line, taking into account a possible non-null spin parameter for the neutron star. They also tried to fit the reflection spectrum (i.e. the iron line and other expected reflection features) with the self-consistent reflection model `reflionx`, a modified version of reflionx calculated for a blackbody illuminating spectrum, convolved with the `kerrconv` component. The addition of the reflection component gave a significant improvement of the fit. In most cases the best fit gave low inclination angles (less than $\sim 10°$), in agreement with recent optical observations (Cornelisse et al., 2013), inner disk radii compatible with the Innermost Stable Circular Orbit (ISCO), corresponding to about 6 Rg for small values of the spin parameter, a ionization parameter $\log \xi \sim 2.3 - 2.6$, and a slight preference for an enhanced iron abundance. The fit resulted quite insensitive to the value of the adimensional spin parameter, a, of the neutron star.

More recently, Chiang et al. (2016a) analysed a recent 300 ks Chandra/HETGS observation of the source performed in the "continuous clocking" mode and thus

free of photon pile-up effects. They fitted the continuum with a combination of multicolor disk blackbody, blackbody and power-law. The iron line was found significantly broader than the instrumental energy resolution and fitting this feature with a diskline instead of a broad Gaussian gave a significant improvement of the fit. They also tried self-consistent reflection models, namely the reflionx model with a power-law continuum as illuminating source and xillver (see e.g. García et al., 2013), to describe the iron line and other reflection features, yielding consistent results. In particular, this analysis gave a inner radius of $\sim 7-8$ R_g and an inclination angle of about 30 deg.

As described above, different continuum models were used to fit the spectrum of Ser X-1 observed with various instruments at different times. In Table 4.1 we summarize the results of the spectral analysis of this source obtained from previous studies, and in particular the results obtained for the iron line and the reflection model. Quite different values have been reported for the inclination angle (from less than 10 deg to about 40 deg), for the inner disk radius (from 4 to more than 100 R_g) and for the iron line centroid energy and/or the ionization parameter $\log \xi$ indicating that the disk is formed by neutral or very highly ionized plasma.

In this chapter we re-analyzed all the available public *NuSTAR* observations of Ser X-1, fitting the iron line and other reflection features with both phenomenological and self-consistent reflection models. These data were already analysed by Miller et al. (2013) using a different choice of the continuum and reflection models. We compare these results with those obtained from three *XMM-Newton* observations (already analyzed by Bhattacharyya and Strohmayer, 2007) fitted with the same models. We choose to re-analyse *NuSTAR* and *XMM-Newton* spectra because these instruments provide the largest effective area available to date, coupled with a moderately good energy resolution, at the iron line energy, and a good broad-band coverage. Moreover, the source showed similar fluxes during the *NuSTAR* and *XMM-Newton* observations. Note also that *NuSTAR* is not affected by pile-up problems in the whole energy range. The spectral results obtained for *NuSTAR* and *XMM-Newton* are very similar to each other and the smearing parameters of the reflection component are less extreme than those found by Miller et al. (2013), and in good agreement with the results obtained from the Chandra observation (Chiang et al., 2016a). In particular we find an inner disk radius in the range $10-15\,R_g$ and an inclination angle with respect to the line of sight of $25-30°$.

4.3 Observations and Data Reduction

In this chapter we analyze data collected by the *NuSTAR* satellite. Ser X-1 has been observed twice with *NuSTAR*, obsID: 30001013002 (12-JUL-2013) and obsID: 30001013004 (13-JUL-2013). The exposure time of each observation is about 40 ksec. The data were extracted using NuSTARDAS (NuSTAR Data Analysis Software) v1.3.0. Source data have been extracted from a circular region with 120" radius whereas the background has been extracted from a circular region with 90" radius in a region far from the source. First, we run the "nupipeline" with default values of the parameters as we aim to get "STAGE 2" events clean. Then spectra for both detectors, FPMA and FPMB, were extracted using the "nuproducts" command. Corresponding response files were also created as output of nuproducts. A comparison of the FPMA and FPMB spectra, indicated a good agreement between them. To check this agreement, we have fitted the two separate spectra with all parameters tied to each other but with a constant multiplication factor left free to vary. Since the value of this parameter is 1.00319 ± 0.00145, our assumption is basically correct. Following the same approach described in Miller et al. (2013), we have therefore created a single added spectrum using the "addascaspec" command. A single response file has been thus created using "addrmf", weighting the two single response matrices by the corresponding exposure time. In this way, we obtain a summed spectrum for the two *NuSTAR* observations and the two *NuSTAR* modules. We fitted this spectrum in the 3-40 keV energy range, where the emission from the source dominates over the background.

We have also used non-simultaneous data collected with XMM-Newton satellite on March 2004. The considered obsID are 0084020401, 0084020501 and 0084020601. All observations are in Timing Mode and each of them has a duration of ~ 22 ksec. We extracted source spectra, background spectra and response matrices using the SAS (Science Analysis Software) v.14 setting the parameters of the tools accordingly. We produced a calibrated photon event file using reprocessing tools "epproc" and "rgsproc" for PN and RGS data respectively. We also extracted the MOS data; these were operated in uncompressed timing mode. However, the count rate registered by the MOS was in the range $290 - 340$ c/s, which is above the threshold for avoiding deteriorated response due to photon pile-up. The MOS spectra indeed show clear signs of pile-up and we preferred not to include them in our analysis, since these detectors cover the same energy range of the PN.

Before extracting the spectra, we filtered out contaminations due to back-

ground flares detected in the 10-12 keV Epic PN light-curve. In particular we have cut out about 600 sec for obsID 0084020401, about 800 sec for obsID 0084020501 and finally about 1600 sec for obsID 0084020601. In order to remove the flares, we applied time filters by creating a GTI file with the task "tabgtigen". In order to check for the presence of pile-up we have run the task "epatplot" and we have found significant contamination in each observation. The count-rate registered in the PN observations was in the range 860-1000 c/s that is just above the limit for avoiding contamination by pile-up. Therefore, we extracted the source spectra from a rectangular region (RAW X$\geq$26) and (RAW X$\leq$46) including all the pixels in the y direction but excluding the brightest columns at RAW X = 35 and RAW X = 36. This reduced significantly the pile up (pile up fraction below a few percent in the considered energy range).

We selected only events with PATTERN $\leq$ 4 and FLAG=0 that are the standard values to remove spurious events. We extracted the background spectra from a similar region to the one used to extract the source photons but in a region away from the source included between (RAWX$\geq$1) and (RAWX$\leq$6). Finally, for each observation, using the task 'rgscombine' we have obtained the added source spectrum RGS1+RGS2, the relative added background spectrum along with the relative response matrices. We have fitted RGS spectrum in the 0.35-1.8 keV energy range, whereas the Epic-PN in the 2.4-10 keV energy range. We have discarded PN data below 2.4 keV because of the presence of systematics which are particularly evident for bright sources (Di Salvo et al., 2009a).

Spectral analysis has been performed using XSPEC v.12.8.1 (Arnaud, 1996). For each fit we have used the `phabs` model in XSPEC to describe the neutral photoelectric absorption due to the interstellar medium with photoelectric cross sections from Verner et al. (1996) and element abundances from Wilms et al. (2000a). For the *NuSTAR* spectrum, which lacks of low- energy coverage up to 3 keV, we fixed the value of the equivalent hydrogen column, N_H, to the same value adopted by Miller et al. (2013), namely $N_H = 4 \times 10^{21}$ cm^{-2} (Dickey and Lockman, 1990), while for the XMM-Newton spectrum we left this parameter free to vary in the fit, finding a slightly higher value (see Tab. 4.2 and 4.3). As a further check, we have fitted the NuSTAR spectrum fixing N_H to the same value found for the XMM spectrum, but the fit parameters did not change significantly.

4.4 Spectral Analysis

4.4.1 *NuSTAR* spectral analysis

The *NuSTAR* observations caught the source in a high-luminosity ($\sim 10^{38}$ erg/s, Miller et al. (2013)) state, therefore most probably in a soft state. As seen in other similar atoll sources, the spectrum of Ser X-1 is characterized by a soft component (i.e. blackbody), interpreted as thermal emission from the accretion disk, a hard component (i.e. a Comptonization spectrum), interpreted as saturated Comptonization from a hot corona, and often by the presence of a broad iron emission line at $6.4 - 6.97$ keV depending on the iron ionization state. We used the Comptonization model `nthComp` (Życki et al., 1999a) in XSPEC, with a blackbody input seed photon spectrum, to fit the hard component. We used a simple blackbody to describe the soft component. Substituting the blackbody with a multicolor disk blackbody, `diskbb` in XSPEC, gives a similar quality fit and the best-fit parameters do not change significantly.

To fit the iron line we first tried simple models such as a Gaussian profile or a `diskline` (Fabian et al., 1989). The best-fit parameters, obtained using alternatively a Gaussian or diskline profile, are in good agreement with each other (see Tab. 4.2). Using a `diskline` instead of a Gaussian profile we get an improvement of the fit corresponding to $\Delta\chi^2 = 54$ for the addition of two parameters. Spectra, along with the best-fit model and residuals are shown in Fig.4.1. In both cases, the fit results are poor (the relative null hypothesis probability is 2.8×10^{-8}; the reduced χ^2 are still relatively large, and evident residuals are present, especially above 10 keV, see Fig.4.1).

In order to fit the residuals at high energy, we added a `powerlaw` component (a hard tail) to all the models described above. A hard power-law tail is often required to fit high-energy residuals of atoll sources in the soft state (see e.g. Pintore et al., 2015a, 2016a; Iaria et al., 2001, 2002), and this component may also be present in the spectrum of Ser X-1 (see Miller et al., 2013). Unless it is specified otherwise, for every fit, we froze the power-law photon index to the value found by Miller et al. (2013) for Ser X-1, that is 3.2. The new models are now called *gauss-pl* and *diskline-pl*, respectively. The new best fit parameters are reported in Tab 4.2. While the best-fit parameters do not change significantly with the addition of this component, we get an improvement of the fit corresponding to a reduction of the χ^2 by $\Delta\chi^2 = 123$ (for the model with a Gaussian line profile) and $\Delta\chi^2 = 113$ (for the model with a diskline profile) for the addition of one parameter, respectively. The probabilities of chance improvement of the fit are 8.5×10^{-24} and 8.6×10^{-23},

respectively. Some residuals are still present between 10 and 20 keV probably caused by the presence of an unmodeled Compton hump. Note that the soft blackbody component remains significant even after the addition of the power-law component. If we eliminate this component from the fitting model we get a worse fit, corresponding to a decrease by $\Delta\chi^2 = 245$ for the addition of two parameters when the soft component is included in the fit and a probability of chance improvement of the fit of $\sim 3 \times 10^{-44}$.

4.4.2 Reflection models

We have also tried to fit the *NuSTAR* spectrum of Ser X-1 with more sophisticated reflection models, performing a grid of fit with self-consistent models such as `reflionx` or `rfxconv`. Reflionx and rfxconv models both include the reflection continuum, the so called Compton hump caused by direct Compton scattering of the reflected spectrum, and discrete features (emission lines and absorption edges) for many species of atoms at different ionization stages (Ross and Fabian, 2005b; Kolehmainen et al., 2011a).

The `reflionx` model depends on 5 parameters, that are the abundance of iron relative to the solar value, the photon index of the illuminating power-law spectrum (Γ, ranging between 1.0 to 3.0), the normalization of reflected spectrum, the redshift of the source, and the ionization parameter $\xi = L_X/(n_e r^2)$ where L_X is the X-ray luminosity of the illuminating source, n_e is the electron density in the illuminated region and r is the distance of the illuminating source to the reflecting medium. When using `reflionx`, which uses a power-law as illuminating spectrum, in order to take into account the high-energy roll over of the Comptonization spectrum, we have multiplied it by a high-energy cutoff, `highecut`, with the folding energy E_{fold} set to 2.7 times the electrons temperature kT_e and the cutoff energy E_{cutoff} tied to 0.1 keV. In this way we introduce a cutoff in the reflection continuum, which otherwise resembles a power-law. The cut-off energy fixed at 2.7 times the electron temperature of the Comptonization spectrum (assumed to be similar to a blackbody spectrum), is appropriate for a saturated Comptonization (see e.g. Egron et al., 2013a). To fit the Comptonization continuum we used the `nthComp` model. Moreover we fixed the photon index of the illuminating spectrum, Γ, to that of the `nthComp` component. We stress out that in our analysis we use a different `reflionx` reflection model with respect to that used by Miller et al. (2013). In fact we used a model that assumes an input power-law spectrum as the source of the irradiating flux modified, in order to mimic the nthcomp continuum, by introducing the model component

`highecut`. Miller et al. (2013) instead used a modified version of reflionx calculated for a blackbody input spectrum, since that component dominates their phenomenological continuum.

`rfxconv` is an updated version of the code in Done and Gierliński (2006), using Ross and Fabian (2005b) reflection tables. This is a convolution model that can be used with any input continuum and has therefore the advantage to take as illuminating spectrum the given Comptonization continuum. It depends on 5 parameters: the relative reflection fraction (rel-refl defined as $\Omega/2\pi$, namely as the solid angle subtended by the reflecting disk as seen from the illuminating corona in units of 2π), the cosine of the inclination angle, the iron abundance relative to the Solar value, the ionization parameter Log ξ of the accretion disk surface, and the redshift of the source.

Due to its high velocities, the radiation re-emitted from the plasma located in the inner accretion disk undergoes Doppler and relativistic effects (which smears the whole reflection spectrum). In order to take these effects into account we have convolved the reflection models with the `rdblur` component (the kernel of the diskline model), which depends on the values of the inner and outer disk radii, in units of the Gravitational radius ($R_g = GM/c^2$), the inclination angle of the disk (that was kept tied to the same value used for the reflection model), and the emissivity index, Betor, that is the index of the power-law dependence of the emissivity of the illuminated disk (which scales as r^{Betor}). Finally, we have also considered the possibility that neutron star has a spin. In this case, the reflection component has been convolved with the `Kerrconv` component (Brenneman and Reynolds, 2006) that through its adimensional spin parameter 'a' allowed us to implement a grid of models exploring different values of 'a' (see Section 4.8). For this model there is also the possibility to fit the emissivity index of the inner and outer part of the disk independently, although in our fits we used the same emissivity index for the whole disk. For all the fits we have fixed the values of R_{out} to 2400 R_g, the iron abundance to solar value, Fe/solar = 1, and the redshift of the source to 0. The best fit parameters are reported in Tab 4.2–4.5.

We started to fit the data adding a reflection component, `reflionx` or `rfxconv`, convolved with the blurring component `rdblur`, to the continuum model given by the blackbody and the nthcomp components (models are called *rdb-reflio* and *rdb-rfxconv*, respectively). Fit results for both models are acceptable, with χ^2_{red} close to 1.09. There are a few differences between the best-fit parameters of the rdb-reflio model with respect to those of the rdb-rfxconv model. In particular the *rdb-rfxconv* model gives a lower value of R_{in}, while the *rdb-reflio* model gives a

higher ionization parameter (although with a large uncertainty). Spectra, along with the best-fit model and residuals are reported in Fig.4.1. The residuals that are very similar for the two models, apart for the 8-10 keV energy range where *rdb-reflio* model shows flatter residuals than *rdb-rfxconv* model (see Fig. 4.2).

As before, we also tried to add a power-law component to the models obtained by the convolution of the blurring component (rdblur) with the two different reflection components (rfxconv or reflionx). The two new models are called *rdb-rfxconv-pl* and *rdb-reflion-pl*, respectively. In both cases we get a significant improvement of the fit, with $\Delta\chi^2 = 90$ for the addition of two parameters and $\Delta\chi^2 = 66$ for the addition of one parameter, respectively. In these cases, an F-test yields a probability of chance improvement of 3.1×10^{-15} for *rdb-reflion-pl* and 6.1×10^{-19} for *rdb-rfxconv-pl* model, respectively. Spectra, along with best-fit model and residuals are reported in Fig. 4.2, whereas values of the best-fit parameters are listed in Tab. 4.3. Residuals are now flat (see plots reported in upper panels of Fig. 4.2). Note also that in this way we get more reasonable values of the best-fit parameters, especially for the ionization parameter, $\log \xi$, which is around 2.7 for both models, in agreement with the centroid energy of the iron line at about 6.5 keV, and well below 3.7 (a ionization parameter $\log \xi \sim 3.7$ would imply that the matter of the accretion disk would be fully ionized).

In summary, the best fit of the *NuSTAR* spectrum of Ser X-1 is obtained fitting the continuum with a soft blackbody component, a Comptonization spectrum, and a hard power-law tail and fitting the reflection features with the `rfxconv` model smeared by the `rdblur` component, since the fitting results are quite insensitive to the value of the spin parameter a (see Section 4.8). This fit, corresponding to a $\chi^2(dof) = 912.5(911)$, gives a blackbody temperature of $\simeq 0.54$ keV, a temperature of the seed photons for the Comptonization of $\simeq 0.93$ keV, an electron temperature of the Comptonizing corona of $\simeq 2.70$ keV and a photon index of the primary Comptonized component of $\simeq 2.17$, whereas the photon index of the hard power-law tail is steeper, around 3.2. The reflection component gives a reflection amplitude (that is the solid angle subtended by the accretion disk as seen from the Comptonizing corona) of $\simeq 0.24$ and a ionization parameter of $\log \xi \simeq 2.7$. The smearing of the reflection component gives an inner disk radius of R_{in} ranging between 10 and 16 R_g, and inclination angle of the disk with respect to the line of sight of $i \simeq 27°$, and the emissivity of the disk scaling as $\propto r^{-2.6\pm0.2}$. Note that the Compton hump is highly significant. To evaluate its statistical significance we can compare the best fit obtained with the model diskline-pl with the best fit given by the model rdb-rfxconv-pl (the main

difference between the two models is in fact that rfxconv contains the reflection continuum and diskline does not). Using rfxconv instead of diskline we get a decreases of the χ^2 by $\Delta\chi^2 = 87$ for the addition of 1 parameter and an F-test probability of chance improvement of 8×10^{-20}, which is statistically significant.

4.4.3 XMM-Newton Spectral Analysis

We have also carried out the analysis of *XMM-Newton* observations of Ser X-1. A previous study, based only on the PN data analysis, has been reported by Bhattacharyya and Strohmayer (2007). We updated the analysis by performing the fit of the RGS spectra in the 0.35–1.8 keV energy range and the PN spectra in the 2.4–10 keV energy range. Following the same approach used for the analysis on *NuSTAR* data, we assumed a continuum model composed of a blackbody, a hard power-law and the nthComp component. In addition to the continuum components described above, we have also detected several discrete features present in all RGS spectra, both in absorption and in emission that were supposed to be of instrumental origin by Bhattacharyya and Strohmayer (2007). The energies of the most intense features detected in our spectra lie between 0.5 keV and 0.75 keV. To fit these features we have therefore added three additional gaussians to our model: two absorption lines at 0.528 keV and at 0.714 keV, respectively, and one in emission at 0.541 keV. To this continuum we first added a diskline (model called *diskline-pl-xmm*, see Table 4.2) to fit the iron line profile. Then we fitted the spectra substituting the diskline with the self-consistent reflection model that gave the best fit to the *NuSTAR* data, that is 'rfxconv', convolved with the smearing component 'rdblur' (model called *rdb-rfxconv-pl-xmm*, results are reported in Table 4.3).

We have performed the fit of the spectrum obtained from these three observations simultaneously, tying parameters of the RGS with the all parameters of the PN from the same observation. The spectra of the three XMM observations are very similar with each other, except for the soft black body temperature that was left free to vary in different datasets. Values of the best-fit parameters of the model *diskline-pl-xmm* result to be in good agreement with what we have found from the fit of the *NuSTAR* spectra with the same model.

We have also performed the fit with a model including the reflection component `rfxconv`, called *rdb-rfxconv-pl-xmm*. As before, in order to take into account structures visible in the RGS spectra, we have added three gaussians to the model. As before we have tied parameters of the RGS to the corresponding parameters of the PN from the same observation except for the parameter kT_{bb} that was

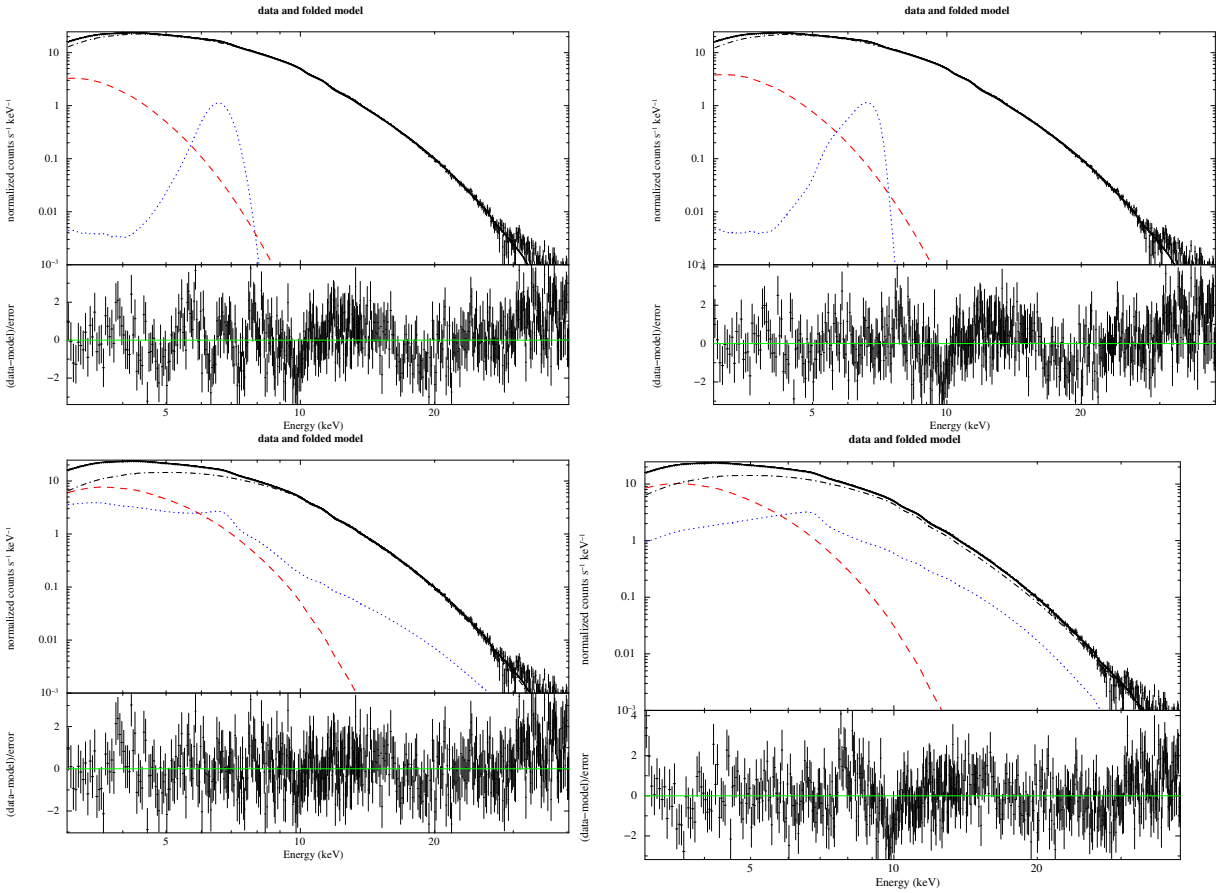

Figure 4.1: NuSTAR spectra of Ser X-1 and best-fitting model together with residuals in units of sigma for the corresponding model. These are: *Top left*: 'gauss' — *Top right*: 'diskline' — *Bottom left*: 'rdb-reflio' — *Bottom right*: 'rdb-rfxconv'. Dashed lines indicate the black-body component, dotted lines indicate the reflection components (i.e. the Gaussian or Diskline profile for the iron line, top panels, or the self-consistent reflection component, bottom panels, respectively), and the dashed-dotted lines indicate the comptonized component.

left free to vary among the three observations. Note also that for these fits the inclination angle is fixed to the corresponding values we found from the *NuSTAR* spectra. Results are reported in Table 4.3, and are in good agreement with those obtained for the *NuSTAR* spectrum.

4.5 Discussion

Ser X-1 is a well studied LMXB showing a broad emission line at $6.4 - 6.97$ keV interpreted as emission from iron at different ionization states and smeared by Doppler and relativistic effects caused by the fast motion of matter in the

inner accretion disk. Moderately high energy resolution spectra of this source have been obtained from *XMM-Newton*, *Suzaku*, *NuSTAR*, and *Chandra*. However, as described in Sec. 4.2, spectral results for the reflection component are quite different for different observations or for different models used to fit the continuum and/or the reflection component. While spectral differences in different observations may be in principle justified by intrinsic spectral variations of the source, differences caused by different continuum or reflection models should be investigated in detail in order to give a reliable estimate of the parameters of the system. For instance, in a recent *NuSTAR* observation analyzed by Miller et al. (2013), assuming a modified version of `reflionx` calculated for a blackbody input spectrum, the authors report a significant detection of a smeared reflection component in this source, from which they derive an inner radius of the disk broadly compatible with the disk extending to the ISCO (corresponding to 6 Rg in the case $a = 0$) and an inclination angle with respect to the line of sight $< 10°$. On the other hand, Chiang et al. (2016a), analysing a recent 300 ks-*Chandra/HETGS* observation of the source obtained a high-resolution X-ray spectrum which gave a inner radius of $R_{in} \sim 7 - 8\, R_g$ and an inclination angle of $\sim 30°$.

In this chapter we analyzed all the available *NuSTAR* and *XMM-Newton* observations of Ser X-1. These observations have been already analyzed by Miller et al. (2013) and Bhattacharyya and Strohmayer (2007), respectively, who used different continuum and reflection models and report different results for the reflection component. The same *XMM-Newton* observations have also been analyzed by Cackett et al. (2010) who also report different results for the reflection component, with higher inner disk radii (between 15 and more than 45 R_g) and quite low inclination angles ($< 10°$) when using a blurred reflection model, and inclination angle between 10 and 35° when using a diskline component to fit the iron line profile (see Tab. 4.1 for more details). We have shown that we can fit the *NuSTAR* and *XMM-Newton* spectra independently with the same continuum model and with a phenomenological model (i.e. diskline) or a self-consistent reflection model (i.e. reflionx or rfxconv) for the reflection component, finding in all our fits similar (compatible within the associated uncertainties) smearing parameters for the reflection component.

To fit these spectra we have used a continuum model composed by a blackbody component (bbody) and a comptonization continuum (nthcomp), which has been widely used in literature to fit the spectra of neutron star LMXBs both in the soft and in the hard state (see e.g. Egron et al., 2013a). With respect to

the continuum model used by Miller et al. (2013) we have substituted one of the two blackbody components, the hottest one, with a Comptonization spectrum. Since this component gives the most important contribution to the source flux, especially above 5 keV, we have subsequently used this component as the source of the reflection spectrum. In all our fits the addition of a hard power-law component, with a photon index ~ 3 significantly improved the fit. The presence of a hard power-law component is often found in the spectra of bright LMXBs in the soft state (see e.g. Piraino et al., 2007; Pintore et al., 2015a, 2016a), and has been interpreted as comptonization of soft photons off a non-thermal population of electrons (see e.g. Di Salvo et al., 2000a).

To fit the reflection component, which is dominated by a prominent iron line, we have first used a phenomenological model consisting of a Gaussian line or a diskline, with a diskline providing a better fit than a Gaussian profile (cf. fitting results reported in Table 4.2). All the diskline parameters obtained from the fitting of the *NuSTAR* and *XMM-Newton* spectra are compatible with each other, except for the line flux which appears to be lower during the *XMM-Newton* observations.

In order to fit the reflection spectrum with self-consistent models, which take into account not only the iron line but also other reflection features, we have used both `reflionx` and `rfxconv` reflection models. In both these models, emission and absorption discrete features from the most abundant elements are included, as well as the reflected continuum. We have convolved the reflection spectrum with the relativistic smearing model `rdblur`, taking into account Doppler and relativistic effects caused by the fast motion of the reflecting material in the inner accretion disk. We have also investigated the possibility that the neutron star has a significant spin parameter. We have therefore performed a grid of fits using the `kerrconv` smearing model, instead of rdblur, freezing the spin parameter 'a' at different values: 0, 0.12, 0.14 and letting it free to vary in an additional case (see Section 4.8 for more details). In agreement with the results reported by Miller et al. (2013) we find that the fit is almost insensitive to the spin parameter but prefers low values of the spin parameter ($a < 0.04$).

The results obtained using `reflionx` or `rfxconv` are somewhat different in the fits not including the hard power-law component. However, the reflection and smearing parameters become very similar when we add this component to the continuum model (cf. results in Tabs. 4.3, 4.4, 4.5). The addition of this component also significantly improves all the fits. We consider as our best fit model the one including the hard power-law component, `rfxconv` as reflection

component smeared by the `rbdblur` component (model named `rdb-rfxconv-pl` in Tab. 4.3). The fit of the *XMM-Newton* spectra with the same model gave values of the parameters that overall agree with those obtained fitting the *NuSTAR* spectra. In this case, we have found values of the ionization parameter $\log(\xi)$ ranging between 2.58 and 2.71 (a bit higher, around 3, for the *XMM-Newton* spectra) and reflection amplitudes between 0.2 and 0.3, indicating a relatively low superposition between the source of the primary Comptonization continuum and the disk (a value of 0.3 would be compatible with a spherical geometry of a compact corona inside an outer accretion disk). For the smearing parameters of the reflection component we find values of the emissivity index of the disk ranging from -2.8 to -2.48, an inner radius of the disk from 10.6 to 16.2 R_g, and an inclination angle of the system with respect to the line of sight of $25 - 30°$. In our results the inclination angle is higher than what found by Miller et al. (2013) (who report an inclination angle less than 10°), but is very similar to that estimated from Chandra spectra ($25 - 35°$, see Chiang et al. (2016a). Moreover, the inner disk radius we find is not compatible with the ISCO. Assuming a 1.4 $M_\odot$ for the neutron star, the inner radius of the disk is located at $22 - 34$ km from the neutron star center. Note that this value is compatible with the estimated radius of the emission region of the soft blackbody component, which is in the range $19 - 31$ km. We interpret this component as the intrinsic emission from the inner disk since this is the coldest part of the system and because the temperature of the blackbody component appears to be too low to represent a boundary layer.

4.6 Conclusions

We have carried out moderate energy resolution, broad-band spectral analysis of the atoll type LMXB Serpens X-1 using data collected by *NuSTAR* and *XMM-Newton* satellites. These data have been already analyzed in literature. In particular Miller et al. (2013) have analyzed the *NuSTAR* spectra and have obtained a low inclination angle of about 8°, an inner disk radius compatible with the ISCO, a ionization parameter $\log \xi$ between 2.3 and 2.6 along with an iron abundance of about 3.

In the following we summarize the results presented in this thesis:

- We have performed the fitting using slightly different continuum and reflection models with respect to that used by other authors to fit the X-ray spectrum of this source. Our best fit of the *NuSTAR* spectrum of Ser X-1

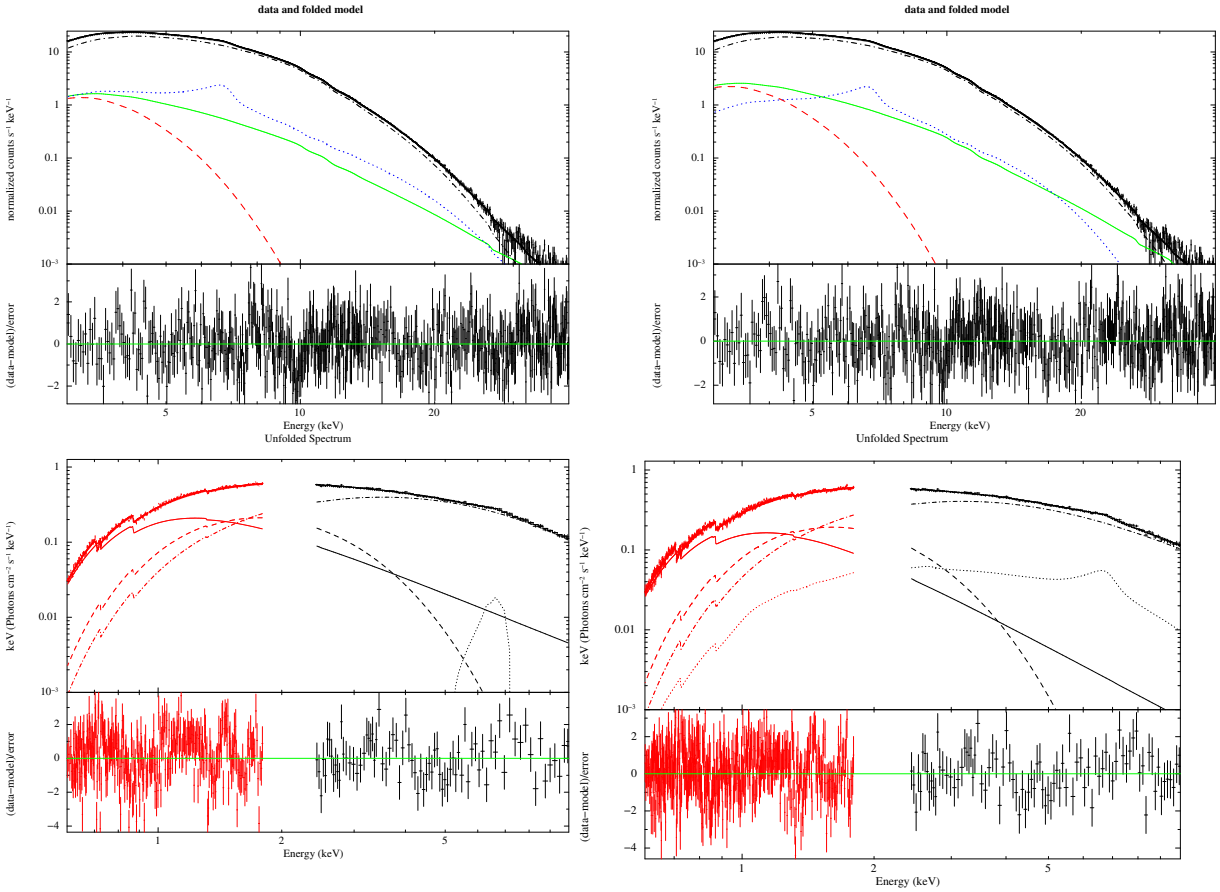

Figure 4.2: *Top panels*: NuSTAR spectra of Ser X-1 and best-fitting model together with residuals in units of sigma for the corresponding model. These are: *Top left*: 'rdb-reflio-pl' — *Top right*: 'rdb-rfxconv-pl'. Bottom panels: XMM-Newton spectra and best-fitting model together with residuals in units of sigma for the corresponding model. These are: *Bottom left*: 'diskline-pl-xmm' — *Bottom right*: 'rdb-rfxconv-pl-xmm'. For clarity only the first XMM-Newton observation is shown. Dashed lines indicate the black-body component, dotted lines indicate the reflection components (i.e. the Diskline profile for the iron line or the self-consistent reflection component), the solid line indicates the power-law component, and the dashed-dotted lines indicate the comptonized component.

is obtained fitting the continuum with a soft blackbody, a Comptonization spectrum, a hard power-law tail in addition to the reflection features. To fit the reflection features present in the spectrum we used both empirical models and self-consistent reflection components as `reflionx` and `rfxconv`, as well as two different blurring components that are `rdblur` and`kerrconv`. From the analysis carried out using kerrcov we have obtained that our fit is insensitive to the value assumed by the adimensional spin parameter 'a', in agreement with what is found by Miller et al. (2013) in their analysis.

- As regards the reflection features, we obtain consistent results using phenomenological models (such as diskline) or self-consistent models to fit the *NuSTAR* spectrum of the source. In particular, the reflection component gives a reflection amplitude of $\Omega/2\pi \sim 0.2 - 0.3$ (where Ω is the solid angle of the disk as seen from the corona in units of 2π) and a ionization parameter of $\log(\xi) \sim 2.6 - 2.7$. The smearing of the reflection component gives an inner disk radius of $R_{in} \sim 10.6 - 16.2\, R_g$, an emissivity index of the disk in the range $-(2.5 - 2.8)$, whereas the inclination angle of the disk with respect to the line of sight results in the range $25 - 29°$. We note that the inner disk radius derived from the reflection component results compatible with the radius inferred from the soft blackbody component, which results in the range $19 - 31$ km.

- Also, the analysis of *XMM-Newton* spectra, carried out using the same models adopted to fit the *NuSTAR* spectra, gave values of the parameters compatible to those described above, although the two observations are not simultaneous. The only differences are the reflection amplitude, $\Omega/2\pi \sim 0.18 - 0.19$, which results slightly lower, although still marginally consistent within the errors, and the ionization parameter, $\log(\xi) \sim 2.9 - 3.1$, which results somewhat higher with respect to the non-simultaneous *NuSTAR* observations.

In conclusion, performing a detailed spectral analysis of *NuSTAR* and *XMM-Newton* data of LMXB Ser X-1 using both phenomenological and self-consistent reflection models, and using a continuum model somewhat different from that used in literature for this source, our best fit parameters are in broad agreement with the findings of Miller et al. (2013) although we find values of the inner disk and the inclination angle that are less extreme.

The aim of the present work is basically to test the robustness of reflection fits of neutron star LMXBs by using the best available data for Ser X-1, a particular

neutron star with a very clear reflection spectrum that has been studied with several instruments.

4.7 Final Remarks

In this chapter we performed an investigation of to which extent imporant disk parameters inferred from reflection fitting depend on the chosen spectral models for both the continuum and the reflection. Despite the fact that authors from previous work have used basically the same continuum componet model, the results of parameter reflections, as R_{in}, $\log(\xi)$, and the inclination angle are scattered over large ranges. In this thesis we re-analyzed all the available public *NuSTAR* observations of Ser X-1, fitting , the continuum with a different model and the iron line with self-consistent reflection models

4.8 Models including `kerrconv`

From the spectral analysis described in Sec. 4.4.1, we find that our best fit obtained using `rdblur` as smearing component gives a soft blackbody temperature of 0.54±0.06 keV and a radius of the emitting region of 25 ± 6 km, a temperature of the seed photons for the Comptonization of 0.93±0.07 keV, an electron temperature of the Comptonizing corona of 2.70±0.04 keV and a photon index of the primary Comptonized component of 2.17±0.04, whereas the photon index of the hard power-law tail is steeper, around 3.2. The reflection component gives a reflection amplitude of 0.24±0.04 and a ionization parameter of $\log(\xi) = 2.69^{+0.02}_{-0.11}$. Finally, the smearing of the reflection component gives an inner disk radius of $R_{in} = 13.4 \pm 2.8 R_g$, compatible with the radius inferred from the blackbody component, and an emissivity index of the disk equal to -2.64±0.16, whereas the inclination angle of the disk with respect to the line of sight results equal to 27.1±1.9°. The analysis of *XMM-Newton* spectra, carried out using the same models adopted to fit the *NuSTAR* spectra, gave values of the parameters compatible to those described above, although the two observations are not simultaneous. In particular in this case we find R_{in} $14.2^{+9.5}_{-4.6}$ R_g, a reflection amplitude of 0.183±0.003 and an ionization parameter of $\log(\xi) = 3.04 \pm 0.11$, a temperature of the seed photons in the range $0.76 - 0.85$ keV, a photon index of the primary Comptonized component of 2.45±0.22 keV. In other words, the *XMM-Newton* spectra independently confirm the results obtained for the *NuSTAR* spectra.

In order to check the presence of a non-null spin parameter of the neutron

Table 4.1: Results of Spectral Analysis of Ser X-1 from Previous Studies

Instrument	Continuum Model	Reflection Model	Line Model	Line Energy (keV)	Equivalent width	R_{in} (R_g)	Incl (deg)	Emissivity index log (ξ)	Flux (ergs/cm^2/sec)	Reference
ASCA	bbody+cutpowerlaw	—	gaussian	6.6 ± 0.17	81 eV	—	—	—	—	Ref(1)
RXTE	bbody	pexrav	gaussian	–	–	—	—	—	—	Ref(2)
BeppoSAX	bbody+compTT	—	gaussian	$6.46\ ^{+0.12}_{-0.14}$	$275\ ^{75}_{-55}$ eV	—	—	—	—	Ref(2)
XMM-Newton	diskbb+compTT	—	laor	$6.40\ ^{+0.08}_{-0.00}$	86-105 eV	4-16	40-50	—	2-10 keV: (3.3-4.2)×10^{-9}	Ref(3)
SUZAKU	bbody+diskbb+powerlaw	—	diskline	$6.83\ ^{+0.15}_{-0.06}$	132±12 eV	7.7±0.5	26±2	—	0.5-10 keV: 5.9±0.9)×10^{-9} [a]	Ref(4)
SUZAKU	bbody+diskbb+powerlaw	—	diskline	$6.97\ ^{+0.15}_{-0.02}$	98 eV	8.0±0.3	24±1	—	0.5-25 keV: (1.19±0.01)×10^{-8}	Ref(5)
SUZAKU	bbody+diskbb+powerlaw	reflionx	—	—	—	6±1	16±1	2.6±0.1	0.5-25 keV: (1.32±0.08)×10^{-8}	Ref(5)
XMM-Newton	bbody+diskbb+powerlaw	—	diskline	6.66 - 6.97	38 - 50 eV	14 - 26	13 - 32	—	0.5-25 keV: (0.6-0.7)×10^{-8}	Ref(5)
XMM-Newton	bbody+diskbb+powerlaw	reflionx	—	—	—	15 - 107	3 - 9	2.6 - 2.8	0.5-25 keV: (0.6-0.7)×10^{-8}	Ref(5)
NuSTAR	bbody+diskbb+powerlaw	—	kerrdisk	6.97±0.01	91±2 eV	10.6±0.6	18±2	—	(0.5-40 keV: 1.5×10^{-8}	Ref(6)
NuSTAR	bbody+diskbb+powerlaw	reflionx	—	—	—	6 - 8.3	¡10	2.30 - 2.60	—	Ref(6)
Chandra	bbody+diskbb+powerlaw	—	diskline	6.97±0.02	149±15 eV	7.7±0.1	24±1	—	—	Ref(7)
Chandra	bbody+diskbb+powerlaw	reflionx	—	—	—	$7.1^{+1.1}_{-0.6}$	29±1	$2.5^{+0.9}_{-0.6}$	—	Ref(7)
Chandra	bbody+diskbb+powerlaw	xillver	—	—	—	$8.4^{+1.1}_{-0.3}$	33±1	$2.2^{+0.7}_{-0.5}$	—	Ref(7)

[1]

[a] Estimated only for the continuum component

Table 4.2: Results of the fit of NuSTAR and XMM-Newton spectra of Ser X-1 using Gaussian and Diskline models

Component	Parameter	gauss	diskline	gauss-pl	diskline-pl	diskline-pl-xmm
phabs	N_H ($\times 10^{22}$ cm^{-2})	0.4 (f)	0.4 (f)	0.4 (f)	0.4 (f)	0.863±0.008
bbody	kT_{bb} (keV)	0.47±0.03	0.54±0.06	0.44±0.04	0.47±0.05	0.47±0.02
R_{BB}	(km)	46.1±6.3	34.3±7.7	45.5±9.5	39.2±8.7	35.1±3.2
bbody	Norm ($\times 10^{-3}$)	22.6±2.3	21.8±0.8	16.9 ±3.4	16.3±2.2	13.1±0.9
gaussian	E (keV)	6.57±0.05	—	6.56±0.05	—	
gaussian	Sigma (keV)	0.37±0.04	—	0.39±0.04	—	
gaussian	Norm ($\times 10^{-3}$)	4.03±0.35	—	4.48±0.34	—	
diskline	line E (keV)	—	6.54±0.04	—	6.54±0.03	6.48±0.06
diskline	Betor	—	-2.59±0.12	—	-2.54±0.13	-2.58±0.18
diskline	R_{in} (R_g)	—	18.6±4.9	—	19.2±4.7	$22.0^{+2.7}_{-5.2}$
diskline	R_{out} (R_g)	—	2400(f)	—	2400(f)	2400(f)
diskline	Incl (deg)	—	40.1±3.6	—	41.5±3.9	46.1±5.6
diskline	Norm ($\times 10^{-3}$)	—	4.38±0.47	—	4.54±0.35	2.89±0.28
nthComp	Gamma	2.41±0.04	2.43±0.04	2.26±0.04	2.27±0.04	$2.10^{+0.14}_{-0.06}$
nthComp	kT_e (keV)	2.95±0.05	2.98±0.04	2.75±0.05	2.76±0.05	2.27±0.16
nthComp	kT_{bb} (keV)	0.96±0.03	0.99±0.04	0.90±0.04	0.92±0.04	0.92±0.06 ; 0.82±0.05 ; 0.88±0.06
nthComp	Norm ($\times 10^{-3}$)	219±11	200±15	229±12	217±18	160±13
powerlaw	Index_pl	—	—	3.20(f)	3.20(f)	3.20(f)
powerlaw	Norm	—	—	0.84±0.12	0.82±0.13	0.72±0.04
gau-rgs	E (keV)	—	—	—	—	0.528 (f)
gau-rgs	Sigma ($\times 10^{-3}$ keV)	—	—	—	—	2.19 (f)
gau-rgs	Norm ($\times 10^{-3}$)	—	—	—	—	-18.4 (f)
gau-rgs	E (keV)	—	—	—	—	0.541 (f)
gau-rgs	Sigma ($\times 10^{-3}$ keV)	—	—	—	—	1.36 (f)
gau-rgs	Norm ($\times 10^{-3}$)	—	—	—	—	57.1 (f)
gau-rgs	E (keV)	—	—	—	—	0.714±0.02
gau-rgs	Sigma ($\times 10^{-3}$ keV)	—	—	—	—	5.8±0.6
gau-rgs	Norm ($\times 10^{-3}$)	—	—	—	—	-12.1±0.7
-	Eq.W (eV)	76±6	85±7	84±6	89±9	72±16 ; 93±18 ; 79±16
-	Obs. Flux	5.25±0.03	5.27±0.03	5.27±0.02	5.27±0.02	3.68±0.24
-	Luminosity	3.72±0.02	3.72±0.02	3.73±0.02	3.73±0.02	2.62±0.17
χ^2_{red} (d.o.f.)	-	1.2750(915)	1.2186(913)	1.14134(914)	1.0961(912)	1.3521(4546)

[2]

Table 4.3: Results of the fit of NuSTAR and XMM-Newton spectra of Ser X-1 using rdblur combined with rfxconv or reflionx

Component	Parameter	rdb-rfxconv	rdb-reflio	rdb-rfxconv-pl	rdb-reflio-pl	rdb-rfxconv-pl-xmm
phabs	N_H ($\times 10^{22}$ cm^{-2})	0.4 (f)	0.4 (f)	0.4 (f)	0.4 (f)	0.896±0.005
bbody	kT_{bb} (keV)	0.71±0.02	0.80±0.02	$0.54^{+0.05}_{-0.02}$	0.54±0.06	0.39±0.04
R_{BB}	(km)	23.6±1.3	15.9±0.8	24.7±7.9	19.2±4.6	49.4±10.6
bbody	Norm ($\times 10^{-3}$)	30.9±0.5	22.5 ±0.6	$11.3^{+3.3}_{-6.1}$	6.8 ±1.2	12.3 ±1.6
highecut	E_{cut} (keV)	—	0.1 (f)	—	0.1 (f)	—
highecut	E_{fold} (keV)	—	8.61±0.19	—	5.04±0.09	—
rdblur	Betor	-3.02±0.36	-2.49±0.15	-2.64±0.16	-2.53±0.14	$-2.46^{+0.56}_{-0.42}$
rdblur	R_{in} (R_g)	7.7±1.3	15.5±4.6	13.4±2.8	13.2±3.1	$14.2^{+9.5}_{-4.6}$
rdblur	R_{out} (R_g)	2400(f)	2400(f)	2400(f)	2400(f)	2400(f)
rdblur	Incl (deg)	29.2±1.8	32.2±1.7	27.1±1.9	28.8±2.4	27(f)
reflionx	Gamma	—	2.88±0.08	—	1.51±0.03	—
reflionx	ξ	—	4990^{+695}_{-2350}	—	490^{+21}_{-98}	—
reflionx	Norm ($\times 10^{-5}$)	—	1.97±0.59	—	10.7±3.5	—
rfxconv	rel_refl	0.55±0.04	—	0.24±0.04	—	0.183±0.022
rfxconv	cosIncl	0.88(f)	—	0.88(f)	—	0.891(f)
rfxconv	log(ξ)	2.68±0.05	—	$2.69^{+0.02}_{-0.11}$	—	3.04±0.11
nthComp	Gamma	3.55±0.18	2.88±0.08	2.17±0.04	1.51±0.03	2.45±0.22
nthComp	kT_e (keV)	$4.36^{+0.57}_{-0.23}$	3.19±0.08	2.70±0.04	5.05±0.09	$3.83^{+1.91}_{-1.02}$
nthComp	kT_{bb} (keV)	1.51±0.04	1.43±0.05	0.93±0.07	1.04±0.18	0.85±0.05 ; 0.76±0.06 ; 0.82±0.06
nthComp	Norm ($\times 10^{-3}$)	71.2±7.2	69.7±4.2	192±24	286^{+18}_{-22}	205±21
powerlaw	Index_pl	—	—	3.21±0.24	3.20(f)	3.98±0.31
powerlaw	Norm	—	—	$1.08^{+1.12}_{-0.72}$	0.82±0.13	0.68±0.05
-	Obs. Flux	5.26±0.15	5.27±0.17	5.27±0.62	5.27±0.55	4.12±0.38
-	Luminosity	3.73±0.11	3.74±0.12	3.74±0.44	3.74±0.39	2.93±0.27
χ^2_{red} (d.o.f.)	-	1.0983(913)	1.0838(913)	1.0017(911)	1.0123(912)	1.33762(4546)

[3]

star, we fitted the *NuSTAR* spectra using reflection components convolved with `kerrconv` instead of `rdblur`. Kerrconv convolves the spectrum with the smearing produced by a kerr disk model. It features the dimensionless 'a' parameter that characterize the spin of the system. We have performed our fit first leaving 'a' as a free parameter and then fixing it to the following three values, 0, 0.12, 0.14. The model with reflionx and 'a' treated as free parameter is called *ker-reflio-af*, whereas for $a = 0$, $a = 0.12$ and $a = 0.14$ the models are called *ker-reflio-a0*, *ker-reflio-a012*, and *ker-reflio-a014*, respectively. In the same way, the model with rfxconv and 'a' treated as free parameter is called *ker-rfxconv-af*, whereas for $a = 0$, $a = 0.12$ and $a = 0.14$ the models are called *ker-rfxconv-a0*, *ker-rfxconv-a012*, and *ker-rfxconv-a014*, respectively. All the models fit the data well; reduced χ^2 are between 1.08 and 1.18 and residuals are basically identical . Moreover the best-fit values of all parameters are very similar to the case with $a = 0$ and to the values we get using `rdblur` instead of `kerrconv`. The fit is therefore insensitive to the spin parameter, although there is a slight preference of the fit towards low values ($a < 0.04$). It is worth noting that in all best fit residuals a feature is present at about 3.9 keV that could be the resonance line of Ca XIX (3.9 keV). Moreover, again we observe high energy residuals (above 30 keV) indicating the presence of a hard power-law component. Also in this case, we get a very large ionization parameter using reflionx.

To avoid this problem, we therefore added a power-law component to the model obtained by the convolution of `kerrconv` with the two different reflection components (reflionx or rfxconv). we considered 'a' free to vary or fixed it to three different values (0, 0.12, 0.14). In all the cases the fits are quite good with values of the reduced χ^2 from 1.0 to 1.01. Again the addition of the power-law proved to be highly statistically significant. The F-test probability of chance improvement for the addition of two parameters is, for instance, 7.5×10^{-15} and 9×10^{-33} for the addition of a power-law to the model *ker-reflio-af* and *ker-rfxconv-af*, respectively. As before, the fit is quite insensitive to the value assumed by the spin parameter 'a'. Values of the best-fit parameters are listed in Tab 4.4 and 4.5.

Table 4.4: Results of the fit of the NuSTAR spectra using kerrconv combined with rfxconv or reflionx components

Component	Parameter	ker-reflio-af	ker-reflio-a0	ker-reflio-a012	ker-reflio-a014	ker-rfxconv-af	ker-rfxconv-a0	ker-rfxconv-a012	ker-rfxconv-a014
bbody	kT_{bb} (keV)	0.79±0.02	0.80±0.02	0.80±0.03	0.80±0.03	0.70±0.02	0.71±0.02	0.71±0.03	0.67±0.04
bbody	Norm ($\times 10^{-3}$)	22.4±0.3	22.5±0.4	22.5±0.7	22.4±0.8	30.1±0.11	31.2±0.3	30.8±0.2	29.9±0.5
highecut	E_{cut} (keV)	0.1 (f)	0.1 (f)	0.1 (f)	0.1 (f)	—	—	—	—
highecut	E_{fold} (keV)	8.54±0.06	8.56±0.13	8.52±0.29	8.59±0.21	—	—	—	—
kerrconv	Index	2.38±0.25	2.53±0.16	2.49±0.19	2.46±0.18	3.65±0.27	3.35±0.48	2.7±0.25	6.5±1.6
kerrconv	a	$0.019^{+0.019}_{-0.021}$	0.0 (f)	0.12 (f)	0.14(f)	0.036±0.008	0.0(f)	0.12(f)	0.14(f)
kerrconv	Incl (deg)	32.2±1.9	32.1±1.3	31.9±1.6	32.1±2.1	30.4±0.4	30.4±1.6	29.4±0.4	35.7±1.6
kerrconv	R_{in} (R_g)	14.5±1.8	18.1±5.7	16.3±5.4	15.7(f)	7.8±0.4	7.8±1.6	< 12.5	6.8±0.3
kerrconv	R_{out} (R_g)	2400(f)	2400(f)	2400(f)	2400(f)	2400(f)	2400(f)	2400(f)	2400(f)
reflionx	Gamma	2.85±0.05	2.86±0.05	2.85±0.12	2.87±0.08	—	—	—	—
reflionx	ξ	3722±61	3784^{+2050}_{-1100}	3580^{+2140}_{-1430}	4980^{+990}_{-2270}	—	—	—	—
reflionx	Norm ($\times 10^{-5}$)	2.38±0.55	2.36±0.95	2.47±1.25	$1.91^{+1.62}_{-0.58}$	—	—	—	—
rfxconv	rel_refl	—	—	—	—	0.58±0.06	0.58±0.03	0.54±0.02	0.69±0.03
rfxconv	cosIncl	—	—	—	—	0.88(f)	0.88(f)	0.88(f)	0.88(f)
rfxconv	log(ξ)	—	—	—	—	2.71±0.03	2.68±0.04	2.68±0.03	2.69±0.04
nthComp	Gamma	2.85±0.05	2.86±0.05	2.85±0.12	2.87±0.08	3.74±0.02	3.75±0.07	3.69±0.06	3.76±0.12
nthComp	kT_e (keV)	3.16±0.03	3.17±0.05	3.16±0.11	$3.19^{+0.09}_{-0.05}$	4.53±0.06	4.51±0.25	4.40±0.16	$4.62^{+0.35}_{-0.24}$
nthComp	kT_{bb} (keV)	1.42±0.03	1.43±0.02	1.43±0.03	1.43±0.04	1.53±0.03	1.53±0.03	1.52±0.05	1.55±0.03
nthComp	Norm ($\times 10^{-3}$)	70.9±1.9	70.3±3.5	$69.9^{+6.6}_{-2.2}$	$70.2^{+4.5}_{-3.3}$	$69.7^{+2.9}_{-12.2}$	$69.6^{+1.1}_{-5.5}$	$71.1^{+5.9}_{-3.3}$	$71.3^{+1.8}_{-5.2}$
-	R_{BB} (km)	14.9±0.9	14.5±0.8	14.6±1.1	14.5±1.5	21.1±1.3	21.8±1.2	21.6±1.7	21.9±2.9
χ^2_{red} (d.o.f.)	-	1.0876(912)	1.0876(913)	1.0859(913)	1.0835(914)	1.1797(914)	1.0981(913)	1.1111(913)	1.0849(913)

Table 4.5: Fitting results adding a power-law to the models of Table

Component	Parameter	ker-reflio-af-pl	ker-reflio-a0-pl	ker-reflio-a012-pl	ker-reflio-a014-pl	ker-rfxconv-af-pl	ker-rfxconv-a0-pl	ker-rfxconv-a012-pl	ker-rfxconv-a014-pl
bbody	kT_{bb} (keV)	0.54±0.18	0.52±0.12	0.56±0.08	0.53±0.13	0.55±0.03	0.59±0.08	0.55±0.03	0.50±0.07
bbody	Norm ($\times 10^{-3}$)	6.8±0.3	8.4±1.1	6.7±0.7	8.4±0.8	11.9±1.6	14.1±0.8	11.9±0.4	10.8±1.2
highecut	E_{cut} (keV)	0.1 (f)	0.1 (f)	0.1 (f)	0.1 (f)	—	—	—	—
highecut	E_{fold} (keV)	5.05±0.08	5.08±0.07	5.04±0.05	5.08±0.08	—	—	—	—
kerrconv	Index	2.59±0.14	2.51±0.12	2.54±0.08	2.51±0.19	2.72±0.27	2.78±0.12	2.71±0.13	2.66±0.18
kerrconv	a	< 0.019	0.0 (f)	0.12 (f)	0.14(f)	$0.06^{+0.67}_{-0.02}$	0.0(f)	0.12(f)	0.14(f)
kerrconv	Incl (deg)	28.3±1.7	28.4±0.9	28.3±0.5	28.3±1.4	26.0±0.9	26.1±0.9	26.1±0.8	26.1±0.8
kerrconv	R_{in} (R_g)	13.6±4.8	12.6±1.5	14.5±0.4	13.8±4.5	15.3±3.9	13.2±3.1	15.6±3.8	15.9±3.6
kerrconv	R_{out} (R_g)	2400(f)	2400(f)	2400(f)	2400(f)	2400(f)	2400(f)	2400(f)	2400(f)
reflionx	Gamma	1.51±0.04	1.52±0.03	1.50±0.04	1.52±0.04	—	—	—	—
reflionx	ξ	497^{+23}_{-81}	496±17	501±19	497^{+14}_{-79}	—	—	—	—
reflionx	Norm ($\times 10^{-5}$)	10.5±1.8	9.9±0.8	10.4±3.2	$9.9^{+2.8}_{-1.1}$	—	—	—	—
rfxconv	rel_refl	—	—	—	—	0.24±0.04	0.27±0.03	0.25±0.03	0.24±0.03
rfxconv	cosIncl	—	—	—	—	0.88(f)	0.88(f)	0.88(f)	0.88(f)
rfxconv	log(ξ)	—	—	—	—	2.71±0.03	2.69±0.04	2.71±0.05	2.69±0.05
nthComp	Gamma	1.51±0.04	1.52±0.03	1.50±0.04	1.52±0.04	2.19±0.04	2.24±0.05	2.19±0.05	2.15±0.04
nthComp	kT_e (keV)	5.04±0.08	5.08±0.07	5.04±0.05	5.08±0.08	2.71±0.05	2.76±0.08	$2.71^{+0.02}_{-0.06}$	$2.68^{+0.07}_{-0.03}$
nthComp	kT_{bb} (keV)	1.04±0.22	1.05±0.06	1.04±0.04	1.04±0.14	0.94±0.07	1.01±0.16	0.94±0.05	0.90±0.09
nthComp	Norm ($\times 10^{-3}$)	287±19	289±77	501±15	289±38	187^{+5}_{-11}	161^{+46}_{-5}	187^{+9}_{-18}	210^{+7}_{-38}
powerlaw	Index_pl	$3.20^{+0.33}_{-1.02}$	3.20(f)	3.20(f)	$3.09^{+0.57}_{-1.02}$	3.20(f)	3.20(f)	3.20(f)	3.20(f)
powerlaw	Norm	0.81±0.42	0.82±0.12	0.80±0.08	$0.54^{+2.13}_{-0.34}$	1.04±0.09	0.98±0.08	1.04±0.13	1.06±0.11
-	R_{BB} (km)	17.6±10.8	20.9±8.9	16.2±5.3	20.3±8.9	22.4±2.9	21.2±5.1	22.4±2.4	25.8±7.4
χ^2_{red} (d.o.f.)	-	1.0148(910) f	1.0123(912)	1.0083(912)	1.0138(911)	1.0016(911)	1.0023(912)	1.0008(912)	1.0006(912)

[5]

Chapter 5

An *XMM-Newton* and *INTEGRAL* view on the hard state of EXO 1745–248 during its 2015 outburst

5.1 Abstract

Context - Transient low-mass X-ray binaries (LMXBs) often show outbursts lasting typically a few-weeks and characterized by a high X-ray luminosity ($L_x \approx 10^{36} - 10^{38}$ erg s^{-1}), while for most of the time they are found in X-ray quiescence ($L_X \approx 10^{31} - 10^{33}$ erg s^{-1}). EXO 1745–248 is one of them.

Aims - The broad-band coverage, and the sensitivity of instruments on board *XMM-Newton* and *INTEGRAL*, offers the opportunity to characterize the hard X-ray spectrum during EXO 1745–248 outburst.

Methods - In this chapter we report on quasi-simultaneous *XMM-Newton* and *INTEGRAL* observations of the X-ray transient EXO 1745–248 located in the globular cluster Terzan 5, performed ten days after the beginning of the outburst shown by the source between March and June 2015. The source was caught in a hard state, emitting a 0.8-100 keV luminosity of $\simeq 10^{37}$ erg s^{-1}.

Results - The spectral continuum was dominated by thermal Comptonization of seed photons with temperature $kT_{in} \simeq 1.3$ keV, by a cloud with moderate optical depth $\tau \simeq 2$ and electron temperature $kT_e \simeq 40$ keV. A weaker soft thermal component at temperature $kT_{th} \simeq 0.6$–0.7 keV and compatible with a fraction of the neutron star radius was also detected. A rich emission line spectrum was observed by the EPIC-pn on-board *XMM-Newton*; features at energies

compatible with K-α transitions of ionized sulfur, argon, calcium and iron were detected, with a broadness compatible with either thermal Compton broadening or Doppler broadening in the inner parts of an accretion disk truncated at 20 ± 6 gravitational radii from the neutron star. Strikingly, at least one narrow emission line ascribed to neutral or mildly ionized iron is needed to model the prominent emission complex detected between 5.5 and 7.5 keV. The different ionization state and broadness suggest an origin in a region located farther from the neutron star than where the other emission lines are produced. Seven consecutive type-I bursts were detected during the *XMM-Newton* observation, none of which showed hints of photospheric radius expansion. A thorough search for coherent pulsations from the EPIC-pn light curve did not result in any significant detection. Upper limits ranging from a few to 15% on the signal amplitude were set, depending on the unknown spin and orbital parameters of the system.

5.2 Introduction

Globular clusters are ideal sites for the formation of binary systems hosting a compact object thanks to the frequent dynamical interaction caused by their dense environment (Meylan and Heggie, 1997). Low mass X-ray binaries (LMXB) formed by a neutron star (NS) that accretes matter lost by a companion, low mass star are particularly favored, as stellar encounters may cause the lower mass star of a binary to be replaced by an heavier NS (Verbunt and Hut, 1987). Some of the densest and most massive globular clusters have the highest predicted rates of stellar interactions and host a numerous population of LMXBs (Heinke et al., 2003b).

Terzan 5 is a compact, massive cluster at a distance of 5.5 kpc which hosts at least three stellar populations with different iron abundances; the observed chemical pattern suggests that it was much more massive in the past, so to be able to hold the iron rich ejecta of past supernova explosions (Ferraro et al., 2009; Origlia et al., 2013), and (ApJ in press Ferraro et al., 2016). Terzan 5 has the highest stellar interaction rate than any cluster in the Galaxy (Verbunt and Hut, 1987). This reflects into the largest population known of millisecond radio pulsars (34; Ransom et al., 2005; Hessels et al., 2006), and in at least 50 X-ray sources, including a dozen likely quiescent LMXBs (Heinke et al., 2006). The populations of millisecond radio pulsars and LMXBs are linked from an evolutionary point of view, as mass accretion in a LMXB is expected to speed up the rotation of a NS down to a spin period of a few milliseconds (Alpar et al., 1982). This link was

confirmed by the discovery of accreting millisecond pulsars (AMSPs; Wijnands and van der Klis, 1998), and by the observations of binary millisecond pulsars swinging between a radio pulsar and an accretion disk state on time scales that can be as short as weeks (Archibald et al., 2009; Papitto et al., 2013a; Bassa et al., 2014). Globular clusters like Terzan 5 are preferential laboratories to study the relation between these two classes of sources.

Many LMXBs are X-ray transients; they show outbursts lasting typically a few-weeks and characterized by a high X-ray luminosity ($L_x \approx 10^{36}-10^{38}$ erg s^{-1}), while for most of the time they are found in X-ray quiescence ($L_X \approx 10^{31} - 10^{33}$ erg s^{-1}). X-ray transient activity has been frequently observed from Terzan 5 since 1980s (Makishima et al., 1981; Warwick et al., 1988; Verbunt et al., 1995) and ten outbursts have been detected ever since (see, e.g., Table 1 in Degenaar and Wijnands, 2012). The large number of possible counterparts in the cluster complicates the identification of the transient responsible for each event when a high spatial resolution X-ray (or radio) observation was not available. As a consequence, only three X-ray transients of Terzan 5 have been securely identified, EXO 1745–248 (Terzan 5 X–1, active in 2000, 2011 and 2015 Makishima et al., 1981; Markwardt and Swank, 2000; Heinke et al., 2003a; Serino et al., 2012a; Tetarenko et al., 2016), IGR J17480–2446 (Terzan 5 X–2, active in 2010; Papitto et al., 2011; Motta et al., 2011) and Swift J174805.3–244637 (Terzan 5 X–3, active in 2012; Bahramian et al., 2014).

The first confirmed outburst observed from EXO 1745–248 took place in 2000, when a *Chandra* observation could pin down the location of the X-ray transient with a sub-arcsecond accuracy (Heinke et al., 2003a). The outburst lasted $\sim$ 100 d, showing a peak of luminosity[1] $\sim 6\times10^{37}$ erg s^{-1} (Degenaar and Wijnands, 2012). The X-ray spectrum was dominated by thermal Comptonization in a cloud with a temperature ranging between a few and tens of keV (Heinke et al., 2003a; Kuulkers et al., 2003); a thermal component at energies of $\approx$ 1 keV, and a strong emission line at energies compatible with the Fe K-α transition were also present in the spectrum. More than 20 type-I X-ray bursts were observed, in none of which burst oscillations could be detected (Galloway et al., 2008). Two of these bursts showed evidence of photospheric radius expansion, and were considered by Özel et al. (2009) to draw constraints on the mass and radius of the NS. A second outburst was observed from EXO 1745–248 in 2011, following the detection of a

[1]Throughout this thesis we evaluate luminosities and radii for a distance of 5.5 kpc, which was estimated by Ortolani et al. (2007) with an uncertainty of 0.9 kpc. There is also an determination from Valenti et al. (2007) for the distance (5.9kpc) consistent within errors with Ortolani's distance.

superburst characterized by a decay timescale of ≈ 10 hr (Altamirano et al., 2012; Serino et al., 2012b). The outburst lasted ≈ 20 d, reaching an X-ray luminosity of 9×10^{36} erg s^{-1}. Degenaar and Wijnands (2012) found a strong variability of the X-ray emission observed during quiescence between the 2000 and the 2011 outburst, possibly caused by low-level residual accretion.

A new outburst from Terzan 5 was detected on 2015 March, 13 (Altamirano et al., 2015). It was associated to EXO 1745–248 based on the coincidence between its position (Heinke et al., 2006) and the location of the X-ray source observed by Swift XRT (Linares et al., 2015) and of the radio counterpart detected by the Karl G. Jansky Very Large Array (VLA; Tremou et al., 2015), with an accuracy of 2.2 and 0.4 arcsec, respectively. The outburst lasted ≈ 100 d and attained a peak X-ray luminosity of 10^{38} erg s^{-1}, roughly a month into the outburst (Tetarenko et al., 2016). The source performed a transition from a hard state (characterized by an X-ray spectrum described by a power law with photon index ranging from 0.9 to 1.3) to a soft state (in which the spectrum was thermal with temperature of ≈ 2–3 keV) a few days before reaching the peak flux (Yan et al., 2015). The source transitioned back to the hard state close to the end of the outburst. Tetarenko et al. (2016) showed that throughout the outburst the radio and X-ray luminosity correlated as $L_R \propto L_X^{\beta}$ with $\beta = 1.68^{+0.10}_{-0.09}$, indicating a link between the compact jet traced by the radio emission and the accretion flow traced by the X-ray output. The optical counterpart was identified by Ferraro et al. (2015), who detected the optical brightening associated to the outburst onset in *Hubble Space Telescope* images; the location of the companion star in the color-magnitude diagram of Terzan 5 is consistent with the main sequence turn-off. We stress that the HST study suggests that EXO 1745–248 is in an early phase of accretion stage with the donor expanding and filling its roche lobe thus representing a prenatal stage of a millisec pulsar binary. This would make more interesting the study of this source as well as linking what we stated above regarding MSP and AXP binaries

Here we present an analysis of the X-ray properties of EXO 1745–248, based on an *XMM-Newton* observation performed ≈ 10 days into the 2015 outburst, when the source was in the hard state.

The main goal of this observation is to observe at a better statistics the region of spectrum around the iron line. Then adding the broad-band coverage allowed by *INTEGRAL* observations, we are able to study the possible associated reflection features and give a definite answer on the origin of the iron line. We also make use of additional monitoring observations of the source carried out with

INTEGRAL during its 2015 outburst to spectroscopically confirm the hard-to-soft spectral state transition displayed by EXO 1745-248 around 57131 MJD (as previously reported by Tetarenko et al., 2016). We stress out that this transition was observed by *Swift*. In order to understand the physical properties of this state, we perfomed an observation with *XMM-Newton* allowing more sensitive and higher resolution data. We focus in Sec. 5.4 on the shape of the X-ray spectrum and in Sec. 5.5 on the properties of the temporal variability, while an analysis of the X-ray bursts observed during the considered observations is presented in Sec. 5.6.

5.3 Observations and Data Reduction

5.3.1 XMM-Newton

XMM-Newton observed EXO 1745–248 for 80.8 ks starting on 2015, March 22 at 04:52 (UTC; ObsId 0744170201). Data were reduced using the SAS (Science Analysis Software) v.14.0.0.

The EPIC-pn camera observed the source in timing mode to achieve a high temporal resolution of 29.5 μs and to limit the effects of pile-up distortion of the spectral response during observations of relatively bright Galactic X-ray sources. A thin optical blocking filter was used. In timing mode the imaging capabilities along one of the axis are lost to allow a faster readout. The maximum number of counts fell on the RAWX coordinates 36 and 37. To extract the source photons we then considered a 21 pixel-wide strip extending from RAWX=26 to 46. Background photons were instead extracted in the region ranging from RAWX=2 to RAWX=6. Single and double events were retained. Seven type-I X-ray bursts took place during the *XMM-Newton* observation with a typical rise time of less than 5 s and a decay e-folding time scale ranging from 10 to 23 s. In order to analyze the *persistent* (i.e. non-bursting) emission of EXO 1745–248 we identified the start time of each burst as the first 1 s-long bin that exceeded the average count-rate by more than 100 s^{-1}, and removed from the analysis a time interval spanning from 15 s before and 200 s after the burst onset. After the removal of the burst emission, the mean count rate observed by the EPIC-pn was 98.1 s^{-1}. Pile-up was not expected to affect significantly the spectral response of the EPIC-pn at the observed *persistent* count rate (Guainazzi et al. 2014; Smith et al. 2016)[2]. To check the absence of strong distortion we run the

[2]http://xmm2.esac.esa.int/docs/documents/CAL-TN-0083.pdf,

SAS task *epatplot*, and obtained that the fraction of single and double pattern events falling in the 2.4–10 keV band were compatible with the expected value within the uncertainties. Therefore, no pile-up correction method was employed. The spectrum was re-binned so to have not more than three bins per spectral resolution element, and at least 25 counts per channel.

The MOS-1 and MOS-2 cameras were operated in Large Window and Timing mode, respectively. At the count rate observed from EXO 1745–248 both cameras suffered from pile up at a fraction exceeding 10% and were therefore discarded for further analysis.

We also considered data observed by the Reflection Grating Spectrometer (RGS), which operated in Standard Spectroscopy mode. We considered photons falling in the first order of diffraction. The same time filters of the EPIC-pn data analysis were applied.

5.3.2 INTEGRAL

We analyzed all *INTEGRAL* (Winkler et al., 2003a) available data collected in the direction of EXO 1745–248 during the source outburst in 2015. These observations included both publicly available data and our proprietary data in AO12 cycle.

The reduction of the *INTEGRAL* data was performed using the standard Offline Science Analysis (OSA) version 10.2 distributed by the ISDC (Courvoisier et al., 2003). *INTEGRAL* data are divided into science windows (SCW), i.e. different pointings lasting each $\sim 2-3$ ks. We analyzed data from the IBIS/ISGRI (Ubertini et al., 2003; Lebrun et al., 2003), covering the energy range 20-300 keV energy band, and from the two JEM-X monitors (Lund et al., 2003), operating in the range 3-20 keV. As the source position varied with respect to the aim point of the satellite during the observational period ranging from 2015 March 12 at 19:07 (satellite revolution 1517) to 2015 April 28 at 11:40 UTC (satellite revolution 1535), the coverage provided by IBIS/ISGRI was generally much larger than that of the two JEM-X monitors due to their smaller field of view.

As the source was relatively bright during the outburst, we extracted a lightcurve with the resolution of 1 SCW for both IBIS/ISGRI and the two JEM-X units. This is shown in Fig. 5.1, together with the monitoring observations provided by Swift/XRT (0.5-10 keV). The latter data were retrieved from the Leicester University on-line analysis tool (Evans et al., 2009) and used only to compare the monitoring provided by the Swift and *INTEGRAL* satellites. We refer the

http://xmm2.esac.esa.int/docs/documents/CAL-TN-0018.pdf

reader to Tetarenko et al. (2016) for more details on the Swift data and the corresponding analysis. In agreement with the results discussed by these authors, also the *INTEGRAL* data show that the source underwent a hard-to-soft spectral state transition around 57131 MJD. In order to prove this spectral state change more quantitatively, we extracted two sets of *INTEGRAL* spectra accumulating all data before and after this date for ISGRI, JEM-X1, and JEM-X2.

Analysis of broad-band *INTEGRAL* spectrua for both hard and soft state is reported in Sect. 5.4.1

We also extracted the ISGRI and JEM-X data by using only the observations carried out during the satellite revolution 1521, as the latter partly overlapped with the time of the *XMM-Newton* observation. The broad-band fit of the combined quasi-simultaneous *XMM-Newton* and *INTEGRAL* spectrum of the source is discussed in previous sections.

We removed from the data used to extract all JEM-X and ISGRI spectra mentioned above the SCWs corresponding to the thermonuclear bursts detected by *INTEGRAL*. These were searched for by using the JEM-X lightcurves collected with 2 s resolution in the 3-20 keV energy band. A total of 4 bursts were clearly detected by JEM-X in the SCW 76 of revolution 1517 and in the SCWs 78, 84, 94 of revolution 1521. The onset times of these bursts were 57094.24535 MJD, 57104.86423 MJD, 57104.99993 MJD, and 57105.25787 MJD, respectively. None of these bursts were significantly detected by ISGRI or showed evidence for a photospheric radius expansion. Given the limited statistics of the two JEM-X monitors during the bursts we did not perform any refined analysis of these events.

5.4 Spectral Analysis

Spectral analysis has been performed using XSPEC v.12.8.1 (Arnaud, 1996). For each fit we have used photoelectric cross sections and element abundances from Wilms et al. (2000b). The uncertainties on the parameters quoted in the following are evaluated at a 90% confidence level.

5.4.1 Hard and soft INTEGRAL spectra

The broad-band *INTEGRAL* spectrum of the source could be well described by using a simple absorbed power-law model with a cut-off at the higher energies (we fixed in all fits the absorption column density to the value measured by *XMM-Newton*, i.e. $N_{\rm H}$=2.02×10^{22} cm^{-2}). In the hard state ($\chi^2_{\rm red}/d.o.f. = 1.2/21$), we

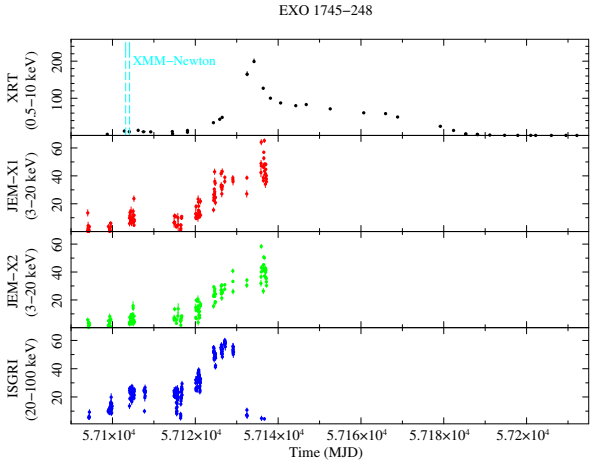

Figure 5.1: Lightcurve of the 2015 outburst displayed by EXO 1745–248 as observed by IBIS/ISGRI and JEM-X on-board *INTEGRAL*. For completeness, we report also the lightcurve obtained from Swift/XRT and published previously by Tetarenko et al. (2016). The hard-to-soft spectral state transition of EXO 1745–248 around 57131 MJD discussed by Tetarenko et al. (2016) is well visible in the above plots (around this date the count-rate of the source in the IBIS/ISGRI decreases significantly, while it countinues to raise in JEM-X). We marked with a vertical dashed line the time of the *XMM-Newton* observation, carried out during the hard state of the source, that we also analyzed in this chapter.

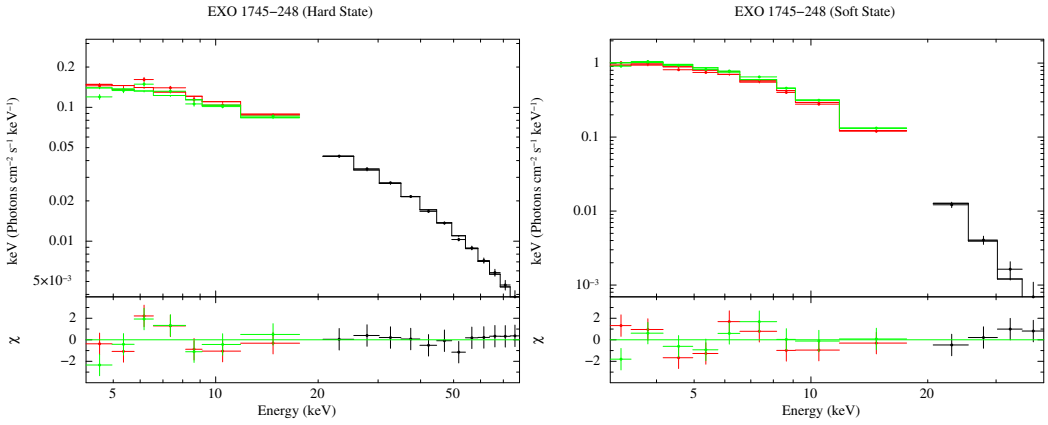

Figure 5.2: The broad-band spectrum of EXO 1745–248 as observed by *INTEGRAL* in the hard (left) and soft (right) state (ISGRI data are in black, JEM-X1 data in red, and JEM-X2 data in green). For both states the best fit to the spectrum was obtained with an absorbed cut-off power-law model (see text for details). The residuals from the best fits are shown in the bottom panels of the upper and lower figure.

measured a power-law photon index Γ=1.1±0.1 and a cut-off energy of 23±2 keV. The source X-ray flux was (2.9±0.2)×10^{-9} erg cm^{-2} s^{-1} in the 3-20 keV energy band, (1.0±0.1)×10^{-9} erg cm^{-2} s^{-1} in the 20-40 keV energy band, and (6.1±0.3)×10^{-10} erg cm^{-2} s^{-1} in the 40-100 keV energy band. The effective exposure time was of 123 ks for ISGRI and 75 ks for the two JEM-X units. In the soft state ($\chi^2_{\rm red}/d.o.f. = 1.3/17$), we measured a power-law photon index Γ=0.6±0.2 and a cut-off energy of 3.8±0.5 keV. The source X-ray flux was (9.5±0.5)×10^{-9} erg cm^{-2} s^{-1} in the 3-20 keV energy band, (1.6±0.3)×10^{-10} erg cm^{-2} s^{-1} in the 20-40 keV energy band, and (1.1±0.5)×10^{-12} erg cm^{-2} s^{-1} in the 40-100 keV energy band. The effective exposure time was of 32 ks for ISGRI and 20 ks for the two JEM-X units. The two broad-band spectra and the residuals from the best fits are shown in Fig. 5.2.

5.4.2 The 2.4–10 keV EPIC-pn spectrum

We first considered the spectrum observed by the EPIC-pn at energies between 2.4 and 10 keV (see top panel of Fig. 5.3), as a soft-excess probably related to uncertainties in the redistribution calibration affected data taken at lower energies (see the discussion in Guainazzi et al. 2015[3], and references therein). Interstellar absorption was described by the TBAbs component (Wilms et al., 2000b) the photoelectric cross sections from Verner et al. (1996) with the hydrogen column density fixed to $N_H = 2 \times 10^{22}$ cm^{-2}, as indicated by the analysis performed with the inclusion of RGS, low energy data (see Sec. 5.4.3). The spectral continuum was dominated by a hard, power-law like component with spectral index $\Gamma \simeq 2$, which we modeled as thermal Comptonization of soft photons with $kT_{in} \simeq 1.3$ keV, by using the model NTHCOMP (Zdziarski et al., 1996; Życki et al., 1999b). As the electron temperature fell beyond the energy range covered by the EPIC-pn, we fixed such parameter to 37 keV, as suggested by the analysis of data taken by INTEGRAL at higher energies (see Sec. 5.4.3). We modeled the strong residuals left by the Comptonization model at low energies with a black-body with effective temperature $kT_{th} \simeq 0.6$ keV and emission radius $R_{th} \simeq 5.5\, d_{5.5}$ km, where $d_{5.5}$ is the distance to the source in units of 5.5 kpc. The addition of such a component was highly significant as it decreased the model reduced chi-squared from 47.9 to 26.5 for the two degrees of freedom less, out of 122.

Even after the addition of a thermal component, the quality of the spectral fit was still very poor mainly because of residuals observed at energies of the Fe K-α transition (6.4–7 keV; see middle panel of Fig. 5.3). The shape of this emission

[3]http://xmm2.esac.esa.int/docs/documents/CAL-TN-0083.pdf

complex is highly structured and one emission line was not sufficient to provide an acceptable modeling. We then modeled the iron complex using three Gaussian features centered at energies $E_1 \simeq 6.75^{+0.02}_{-0.03}$, $E_2 \simeq 6.48^{+0.03}_{-0.01}$ and $E_3 \simeq 7.12^{+0.04}_{-0.07}$ keV. These energies are compatible with K-α transition of ionized Fe XXV, K-α and K-β of neutral or weakly ionized Fe (I-XX), respectively. The ionized iron line is relatively broad ($\sigma_1 = 0.24 \pm 0.03$ keV) and strong (equivalent width $EW_1 = 62.0 \pm 0.02$ eV), while the others are weaker and have a width lower than the spectral resolution of the instrument. In order to avoid correlation among the fitting parameters, we fixed the normalization of the K-β transition of weakly ionized iron to one tenth of the K-α. The addition of the three Fe emission lines decreased the model χ^2 to 266 for 114 degrees of freedom. Three more emission lines were required at lower energies, $E_4 = 2.74^{+0.01}_{-0.03}$, $E_5 = 3.30(3)$ and $E_6 = 3.94^{+0.05}_{-0.06}$ keV, compatible with K-α transitions of S XVI, Ar XVIII, and Ca XX (or XIX), respectively. The significance of these lines has been evaluated with an F-test, giving probabilities of 3×10^{-4}, 9×10^{-6} and 7.7×10^{-8}, respectively, that the improvement of the fit χ^2 obtained after the addition of the line is due to chance. The chi-squared of the model (dubbed Model I in Table 5.1) is $\chi^2 = 154.5$ for 106 degrees of freedom.

The broadness of the 6.75 keV Fe XXV line suggests reflection of hard X-rays off the inner parts of the accretion disk as a plausible origin. We then replaced the Gaussian profile with a relativistic broadened DISKLINE profile (Fabian et al., 1989). The three emission lines found between 2.4 and 4 keV have high ionization states and probably originate from the same region. We then modeled them with relativistic broadened emission features as well, keeping the disk emissivity index, β_{irr}, and the geometrical disk parameters (the inner and outer disk radii, R_{in} and R_{out}, and inclination, i) tied to the values obtained for the Fe XXV line. As the spectral fit was insensitive to the outer disc radius parameter, we left it frozen to its maximum value allowed (10^7 R_g, where $R_g = GM/c^2$ is the NS gravitational radius). Modeling of the neutral (or weakly ionized) narrow Fe lines at $\simeq 6.5$ and 7.1 keV with a Gaussian profile was maintained. We found that the energy of the lines were all consistent within the uncertainties with those previously determined with Model I. The parameters of the relativistic lines indicate a disk extending down to $R_{in} = 20^{+4}_{-6}$ R_g with an inclination of $i = (37 \pm 2)^\circ$ and an emissivity index of $\beta = -2.44^{+0.04}_{-0.06}$ (see column dubbed Model II of Tab. 5.1 for the whole list of parameters). Modeling of the spectrum with these broad emission lines decreased the fit χ^2 to 141.8, for 106 degrees of freedom, which translates into a probability of $p_{null} = 10^{-2}$ of obtaining a value of the fit χ^2 as large or larger if

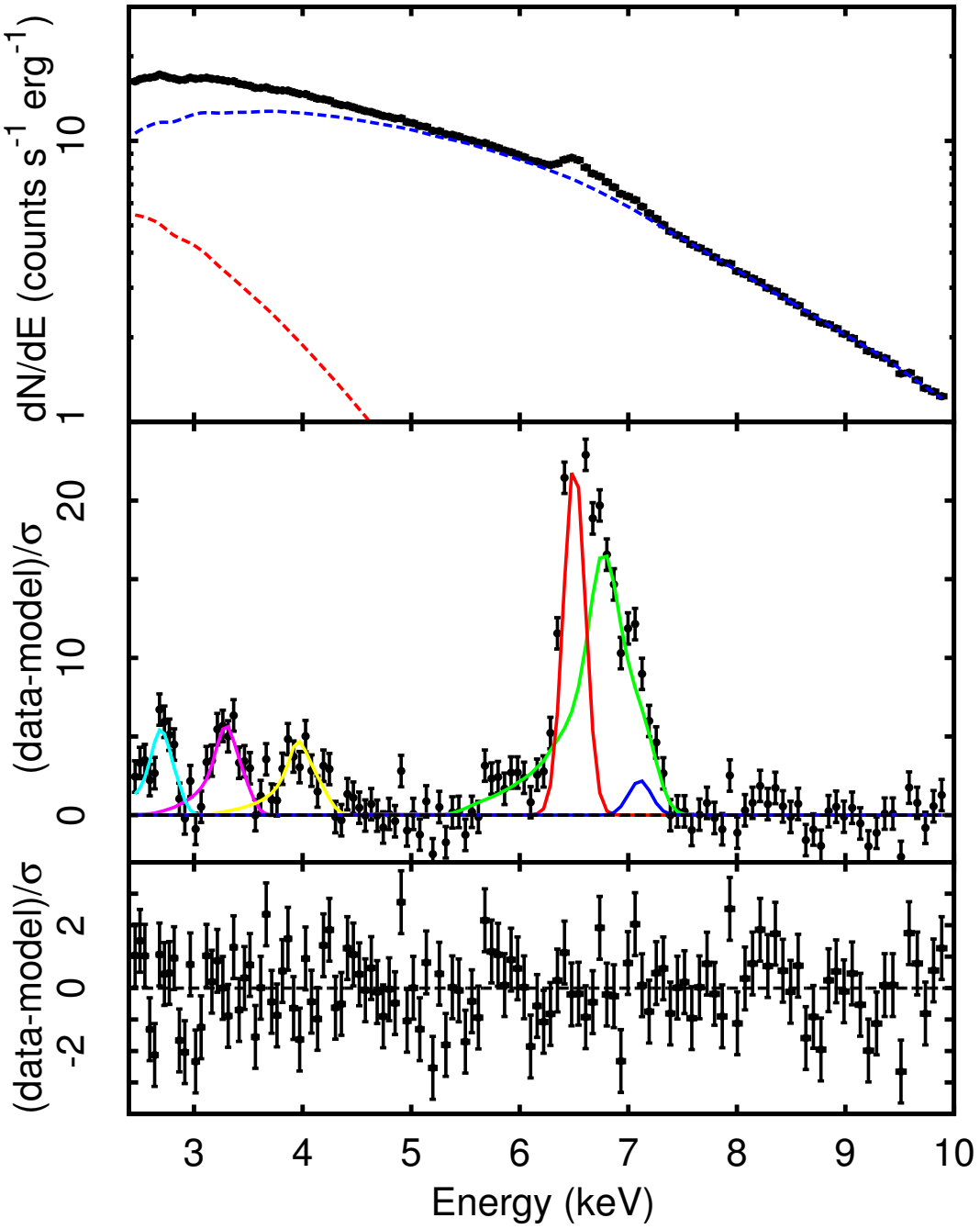

Figure 5.3: Spectrum observed by the EPIC-pn between 2.4 and 10 keV together with the best fitting black body (red dashed line) and Comptonization (blue dashed line) component of Model II listed in Table 5.1 (top panel). Residuals obtained when the six emission features at energies $E_1 = 6.75$ (green solid line), $E_2 = 6.48$ (red solid line), $E_3 = 7.12$ (blue solid line), $E_4 = 2.74$ (cyan), $E_5 = 3.30$ (magenta), $E_6 = 3.94$ (yellow) are removed from Model II (middle panel). The model is not fitted after the line removal, so the residuals are plotted for an illustrative purpose, only. Residuals left by Model II are plotted in the bottom panel.

the data are drawn from such a spectral model. Figure 5.3 shows the observed spectrum, the residuals with and without the inclusion of the emission lines. The model parameters are listed in the third column of Table 5.1.

5.4.3 The 0.35–180 keV XMM-Newton/INTEGRAL broadband spectrum

In order to study the broadband spectrum of EXO 1745–248 we fitted simultaneously the spectra observed by the two RGS cameras (0.35–2.0 keV) and the EPIC-pn (2.4–10 keV) on-board *XMM-Newton*, together with the spectra observed by the two JEM-X cameras (5–25 keV) and ISGRI (20-180 keV) on board *INTEGRAL* during the satellite revolution 1521, which partly overlapped with the *XMM-Newton* pointing. We initially considered Model II, in which the continuum was modeled by the sum of a Comptonized and a thermal component, the lines with energies compatible with ionized species were described by a relativistic broadened disk emission lines, and the K-α and K-β lines of neutral (or weakly) ionized iron were modeled by a Gaussian profile. The inclusion of the RGS spectra at low energies yielded a measure of the equivalent hydrogen column density $N_H = (2.02 \pm 0.04) \times 10^{22}$ cm^{-2}. At the high energy end of the spectrum, the ISGRI spectrum constrained the electron temperature of the Comptonizing electron population to $kT_e = 37^{+7}_{-5}$ keV. The other parameters describing the continuum and the lines were found to be compatible with those obtained from the modeling of the EPIC-pn spectra alone. The model parameters are listed in the fourth column of Table 5.1, dubbed Model II*.

In order to entertain the hypothesis that the broad emission lines are due to reflection of the primary Comptonized spectrum onto the inner accretion disk, we replaced the Fe XXV broad emission line described as DISKLINES in Model II* with a self-consistent model describing the reflection off an ionized accretion disk. We convolved the Comptonized component describing the main source of hard photons, NTHCOMP, with the disk reflection model RFXCONV (Kolehmainen et al., 2011b).

We further convolved the RFXCONV component with a relativistic kernel (RDBLUR) to take into account relativistic distortion of the reflection component due to a rotating disc. Because the RFXCONV model does not include Ar and Ca transitions and does not give a good modeling of the S line, leaving clear residuals at ~ 2.7 keV we included three DISKLINE components for them, linking the parameters of the RDBLUR component to the corresponding smearing parameters of the DISKLINES , according to the hypothesis that all these lines originate

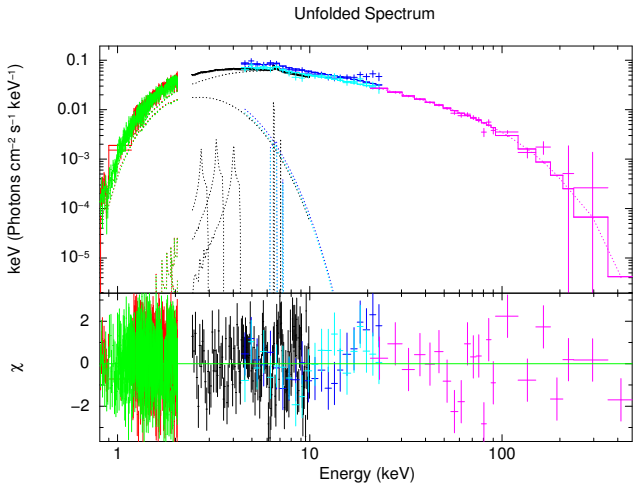

Figure 5.4: RGS1 (red), RGS2 (green), EPIC-pn (black), JEMX1 (blue), JEMX2 (cyan) and ISGRI (magenta) spectra (top panel). Residuals with respect to Model III are plotted in the bottom panel.

from the same disk region (see, e.g. di Salvo et al., 2009; Egron et al., 2013b; Di Salvo et al., 2015b). The best fit with this model (dubbed Model III, see fourth column of Table 5.1) was slightly worse (χ^2 /dof =1271/1083) than for Model II* (χ^2 /dof =1248/1083). According to the reflection model, the solid angle ($\Omega_r/2\pi$) subtended by the reflector as seen from the illuminating source was 0.22± 0.04. The logarithm of the ionization parameter of the disc was $\simeq$ 2.7, which could well explain the ionization state of the Fe XXV, S XVI, Ar XVIII and Ca XX (or XIX) emission lines observed in the spectrum. The inclination angle of the system was found to be consistent with 37°. The broadband continuum and the line parameters were not significantly changed by the introduction of the reflection model. The six instruments spectrum, the Model III and residuals are plotted in Fig. 5.4.

To test independently the significance of the Compton hump and absorption edges, constituting the continuum of the reflection component, we also tried a different reflection model, namely `pexriv` (Magdziarz and Zdziarski, 1995), which describes an exponentially cut off power law spectrum reflected from ionized material. We fixed the disk temperature to the default value 10^6 K, and the value on reflection fraction to 0.22, that is the best value found in Model III. We also tied parameters describing the irradiating power-law (photon index and energy cut-off) to those indicated by the `nthComp` component. As the iron emission is not included in the `pexriv` model, we added a `diskline` centered at 6.75 keV. The results of the fit are reported in the rightmost column of Table 5.1, labeled 'Model IV'. The parameters describing the irradiating continuum and the

reflection component are compatible with those obtained with RFXCONV, and the fit χ^2 slightly improved with respect to Model III ($\Delta\chi^2 = 28.6$ for two degrees of freedom less), while is compatible with the results obtained with Model II*.

5.5 Temporal analysis

The *persistent* (i.e, non-bursting) emission observed during the XMM-Newton EPIC-pn observation was highly variable, with a sample fractional rms amplitude of 0.33. A portion of the *persistent* light curve is shown in Fig. 5.5 for illustrative purposes. To study the power spectrum of the aperiodic variability we performed a fast Fourier transform of 32-s long intervals of the 0.5–10 keV EPIC-pn time series with 59 μs time resolution (corresponding to a Nyquist maximum frequency of 8468 Hz). We averaged the spectra obtained in the various intervals, re-binning the resulting spectrum as a geometrical series with a ratio of 1.04. The Leahy normalized and white noise subtracted average power spectrum is plotted in Fig. 5.6. The spectrum is dominated by a flicker noise component described by a power law, $P(\nu) \propto \nu^{-\alpha}$, with $\alpha = 1.05(1)$, slightly flattening towards low frequencies. In order to search for kHz quasi periodic oscillations already observed from the source at a frequency ranging from 690 to 715 Hz (Mukherjee and Bhattacharyya, 2011; Barret, 2012), we produced a power density spectrum over 4 s-long intervals to have a frequency resolution of 0.25 Hz, and averaged the spectra extracted every 40 consecutive intervals. No oscillation was found within a 3-σ confidence level upper limit of 1.5% on the rms variation.

In order to search for a coherent signal in the light curve obtained by the EPIC-pn, we first reported the observed photons to the Solar system barycenter, using the position RA=17^h 48^m 05.236, DEC=-24° 46' 47.38" reported by Heinke et al. (2006) with an uncertainty of 0.02" at 1-σ confidence level. We performed a power density spectrum on the whole $t_{pds} = 77.5$ ks exposure, re-binning the time series to a resolution equal to eight times the minimum ($t_{res} = 2.3 \times 10^{-4}$ s, giving a maximum frequency of $\nu_{Ny} = 2117$ Hz). After taking into account the number of frequencies searched, $N_f \simeq \nu_{Ny}\, t_{pds} = 1.64 \times 10^8$, we could not find any significant signal with an upper limit at 3-σ confidence level of 0.5% on the amplitude of a sinusoidal signal, evaluated following Vaughan et al. (1994).

The orbital period of EXO 1745–248 is currently unknown. On the spectral properties, Heinke et al. (2006) suggested it might be hosted in an ultra-compact binary ($P_{orb} << 1$ d). Based on empirical relation between the V magnitude of the optical counterpart, the X-ray luminosity and the orbital period, Ferraro

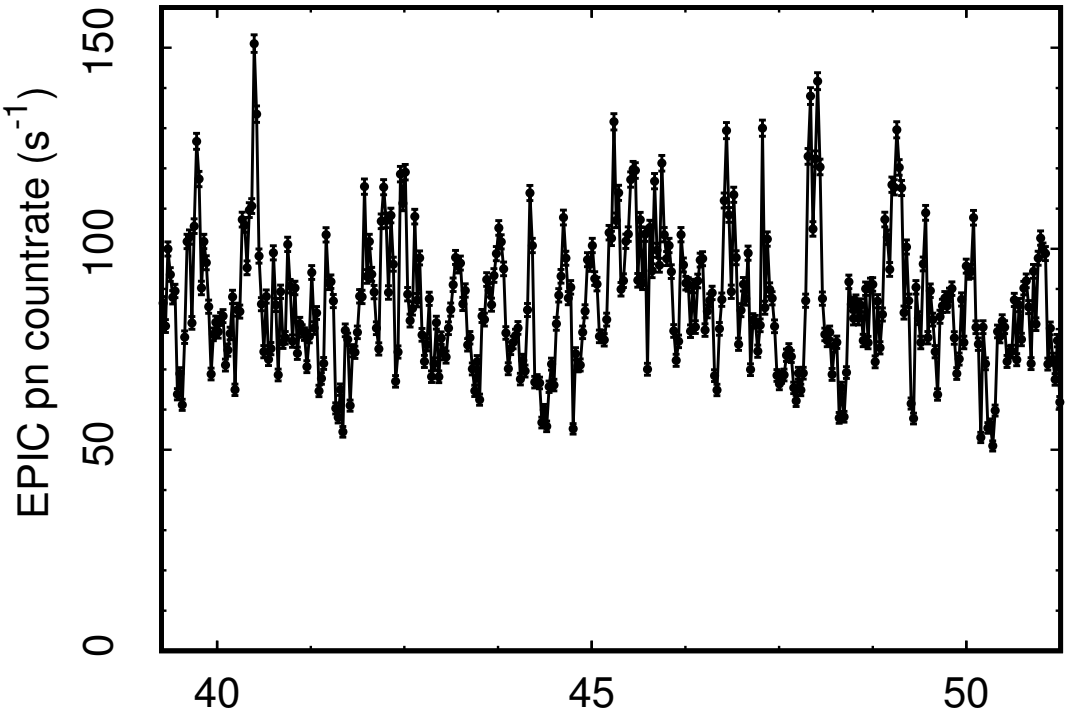

Figure 5.5: Snapshot of the 0.5-10 keV *persistent* light curve observed by the EPIC-pn on-board XMM-Newton. Counts were binned in 32 s-long intervals.

et al. (2015) estimated a likely range for the orbital period between 0.1 and 1.3 d. As the orbital period is likely of the same order of the lenght of the exposure of the observation considered, or shorter, the orbital motion will induce shifts of the frequency of a coherent signal that hamper any periodicity search. We then performed a search on shorter intervals, with a length ranging from 124 to 5500 s. The data acquired during type-I X-ray bursts were discarded. No signal was detected at a confidence level of 3-σ, with an upper limit ranging between 14% and 2%, with the latter limit relative to the longer integration time.

In order to improve the sensitivity to signals affected by the unknown binary orbital motion, we applied the quadratic coherence recovery technique described by Wood et al. (1991) and Vaughan et al. (1994). We divided the entire light curve in time intervals of length equal to $\Delta t = 495$ s. In each of the intervals the time of arrival of X-ray photons t_{arr} were corrected using the relation $t' = \alpha t_{arr}^2$; the parameter α was varied in steps equal to $\delta\alpha = (2\nu_{Ny}\Delta t^2)^{-1} = 9.6 \times 10^{-10}$ s^{-1} to cover a range between $\alpha_{max} = 1.7 \times 10^{-8}$ s^{-1} and $\alpha_{min} = -\alpha_{max}$. The width of the range is determined by a guess on the orbital parameters of the system that would be optimal for an orbital period of 12 h, a donor star mass of $M_2 = 0.3$ M$_\odot$, a NS spin period of $P = 3$ ms, and a donor to NS mass ratio of $q = 0.2$ (see

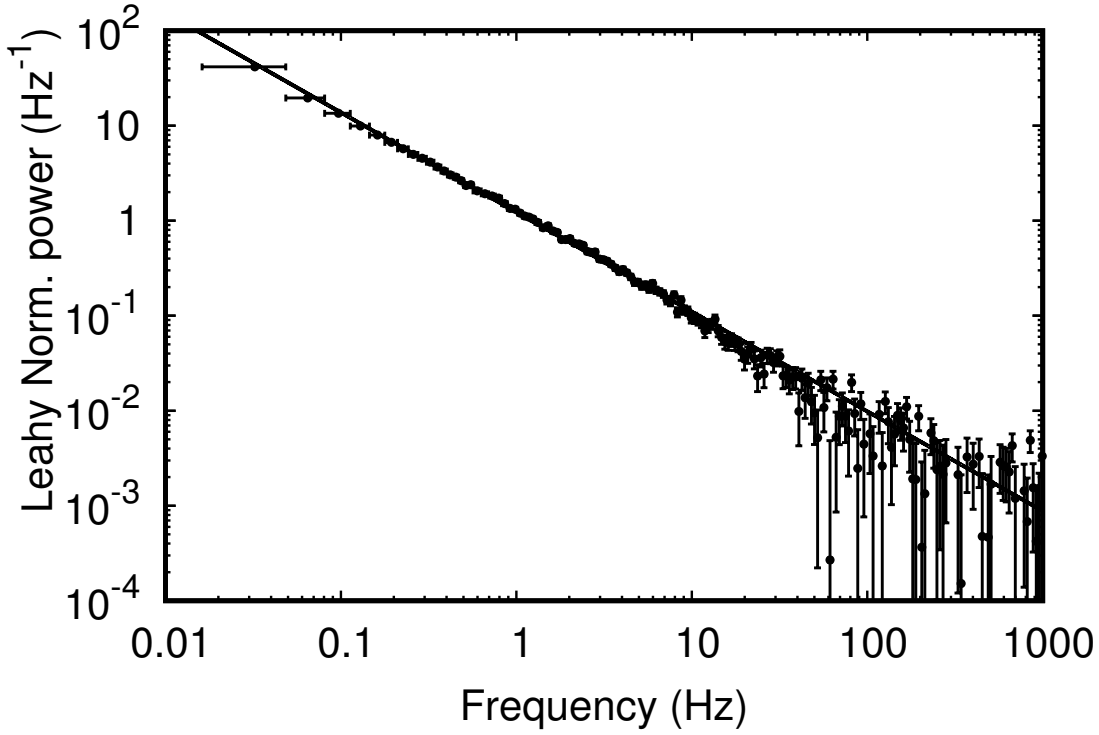

Figure 5.6: Leahy normalized power density spectrum evaluated averaging spectra computed over 8 s-long intervals of the EPIC-pn observation, and re-binning the resulting spectrum as a geometrical series with ratio equal to 1.04. A white noise level equal to 1.99(1) has been subtracted. The solid line represents a power law, $P(\nu) = \nu^{-\alpha}$ with index $\alpha = 1.05$.

Eq. 14 of Wood et al. 1991). This method confirmed the lack of any significant periodic signal, with an 7% on the sinusoidal amplitude. We also considered a shorter time interval of $\Delta\ t = 247$ s, and still obtained no detection within a 3σ c.l. upper limit of 10.5%.

We also searched for burst oscillations in the seven events observed during the *XMM-Newton* exposure. To this aim, we produced power density spectra over intervals of variable length, ranging from 2 to 8 s, and time resolution equal to that used above ($t_{res} = 2.3 \times 10^{-4}$ s). No significant signal was detected in either of the bursts, with 3σ c.l. upper limit on the signal amplitude of the order of $\simeq 20$ and $\simeq 10\%$ for the shorter and longer integration times used, respectively.

5.6 Type I X-ray bursts

Seven bursts took place during the *XMM-Newton* observation, with a recurrence time varying between $t_{rec} = 2.5$ and 4 hours (see Table 5.2). The bursts attained a peak 0.5–10 keV EPIC-pn count rate ranging from 1100 to 1500 counts/s (see top panel of Fig. 5.7 where we plot the light curve of the second burst seen during the *XMM-Newton* exposure). Such values exceed the EPIC-pn telemetry limit (≈450 counts/s), and data overflows occurred close to the burst maximum. The burst rise takes place in less than ≈ 5 s, while the decay could be approximately modeled with an exponential function with an e-folding time scale ranging between 10 and 23 s.

In order to analyze the evolution of the spectral shape during the bursts, we extracted spectra over time intervals of length ranging from 3 to 100 s depending on the count rate. In order to minimize the effect of pile up, which becomes important when the count rate increases above a few hundreds of counts per second, we removed the two brightest columns of the EPIC-pn chip (RAWX=36-37). Background was extracted considering the *persistent emission* observed between 600 and 100 s before the burst onset. The resulting spectra were modeled with an absorbed black-body, fixing the absorption column to the value found in the analysis of the *persistent* emission ($N_H = 2 \times 10^{22}$ cm^{-2}). The evolution of the temperature and apparent radius observed during the second burst, the one with the highest peak flux seen in the *XMM-Newton* observation, are plotted in the middle and bottom panels of Fig. 5.7, respectively. The temperature attained a maximum value of ≈ 3.5 keV and then decreased steadily, confirming the thermonuclear nature of the bursts. The estimated apparent extension of the black-body emission remained always much lower than any reasonable value ex-

pected for the radius of a standard neutron star ($\gtrsim$8-13 km). The maximum flux attained a value of $3.8(7) \times 10^{-8}$ erg cm^{-2} s^{-1} (see Table 5.2), which translate into a luminosity of $1.4(2) \times 10^{38}\, d_{5.5}^2$ erg s^{-1}. This value is both lower than the Eddington limit for a NS and cosmic abundance ($1.76 \times 10^{38}\, (M/1.4\, M_\odot)$ erg s^{-1}) and the luminosity attained during the two bursts characterized by photospheric radius expansion reported by Galloway et al. (2008, $L_{\rm pre} \simeq 2.2 \times 10^{38}\, d_{5.5}^2$ erg s^{-1}). Similar properties were observed also in the other bursts and we concluded that photospheric radius expansion did not occur in any of the bursts observed by *XMM-Newton*.

Table 5.2 lists the energetics of the seven bursts observed by *XMM-Newton*. The persistent flux was evaluated by fitting the spectrum observed from 500 s after the previous burst onset, and 50 s before the actual burst start time, using Model I (see Table 5.1). We measured the fluence $\mathcal{F}$ by summing the fluxes observed in the different intervals over the duration of each burst. We also evaluated the burst timescale as the ratio $\tau = \mathcal{F}/F_{\rm peak}$ (van Paradijs et al., 1988). The rightmost column of table 5.2 displays the parameter α, defined as the ratio between the persistent integrated flux and the burst fluence ($\alpha = c_{\rm bol} F_{\rm pers} t_{rec}/\mathcal{F}$; see, e.g., Galloway et al., 2008), where $c_{\rm bol}$ is a bolometric correction factor that we estimated from the ratio between the flux observed in the 0.5–100 keV and the 0.5–10 keV band with Model II* and II, respectively (see Table 5.1), $c_{\rm bol} = 2.8 \pm 0.3$. We evaluated values of α ranging between 50 and 110, with an average $< \alpha >= 82$.

5.7 Discussion

We analyzed quasi-simultaneous *XMM-Newton* and *INTEGRAL* observations of the transient LMXB EXO 1745–248 in the massive globular cluster Terzan 5, carried out when the source was in the hard state, just after it went into outburst in 2015, with the aim to characterize its broad-band spectrum and its temporal variability properties. We also made use of all additionally available INTEGRAL data collected during the outburst of the source in 2015 to spectroscopically confirm its hard-to-soft state transition occurred around 57131 MJD. This transition was firstly noticed by Tetarenko et al. (2016) using the source lightcurves extracted from Swift/BAT, Swift/XRT, and MAXI.

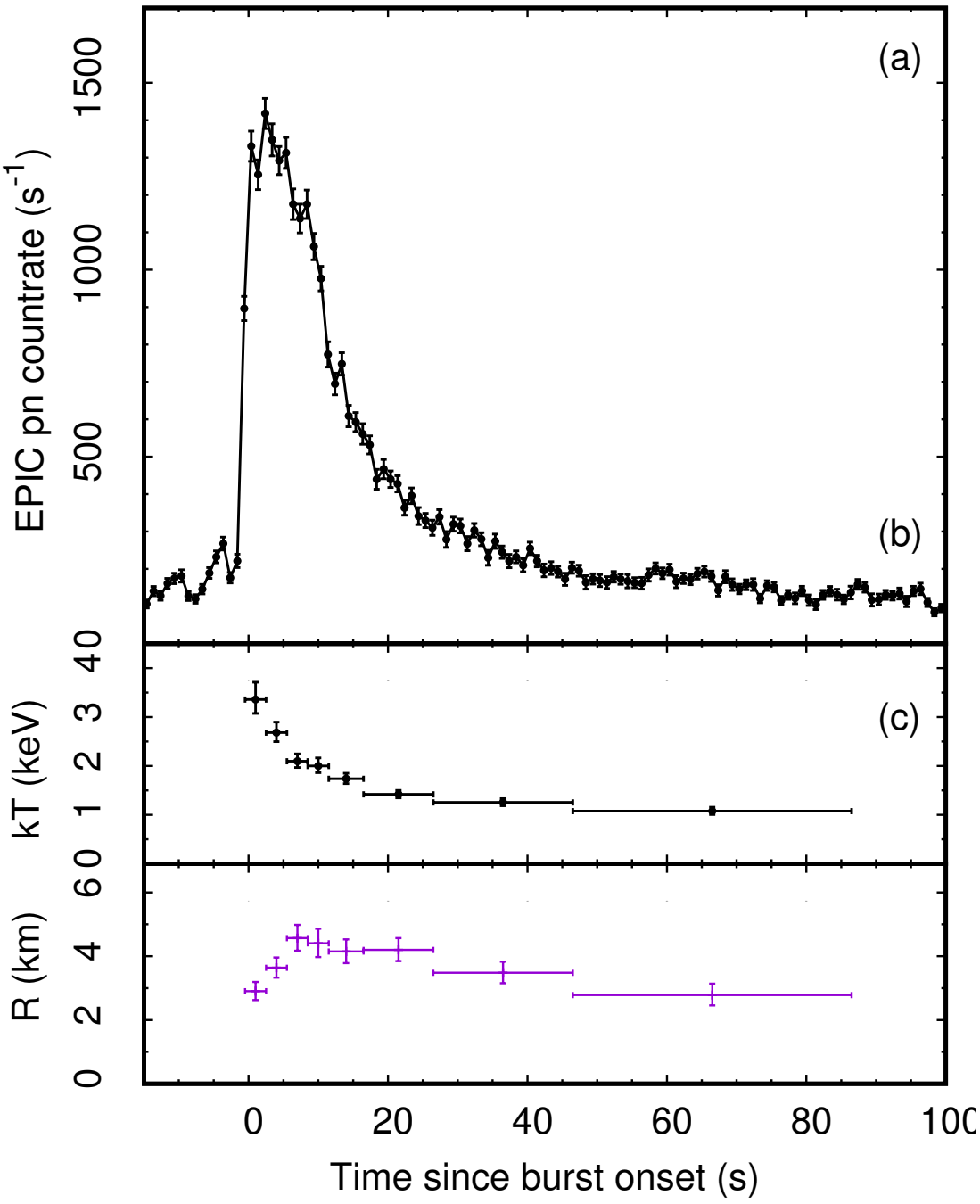

Figure 5.7: 0.5-10 keV light curve of the second burst observed by the EPIC-pn, which begun on $T_2 = 57103.41516$ MJD (top panel). The central and bottom panels show the temperature and apparent radius of the black body used to model the time-resolved spectra, respectively. The radius is evaluated for a distance of 5.5 kpc. Errors are reported with a 90% confidence.

5.7.1 The combined XMM-Newton and INTEGRAL spectrum

We modeled the spec rum observed simultaneously by *XMM-Newton* and *INTEGRAL* to study the X-ray emission from the source in the energy range 0.8–100 keV. We estimated an unabsorbed total luminosity ($0.5-100$ keV energy range) of $\approx 1\times10^{37}\,d_{5.5}^2$ erg s^{-1}. The continuum was well described by a two-component model, corrected by the low-energy effects of interstellar absorption. The best-fit value of the equivalent hydrogen column density, N_H, is $(2.02\pm0.05)\times 10^{22}$ cm^{-2}, slightly lower than the estimate of interstellar absorption towards Terzan 5 given by Bahramian et al. (2014), $N_H = (2.6\pm0.1)\times10^{22}$ cm^{-2}. The two-component continuum model consist of a quite hard Comptonization component, described by the `nthComp` model, with electron temperature $kT_e \sim 40$ keV, photon index $\Gamma \simeq 1.8-2$ and seed-photon temperature of about 1.3 keV, and of a soft thermal component described by a black-body with temperature $kT \sim 0.6-0.7$ keV. The Comptonization component contributed to more than 90 per cent of the flux observed during the observations considered, clearly indicated that the source stayed in the hard state. Assuming a spherical geometry for both the black-body and the seed-photon emitting regions, and ignoring any correction factor due to color temperature corrections or boundary conditions, we found a radius of the black-body emitting region of about $R_{bb} = 3.5-5$ km and a radius of the seed-photon emitting region of about $R_w = 2-3$ km. Given these modest extensions, it is likely that the surfaces of seed photons are related to hot spots onto the neutron star surface. The latter was calculated using the relation reported by in 't Zand et al. (1999), assuming an optical depth of the Comptonization region, $\tau = 2.2\pm0.3$, evaluated using the relation between the optical depth, the temperature of the Comptonizing electrons and the asymptotic power-law index given by Lightman and Zdziarski (1987).

A similar spectral shape was found during the 2000 outburst of EXO 1745–248 observed by *Chandra* and *RXTE* (Heinke et al., 2003a). In that case the continuum model consisted of a multicolor disk black-body, characterized by an inner temperature of $kT = 0.6-1.2$ keV and an inner disk radius of $r_{in}/d_{10}(\cos i)^{0.5} = 4.3-9.2$ km, and a Comptonization component, described by the `comptt` model, characterized by a seed photon temperature of $kT_0 = 1.2-1.7$ keV and radius $R_W = 3.1$ - 6.7 km, an electron temperature of $kT_e = 9.8-10.7$ keV, and an optical depth $\tau = 8$. The Comptonization spectrum was softer during the Chandra/RXTE observations than during the XMM-Newton/INTEGRAL observation analyzed here, and the 0.1-100 keV luminosity was $L_X \approx 6.6\times10^{37}$

erg/sec, higher by about a factor 6 than during our observation. Such a softening of the Comptonization spectrum with increasing luminosity is in agreement with the results presented by Tetarenko et al. (2016) for the 2015 outburst using Swift/XRT data (see their Table 1) and our findings in Sect. 5.3.2 by using the INTEGRAL monitoring data.

Thanks to the large effective area and the moderately-good energy-resolution of the EPIC-pn, we could detect several emission features in the spectrum of EXO 1745-248. Most of the emission features are broad and identified with Kα transitions of highly ionized elements. These are the $2.6-2.7$ keV line identified as S XVI transition (H-like, expected rest frame energy 2.62 keV), the 3.3 keV line identified as Ar XVIII transition (H-like, expected rest-frame energy 3.32 keV), the $3.96-4.1$ keV line identified as Ca XIX or Ca XX transition (He or H-like, expected rest-frame energy 3.9 and 4.1 keV, respectively), and the 6.75 keV line identified as Fe XXV (He-like) transition (expected rest-frame energy 6.7 keV). The Gaussian width of the Fe XXV line we observed from EXO 1745–248, $\sigma_1 = 0.24^{+0.03}_{-0.02}$ keV, is compatible with the width of the Fe line detected during the 2000 outburst (Heinke et al., 2003a). The widths of the low energy lines are compatible with being about half the width of the iron line, in agreement with the expectations from Doppler or thermal Compton broadening, for which the width is proportional to the energy. Therefore all these lines are probably produced in the same emitting region, characterized by similar velocity dispersion or temperature (i.e., the accretion disk).

The fitting of the iron line appears, however, much more complex and puzzling than usual. At least two components are needed to fit the iron emission feature because of highly significant residuals still present after the inclusion in the model of a broad Gaussian. We fitted these residuals using another Gaussian centered at ~ 6.5 keV (therefore to be ascribed to neutral or mildly ionized iron) which appears to be much narrower than the previous component (its width is well below the energy resolution of the instrument and compatible with 0). Driven by a small residual still present at ~ 7 keV and by the expectation that the 6.5-keV $K\alpha$ transition should be accompanied by a 7.1-keV $K\beta$ transition, we also added to the model a narrow Gaussian centered at ~ 7.1 keV, which we identify with the Kβ transition of neutral or mildly ionized iron. Note that the flux ratio of the Kβ transition to the Kα transition reaches its maximum of $0.15-0.17$ for Fe VIII, while it drops to less than 0.1 for charge numbers higher than Fe X-XI (see Palmeri et al., 2003). This suggest that these components originate from low-ionization iron (most probably Fe IVIII) and come from a different region,

plausibly farther from the ionizing central engine, with respect to the other broad and ionized emission lines.

In the hypothesis that the width of the broad lines is due to Doppler and relativistic smearing in the inner accretion disk, we fitted these lines in the EPIC-pn spectrum using relativistic broadened disk-lines instead of Gaussian lines (see Model II and II* in Table 5.1). We obtained a slight improvement of the fit. According to this model we obtained the emissivity index of the disk, $\propto r^{-\beta}$ with $\beta \sim -2.4$, the inner radius of the disk, $R_{in} \sim 14 - 24$ R$_g$, and the inclination angle of the system, $\sim 37°$.

Taking advantage from the broad-band coverage ensured by the almost simultaneous XMM-Newton and INTEGRAL spectra, we also attempted to use a self-consistent reflection model, which takes into account both the discrete features (emission lines and absorption edges, as well as Compton broadening of all these features) and the Compton scattered continuum produced by the reflection of the primary Comptonized spectrum off a cold accretion disk (Model III in Table 5.1). However, we could not obtain a statistically significant improvement of the fit with respect to the disklines model. All the parameters were similar to those obtained with the diskline model. The only change in the smearing parameters we get using the reflection model instead of disklines is in the value of the inner disk radius, which is now constrained to be < 8.5 R$_g$. The reflection component required a ionization parameter of $\log \xi \sim 2.7$, consistent the high ionization degree of the broad lines, and a reflection fraction (that is the solid angle subtended by the reflector as seen from the corona, $\Omega/2\pi$) of about 0.22. A non significant improvement in the description of the spectrum ($\Delta\chi^2 \simeq -5$ for the addition of two parameters) was obtained when using pexriv to model the reflection continuum (Model IV, see Table 5.1 with respect to best fit model (Model II* in Tab 5.1). The observation analyzed here were then not sufficient to ascertain with statistical significance whether a reflection continuum is present in the spectrum.

The smearing parameters of the reflection component were similar to what we find for other sources. The emissivity index of the disk, ~ -2.5, the inner radius of the disk, about 30 km or below 13 km, according to the model used for the reflection component, as well as the inclination with respect to the line of sight, $35 - 40°$, are similar to the corresponding values reported in literature for many other sources (see e.g. Di Salvo et al., 2015b, and references therein). For instance, in the case of atoll LMXB 4U 1705–44 the inner disk radius inferred from the reflection component lay around $14 - 17$ R$_g$ both in the soft and in the hard state,

changing very little (if any) in the transition from one state to the other (di Salvo et al., 2009; Egron et al., 2013b; Di Salvo et al., 2015b). In the case of 4U 1728–34, caught by *XMM-Newton* in a low-luminosity (most probably hard) state, the inner disk radius was constrained to be $14-50$ R_g (Egron et al., 2011b). Even in the case of accreting millisecond pulsars (AMSPs), which are usually found in a hard state and for which we expect that the inner disk is truncated by the magnetic field, inner disk radii in the range $6-40$ R_g were usually found (see, e.g. Papitto et al., 2009b; Cackett et al., 2009b; Papitto et al., 2010b, 2013b; Pintore et al., 2016b; King et al., 2016). Also, the reflection fraction inferred from the `rfxconv` model, $\Omega/2\pi \sim 0.22$, although somewhat smaller than what is expected for a geometry with a spherical corona surrounded by the accretion disk ($\Omega/2\pi \sim 0.3$), is in agreement with typical values for these sources. Values of the reflection fraction below or equal 0.3 were found in a number of cases (e.g. Di Salvo et al., 2015b; Degenaar et al., 2015; Pintore et al., 2015b, 2016b; Ludlam et al., 2016; Chiang et al., 2016b). More puzzling is the high ionization parameter required from the broad emission lines, $\log \xi \sim 2.7 - 2.8$, where $\xi = L_X/(n_e r^2)$ is the ionization parameter, L_X is the bolometric luminosity of the central source and n_e and r are the electron density in the emitting region and the distance of the latter from the central source, respectively. This high value of the ionization parameter is quite usual in the soft state, while in the hard state a lower ionization is usually required, $\log \xi < 2$. This was clearly evident in the hard state of 4U 1705-44 (Di Salvo et al., 2015b), although in that case the luminosity was $\sim 6 \times 10^{36}$ ergs/s, about a factor 2 below the observed luminosity of EXO 1745-248 during the observations analysed here.

Perhaps the most unusual feature of this source is the simultaneous presence in its spectrum of a broad ionized iron line and at least one narrow, neutral or mildly ionized iron line, both in emission and clearly produced in different regions of the system. Sometimes, in highly inclined sources, broad iron emission lines were found together with highly ionized iron lines in absorption, clearly indicating the presence of an out-flowing disk wind (see, e.g., the case of the bright atoll source GX 13+1; Pintore et al., 2014, and references therein). In the case of 4U 1636-536, Pandel et al. (2008c) tentatively fitted the very broad emission feature present in the range $4-9$ keV with a combination of several Kα lines from iron in different ionization states. In particular they fitted the iron complex with two broad emission lines with centroid energies fixed at 6.4 and 7 keV, respectively. However, to our knowledge, there is no other source with a line complex modeled by one broad and one (or two) narrow emission features, as the one showed by

EXO 1745-248. While a natural explanation for the broad, ionized component is reflection in the inner rings of the accretion disk, the narrow features probably originate from illumination of an outer region in which the motion of the emitting material is much slower, as well as the corresponding ionization parameter. Future observation with instruments with a higher spectral resolution will be needed to finely deconvolve the line shape, and firmly assess the origin of each component.

5.7.2 Temporal variability

The high effective area of the EPIC-pn on board *XMM-Newton*, combined with its μs temporal resolution, make it the best instrument currently flying to detect coherent X-ray pulsations, and in particular those with a period of few milliseconds expected from low magnetic field NS in LMXBs. We performed a thorough search for periodicity in the EPIC-pn time series observed from EXO 1745–248, but found no significant signal. The upper limits on the pulse amplitude obtained range from 2 to 15% depending on the length of the intervals considered, the choice of which is a function of the unknown orbital period, and on the application of techniques to minimize the decrease of sensitivity to pulsations due to the orbital motion. Such upper limits are of the order, and sometimes lower than the amplitudes usually observed from AMSPs (see, e.g., Patruno and Watts, 2012). Though not excluding the possibility of low amplitude pulsations, the non detection of a signal does not favor the possibility that EXO 1745–248 hosts an observable accreting millisecond pulsar (AMSP). This is also hinted by the significantly larger peak luminosity reached by EXO 1745–248 during its outbursts ($\sim 7 \times 10^{37}$ erg s^{-1}) with respect to AMSPs ($\approx$ few $\times 10^{36}$ erg s^{-1}). Together with the long outburst usually shown (t$\sim$ 100 d), such a large X-ray luminosity suggests that the long term accretion rate of EXO 1745–248 is more than ten times larger than in AMSPs. A larger mass accretion rates is though to screen the NS magnetic field (Cumming et al., 2001b), possibly explaining why ms pulsations are observed only from relatively faint transient LMXBs.

At the moment of writing this thesis, the orbital parameters of EXO 1745–248 were not known. Recently, Ferraro et al. (2015) showed that the location of the optical counterpart of EXO 1745–248 in the color-magnitude diagram of Terzan 5 is close to the cluster turnoff, and is compatible with a 0.9 M$_\odot$ sub-giant branch star if it belongs to the low metallicity population of Terzan 5. In such a case the mass transfer would have started only recently. The orbital period would be $\sim$ 0.9 days and the optimal integration time to perform a search for periodicity $\sim 920\,(P_s/3\mathrm{ms})^{1/2}$ s, where P_s is the spin period of the putative pulsar (when not

performing an acceleration search; see Eq. 21 in Johnston and Kulkarni (1991), evaluated for a sinusoidal signal and an inclination of 37°). The upper limit on the signal amplitude we obtained by performing a signal search on time intervals of this length is 5%.

A useful comparison can be made considering the only accreting pulsar known in Terzan 5, IGR J17480–2446, a NS spinning at a period of 90 ms, hosted in a binary system with an orbital period of 21.3 hr (Papitto et al., 2011). Its optical counterpart in quiescence also lies close to the cluster turnoff (Testa et al., 2012). The relatively long spin period of this pulsar and its relatively large magnetic field compared to AMSP, let Patruno et al. (2012) to argue that the source started to accrete and spin-up less than a few 10^7 yr, and was therefore caught in the initial phase of the mass transfer process that could possibly accelerate it to a spin period of few milliseconds. When the IGR J17480–2446 was found in a hard state, X-ray pulsations were observed at an amplitude of 27 per cent, decreasing to a few per cent after the source spectrum became softer and cut-off at few keV (Papitto et al., 2012). The upper limit on pulsations obtained assuming for EXO 1745–248 similar parameters than IGR J17480–244 is 2%, of the order of the amplitude of the weaker pulsations observed from IGR J17480–244.

On the other hand, if the companion star belongs to the metal-rich population of Terzan 5, it would be located in the color-magnitude diagram at a position where companions to redback millisecond pulsars are found (Ferraro et al., 2015). In such a case a spin period of few millisecond would be expected for the NS, and upper limits ranging from 5 to 15% on the pulse amplitude would be deduced from the analysis presented here, depending on the orbital period. For comparison, the redback transitional ms pulsar IGR J18245–2452 in the globular cluster M28 showed pulsations with amplitude as high as 18%, that were easily detected in an *XMM-Newton* observation of similar length as the one presented here (Papitto et al., 2013c; Ferrigno et al., 2014). This further suggests that EXO 1745–248 is unlikely an observable accreting pulsar, unless its pulsations are weak with respect to similar systems and/or it belongs to a very compact binary system. Neither a search for burst oscillations yielded to a detection, with an upper limit of $\approx$ 10% on the pulse amplitude, and therefore the spin period of the NS in EXO 1745–248 remains undetermined.

5.7.3 Type-I X-ray bursts

Seven type-I X-ray bursts were observed during the 80 ks *XMM-Newton* observation presented here, with a recurrence time varying from 2.5 to 4 hours.

None of the bursts showed photospheric radius expansion, and all the bursts observed had a relatively long rise time ($\sim$ 2–5 s) and decay timescale (τ = 15–23 s, except the second, brightest burst which had $\tau \simeq 10$ s). Bursts of pure helium are characterized by shorter timescales ($\tau < 10$ s) and we deduce that a fraction of hydrogen was probably present in the fuel of the bursts we observed. More information on the fuel composition can be drawn from the ratio between the integrated persistent flux and the burst fluence, α. This parameter is related to the ratio between the efficiency of energy conversion through accretion onto a compact object (GM_*/R_*) and thermonuclear burning ($Q = 1.6 + 4 < X >$ MeV nucleon^{-1}, where $< X >$ is the abundance of hydrogen burnt in the burst), $\alpha = 44\,(Q_{\rm nuc}/4.4$ MeV nucleon$^{-1})^{-1}$ for a 1.4 $M_\odot$ NS with a radius of 10 km (see Eq. 6 of Galloway et al., 2008, and references therein). The observed values of α range from 50 to 100, with an average of 82, indicating that hydrogen fraction in the bursts was $< X > \approx 0.2$. Mass accretion rate should have then been high enough to allow stable hydrogen burning between bursts, but part of the accreted hydrogen was left unburnt at the burst onset and contributed to produce a longer event with respect to pure helium bursts. Combined hydrogen-helium flashes are expected to occur for mass accretion rates larger than $\simeq 0.1\,\dot{m}_{\rm Edd}$ (for solar metallicity, lower values are expected for low metallicity, Woosley et al., 2004), where $\dot{m}_{\rm Edd}$ is the Eddington accretion rate per unit area on the NS surface (8.8×10^4 g cm^{-2} s, or 1.3×10^{-8} M$_\odot$ yr^{-1} averaged over the surface of a NS with a radius of 10 km). The persistent broadband X-ray luminosity of EXO 1745–248 during the observations considered here indicates a mass accretion rate of $8.5 \times 10^{-10}\,d_{5.5}^2 \simeq 0.05\,\dot{M}_{\rm Edd}$ M$_\odot$ yr^{-1} for a 1.4 M$_\odot$ NS with a 10 km radius, lower than the above threshold not to exhaust hydrogen before the burst onset. A low metallicity could help decreasing the steady hydrogen burning rate and leave a small fraction of hydrogen in the burst fuel.

The seven bursts observed during the *XMM-Newton* observation analyzed here share some of the properties of the 21 bursts observed by *RXTE* during the 2000 outburst before the outburst peak, such as the decay timescale, $\tau \approx 25$ s, and the peak and persistent flux $F_{\rm peak} = (3$–$19) \times 10^{-9}$ erg cm^{-2} s^{-1}, $F_{\rm pers} = (1$–$5) \times 10^{-9}$ erg cm^{-2} s^{-1} and the absence of photospheric radius expansion (see Table 10 and appendix A31 in Galloway et al., 2008). However those bursts showed recurrence times between 17 and 49 minutes, and correspondingly lower values of $\alpha = 20$–46 with respect to those observed here. The observation of frequent, long bursts and infrequent, short bursts at similar X-ray luminosity made Galloway et al. (2008) classify EXO 1745–248 as an *anomalous* burster. The observations

presented here confirm such a puzzling behavior for EXO 1745–248. We note that 4 additional type-I bursts were detected by *INTEGRAL* during the monitoring observations of EXO 1745–248. As we discussed in previous sections we did not perform a spectroscopic analysis of these events due to the limited statistics of the two JEM-X units and the lack of any interesting detection in ISGRI which could have indicated the presence of a photospheric radius expansion phase.

Table 5.1: Best fitting models of the spectrum observed from EXO 1745–248. Fluxes are unabsorbed and expressed in units of 10^{-10} erg cm^{-2} s^{-1}. For the fits of the EPIC-pn spectrum alone (second and third column) the fluxes are evaluated in the 0.5–10 keV energy band, while they are calculated in the 0.5–100 keV range for the broadband spectrum (fourth and fifth columns). The normalization of the lines are expressed in units of 10^{-4} ph cm^{-2} s^{-1}.

	EPIC-pn (2.4–11 keV)		Broadband (0.35–180 keV)		
Parameter	Model I	Model II	Model II*	Model III	Model IV
N_H ($\times 10^{22}$ cm^{-2})	(2.0)	(2.0)	2.02 ± 0.04	2.13 ± 0.05	2.06 ± 0.05
kT_{th} (keV)	$0.58^{+0.03}_{-0.06}$	$0.64^{+0.04}_{-0.02}$	0.63±0.04	0.73 ± 0.03	$0.64^{+0.02}_{-0.06}$
R_{bb} ($d_{5.5}$ km)	$5.5^{+0.8}_{-0.4}$	4.6 ± 0.2	4.5 ± 0.5	3.8 ± 0.2	4.4 ± 0.4
Γ	$2.06^{+0.08}_{-0.12}$	$2.02^{+0.19}_{-0.09}$	1.93 ± 0.07	1.89 ± 0.08	1.90 ± 0.05
kT_e (keV)	(37.0)	(37.0)	$37.2^{+6.9}_{-5.1}$	40^{+7}_{-5}	$33.6^{+5.7}_{-4.4}$
kT_{in} (keV)	$1.33^{+0.06}_{-0.14}$	1.3 ± 0.1	1.27 ± 0.06	1.34 ± 0.07	$1.25^{+0.08}_{-0.04}$
$F_{nthcomp}$	8.0 ± 0.2	$7.9^{+0.2}_{-0.3}$	24.9 ± 2.2	23.8 ± 2.1	21.6 ± 2.1
R_w	1.6 ± 0.3	1.5 ± 0.3	2.8 ± 0.3	2.4 ± 0.3	2.5 ± 0.4
$\beta_{\rm Irr}$	...	$-2.44^{+0.04}_{-0..06}$	-2.44 ± 0.07	-2.24 ± 0.07	-2.43 ± 0.05
R_{in} (R_g)	...	20^{+4}_{-6}	20 ± 6	< 8.5	$18.3^{+3.9}_{-6.2}$
R_{out} (R_g)	...	(10^7)	(10^7)	(10^7)	(10^7)
i (°)	...	37^{+2}_{-3}	37 ± 3	38 ± 1	$37.2^{+2.1}_{-1.7}$
$\Omega_r/2\pi$	...	...	...	0.22 ± 0.04	(0.22)
$log\xi$	...	...	...	2.70 ± 0.07	$2.39^{+0.41}_{-0.27}$
T_{disk} (k)	...	...	...	...	(10^6)
E_1 (keV)	$6.75^{+0.02}_{-0.03}$	6.75 ± 0.02	6.74 ± 0.02	...	6.75 ± 0.02
σ_1 (keV)	$0.24^{+0.03}_{-0.02}$	...	...	...	...
N_1	$6.0^{+0.7}_{-0.5}$	$6.6^{+0.6}_{-0.4}$	7.1 ± 0.1	...	$6.7^{+0.2}_{-0.4}$
EW_1 (eV)	62.0 ± 0.02	68.2 ± 0.04	72.9 ± 2.5	...	68.6 ± 2.4
E_2 (keV)	$6.48^{+0.03}_{-0.01}$	6.50 ± 0.01	6.50 ± 0.02	6.49 ± 0.02	6.49 ± 0.02
σ_2 (keV)	(0.0)	(0.0)	(0.0)	(0.0)	(0.0)
N_2	2.8 ± 0.3	3.2 ± 0.2	3.2 ± 0.2	2.4 ± 0.2	3.2 ± 0.3
EW_2 (eV)	26.8 ± 0.02	31.6 ± 0.2	31.3 ± 1.4	23.1 ± 1.9	31.1 ± 1.9
E_3 (keV)	$7.12^{+0.04}_{-0.07}$	7.09 ± 0.07	(7.06)	(7.06)	(7.06)
σ_3 (keV)	(0.0)	(0.0)	(0.0)	(0.0)	(0.0)
N_3	(N_2/10)	(N_2/10)	(N_2/10)	(N_2/10)	(N_2/10)
EW_3 (eV)	3.1 ± 0.1	3.6 ± 0.1	3.5 ± 0.7	2.7 ± 0.8	3.5 ± 0.9
E_4 (keV)	$2.74^{+0.01}_{-0.03}$	2.68 ± 0.03	2.67 ± 0.03	$2.67^{+0.01}_{-0.02}$	2.67 ± 0.03
σ_4 (keV)	(0.0)	...	...	...	...
N_4	$1.0^{+0.2}_{-0.1}$	2.0 ± 0.4	2.3 ± 0.4	1.2 ± 0.4	2.2 ± 0.3
EW_4 (eV)	3.8 ± 0.2	7.5 ± 0.4	8.4 ± 1.1	4.2 ± 0.9	8.0 ± 1.3
E_5 (keV)	3.30 ± 0.03	3.29 ± 0.02	3.27 ± 0.04	3.28 ± 0.03	3.29 ± 0.03
σ_5 (keV)	$0.13^{+0.04}_{-0.02}$	...	...	...	...
N_5	$2.5^{+0.6}_{-0.7}$	2.1 ± 0.3	2.1 ± 0.3	$1.7^{+0.2}_{-0.5}$	$1.8^{+0.3}_{-0.5}$
EW_5 (eV)	11.5 ± 0.1	9.2 ± 0.1	9.5 ± 1.2	7.2 ± 1.1	8.8 ± 1.1
E_6 (keV)	$3.94^{+0.05}_{-0.06}$	3.96 ± 0.02	3.96 ± 0.05	4.01 ± 0.05	3.96 ± 0.05
σ_6 (keV)	$0.26^{+0.10}_{-0.07}$	...	...	...	...
N_6	$2.8^{+1.8}_{-0.9}$	1.6 ± 0.3	2.21 ± 0.05	1.2 ± 0.4	$1.5^{+0.1}_{-0.3}$
EW_6 (eV)	15.4 ± 0.2	8.5 ± 0.1	8.3 ± 0.9	6.3 ± 1.9	8.1 ± 1.2
RGS1/EPN	...	...	1.04 ± 0.02	$1.08^{+0.01}_{-0.03}$	1.06 ± 0.03
RGS2/EPN	...	...	1.03 ± 0.02	$1.08^{+0.01}_{-0.03}$	1.03 ± 0.02
JEMX1/EPN	...	...	1.30 ± 0.06	1.27 ± 0.05	1.29 ± 0.06
JEMX2/EPN	...	...	1.11 ± 0.05	1.08 ± 0.05	1.10 ± 0.05
ISGRI/EPN	...	...	$1.27^{+0.05}_{-0.09}$	1.09 ± 0.04	1.20 ± 0.07
Flux	9.34 ± 0.01	9.23 ± 0.03	26 ± 3	28 ± 3	26 ± 3
χ^2 (d.o.f.)	1.457 (106)	1.338 (106)	1.152 (1083)	1.173 (1083)	1.1487 (1081)
$p_{\rm null}$	1.5×10^{-3}	1.1×10^{-2}	3.6×10^{-4}	6.1×10^{-5}	4.6×10^{-4}

Table 5.2: Properties of the type-I X-ray bursts observed by XMM-Newton.

No.	Start time (MJD)	t_{rec} (s)	$F_{\rm pers}$	$F_{\rm peak}$	$\mathcal{F}$	τ (s)	α
I	57103.26624	...	0.99(2)	17(2)	38(3)	22.7 ± 3.4	
II	57103.41516	12866	0.955(7)	38(7)	40(6)	10.5 ± 2.6	86 ± 16
III	57103.56912	13303	0.924(6)	18(2)	31(3)	16.5 ± 3.0	111 ± 12
IV	57103.67557	9197	0.91(1)	21(3)	42(5)	20.4 ± 3.8	56 ± 6
V	57103.84017	14221	0.868(4)	29(4)	44(5)	18.8 ± 2.8	79 ± 9
VI	57103.96830	11071	0.929(5)	24(3)	38(4)	16.2 ± 2.8	76 ± 11
VII	57104.10384	11710	0.922(4)	22(3)	37(4)	17.1 ± 3.1	82 ± 12

4

Chapter 6

General Conclusions

This PhD thesis is dedicated to the spectral study of a sample of properly chosen neutron star Low Mass X-ray Binaries (LMXB). The sources in the analyzed sample are 4U 1705-44, Serpens X-1, and the transient source EXO 1745-248.

In the case of 4U 1705-44 the broad-band ($0.5 - 200$ keV) spectrum was acquired with the Japanese X-ray observatory *Suzaku* with the aim of study the reflection spectrum in this source during a hard state and to make a comparison of the derived spectral parameters with those obtained during the more luminous soft state of the source. We find that the reflection parameters are very similar in the two states of the source, the main difference being in the ionization parameter which is much higher during the soft state, as expected. Other parameters, such as the inclination angle of the system with respect to the line of sight or the inner disk radius, were instead very similar. In particular, the accretion disk in the hard state appears to be truncated at a radius comparable to that found during the soft state, indicating that the disk does not recede significantly in the hard state, where the mass accretion rate is lower than in the soft state.

Serpens X-1 was observed with the NASA X-ray observatory NuSTAR ($3-200$ keV energy) during a high luminosity state, with the aim to fit its broad-band spectrum, derive the reflection parameters, and compare these with the results obtained by (Miller et al., 2013) who have analyzed the same data. (Miller et al., 2013) found that fitting the NuSTAR spectrum with relativistically blurred disk reflection models suggest that the disk likely extends close to the innermost stable circular orbit (ISCO) or stellar surface. We have re-analysed these data together with XMM-Newton data from a previous observation of this source and fitted these spectra with slightly different continuum and reflection models with respect to those previously adopted for this source, yielding consistent spectral results for the NuSTAR and XMM-Newton spectra. Our results are less extreme with

respect to those found by (Miller et al., 2013). In particular, we find that the inner disk radius is relatively far form the ISCO, at $\sim$ 30 km from the neutron star center, in line with what is usually found for neutron star systems.

Finally, in collaboration with Dr. Alessandro Papitto at the Institute of Space Sciences in Barcelona (Spain), I have analyzed the high resolution and broad band spectra of EXO 1745-248, observed with the instruments on board of the ESA satellites XMM-Newton and INTEGRAL. The spectral analysis of this interesting source has shown the presence, at the same time, of narrow lines at 6.4 and 7.05 keV, identified as the Kα and Kβ transitions of neutral iron, together with a broad emission line at 6.7 keV, identified as the Kα transition of He-like Fe, which appears broad and is probably produced by reflection off the inner accretion disk. Besides these complex iron emission lines, we also detect the presence of broad low-energy emission lines, identified as Kα transitions of SXVI, ArXVII and CaXIX-XX. The analysis has shown that there are at least two different emission regions in this source: one with weakly ionized plasma that produces the narrow features, and the other strongly ionized that produces the broad features which is likely localized at the inner edge of the accretion disk. For this source, as well as for the other two sources of our sample, we have performed a detailed spectral analysis, the X-ray spectra of these sources have been fitted using both phenomenological models (where the emission lines are modelled either with Gaussians or Disklines) and with self-consistent reflection models, although in the case of EXO 1745-248 the analysis has been complicated by the presence of additional discrete features in the final best-fit model.

We have analyzed these sources in a hard or soft state. In all the cases, in order to obtain a good fit of the broad-band spectrum, we had to add a reflection component. In all spectra the inner disk radius, R_{in} is about $30-35$ km from the neutron star center indicating that we are probing the region very close to the neutron star. Moreover the value of the reflection fraction, defined as the solid angle subtended by the reflector, i.e. the disk, as seen from the corona in units of 2π ($f_{refl} = \Omega/2\pi$), is usually in the range 0.2-0.3, compatible with a geometry of central corona with an outer accretion disk. The fact that R_{in} is always about 30 km in both soft and hard state, seems to exclude the model proposed for the black hole binaries where the inner radius of the disk is receding in the hard state (Esin et al., 1997). This difference may be related to the fact that a neutron star, contrary to black holes, has a solid surface.

Appendix A

Instruments for X-ray observations

The X-ray observations presented and analyzed in this thesis are performed by satellites orbiting around the Earth. From these observations X-ray spectra have been extracted and analyzed. In general these spectra cover an energy range between 0.4 and 500 keV and have been obtained using the instruments on board the following X-ray observatories: SUZAKU, XMM-Newton, INTEGRAL, and NuSTAR satellites.

In particular, 4U 1705–44 is a LMXB of the atoll class, and has been observed by the SUZAKU satellite for about 100 ks, in Feb 2014, during a 'hard' state. This observations has been performed as a predicted *'Target of Opportunity' (ToO)* program, in order to catch the source at a low luminosity level. Serpens X-1 is an atoll source and has been observed by NuSTAR satellite for about 80 ksec, in Aug 2014, during 'soft' state. EXO 1745–248, that is a transient source of the atoll class, has been observed by XMM-Newton and INTEGRAL satellites for about 75 ks, in March 2015, just after the onset of an X-ray outburst. This observation has been performed as *'Target of Opportunity' (ToO)* program.

Most current missions operating in the soft X-ray range (E¡10 keV) are equipped with X-ray CCDs. They provide substantially better spectral resolution than proportional counters (used in previous generation of X-ray satellites), allowing measures with higher precision of emission lines such as the Fe line in the $6.4 - 6.97$ keV energy range, as well as better estimations for the column density of absorbing material, thanks to their low-energy sensitivity, and for the electron temperature of the hot diffuse plasmas and the power-law photon index in non-thermal plasmas, thanks to their broad-band capabilities.

In Figure A.1 I give a schematic picture of the most important X-ray satellites

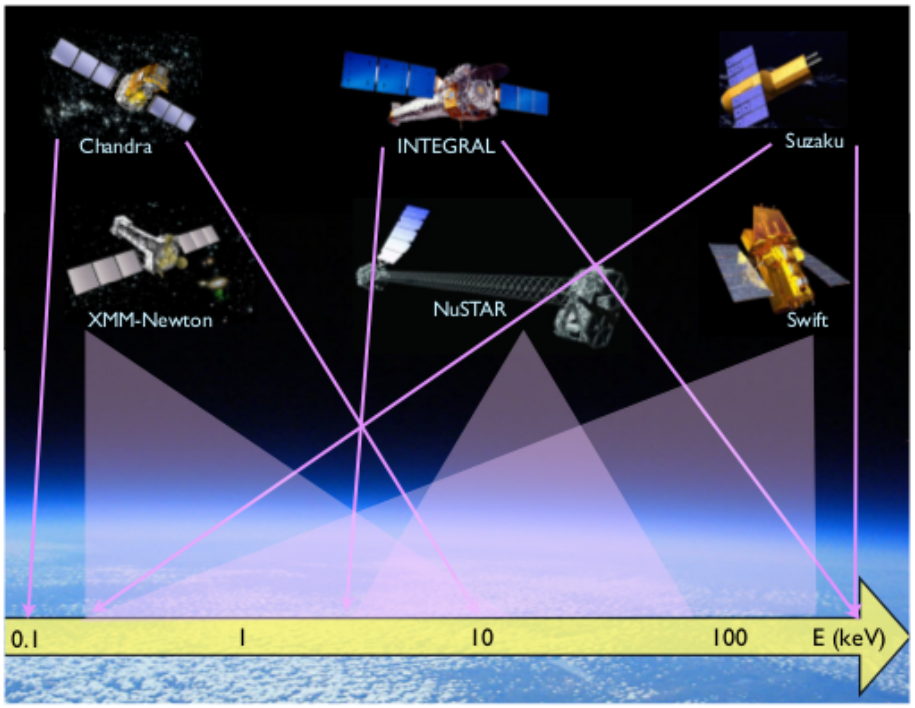

Figure A.1: The actual generation of X-ray satellites covering a wide spectral range, from 0.1 to 500 keV. See text for more details.

available today as well as of the spectral range they cover. In the following sections I give a short overview of the X-ray observatories used for this thesis.

A.1 SUZAKU

Suzaku is the fifth Japanese X-ray satellite, funded by the Japan Aerospace Exploration Agency (JAXA) and the NASA. Since 2005, it has performed various observational studies for a wide variety of X-ray sources, with a high energy resolution and a high sensitivity over a wide energy range from 0.3 to 600 keV. Suzaku is dedicated to the study of hot plasmas in various X-ray sources, to the structure and evolution of clusters of galaxies, and to the spectroscopy and accretion flow of black hole candidates, neutron star binaries, and Active Galactic Nuclei.

The main instruments on board Suzaku (Mitsuda et al., 2007) are: The X-ray Spectrometer (XRS) consisting of a micro-calorimeter with very high energy resolution for X-ray spectroscopic studies, which was the spacecraft's primary instrument. Because of a malfunctioning of the cooling system, which occurred just after the launch of the satellite in July 2005, the entire reservoir of liquid

helium was lost and this caused the shut down of the spectrometer. The X-ray Imaging Spectrometer (XIS) is composed of four imaging CCD cameras (three working) sensitive in the $0.2 - 12$ keV band, each located at the focal plane of a dedicated X-ray telescope. Finally, at high energy there is a non-imaging, collimated Hard X-ray Detector (HXD), a solid state detector sensitive in the 10-600 keV band.

A.2 NuSTAR

NuSTAR (Nuclear Spectroscopic Telescope Array) (Harrison et al., 2013) focuses on the hard X-ray sky. It is the first X-ray telescope able to produce images at hard X-rays (up to ~ 80 keV). Launched on June 13 2012 by the NASA, it uses grazing incidence optics with long focal lengths (upon entry into space, it extended to its full length of 10 meters) in order to obtain both a good angular resolution and a low background. NuSTAR has the main aim to study the hidden Universe, the distribution of black holes through the cosmos to understand how they affect the formation of galaxies, what powers the most extreme active galactic nuclei, but also the distribution of stellar remnants in the Galaxy, the chemical enrichment from star explosions, non-thermal processes, etc.

The NuSTAR focal planes include four hybrid hard X-ray detectors consisting of a CdZnTe sensor. Each of the four hybrids (placed in a 2 x 2 array in the focal plane) is segmented into 32 x 32 pixels, each subtending 12.5" on the sky. The detectors measure the arrival time, energy and position of interaction of each incident X-ray.

A.3 XMM-Newton

The X-ray Multi-Mirror Mission (XMM-Newton) is an X-ray satellite launched by the European Space Agency (ESA) in December 1999. Named after physicist and astronomer Sir Isaac Newton, the mission is designed to investigate cosmic X-ray sources, performing narrow- and broad-range spectroscopy, and performing the first simultaneous imaging of objects in both X-ray and optical (visible and ultraviolet) wavelengths. Originally scheduled for a two-year mission, the spacecraft remains in good health and has received mission extensions and still working to date.

The instruments on board the XMM-Newton satellite (Jansen et al., 2001) are: the three units of the European Photon Imaging Camera (EPIC), which is

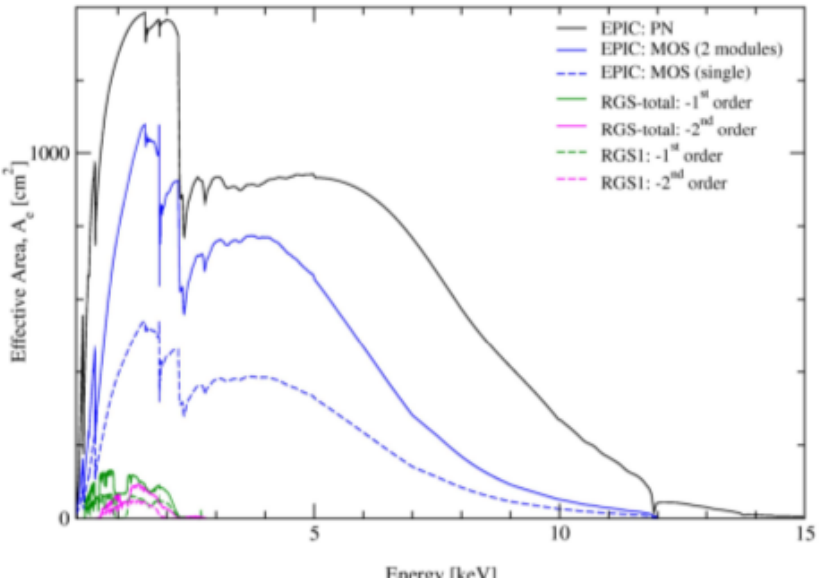

Figure A.2: Effective area of the XMM-Newton X-ray telescopes, EPIC-pn, EPIC-MOS and RGS with a maximum at about 1.5 keV. A pronounced edge near 2 keV is associated to the Au edge. The effective areas of the two MOS cameras are lower than that of the pn, because only part of the incoming radiation falls onto these detectors. The remaining part goes to the RGS for spectroscopic studies. From the XMM-Newton Users handbook.

the primary instrument. The system is composed of two MOS-CCD cameras and a single pn-CCD camera, with a total field of view of 30 arcminutes and an energy sensitivity range between 0.15 and 15 keV and with imaging capabilities. The Reflection Grating Spectrometers (RGS) are composed of two Focal Plane Cameras and their associated Reflection Grating Arrays. This system is used to build X-ray spectral data with high energy resolution for X-ray spectroscopic studies. The RGS system operates in the 2.5 to 0.35 keV range, which allows detection of carbon, nitrogen, oxygen, neon, magnesium, silicon, and iron L-shell features. The two reflection grating spectrometers (RGS1 and RGS2), can operate simultaneously, with the three EPIC cameras and with a co-aligned optical telescope (Optical Monitor, OM). The OM is sensitive between 170 and 650 nanometres in a 17×17 arcminute square field of view co-aligned with the centre of the X-ray telescope's field of view. In Figure A.2 the effective area of the instruments on board XMM-Newton is shown.

A.4 INTEGRAL

INTEGRAL (INTErnational Gamma-Ray Astrophysics Laboratory) (Winkler et al., 2003b) is an ESA mission and celebrated the 10th anniversary of its launch in October 2012. Initially planned for a duration of 2 years, this ESA scientific mission dedicated to hard X-ray and gamma-ray imaging of the sky, is still operating. INTEGRAL uses coded aperture mask technique for three of its instruments. Its main science objectives are compact objects, extragalactic astronomy, stellar nucleosynthesis, the Galactic center, identification of high energy sources, particle processes and acceleration.

Four instruments are co-aligned to study a target across a broad energy range, from hard X-rays to gamma-rays. The INTEGRAL imager, IBIS (Imager on-Board the INTEGRAL Satellite) observes from 15 keV (hard X-rays) to 10 MeV (gamma-rays). Angular resolution is 12 arcmin, enabling a bright source to be located to better than 1 arcmin. The spectrometer aboard INTEGRAL is SPI (the SPectrometer for INTEGRAL), which observes radiation between 20 keV and 8 MeV. SPI uses a coded mask and has an energy resolution of 2 keV at 1 MeV, which is a record at these high energies. Dual JEM-X units provide additional information at lower energies on targets. They observe in soft and hard X-rays, from 3 to 35 keV. Aside from broadening the spectral coverage, imaging is more precise due to the shorter wavelength. Imaging capabilities are obtained again with the use of a coded mask. INTEGRAL also mounts an Optical Monitor (OMC), sensitive from 500 to 580 nm.

Bibliography

Alpar, M. A., Cheng, A. F., Ruderman, M. A., and Shaham, J. (1982). A new class of radio pulsars. Nature, 300:728–730.

Altamirano, D., Keek, L., Cumming, A., Sivakoff, G. R., Heinke, C. O., Wijnands, R., Degenaar, N., Homan, J., and Pooley, D. (2012). A superburst candidate in EXO 1745-248 as a challenge to thermonuclear ignition models. MNRAS, 426:927–934.

Altamirano, D., Krimm, H. A., Patruno, A., Bahramian, A., Heinke, C. O., Wijnands, R., and Degenaar, N. (2015). Swift/BAT detects an outburst from an X-ray transient in the globular cluster Terzan 5. *The Astronomer's Telegram*, 7240.

Archibald, A. M., Stairs, I. H., Ransom, S. M., et al. (2009). A Radio Pulsar/X-ray Binary Link. *Science*, 324:1411–.

Arnaud, K. A. (1996). XSPEC: The First Ten Years. In Jacoby, G. H. and Barnes, J., editors, *Astronomical Data Analysis Software and Systems V*, volume 101 of *Astronomical Society of the Pacific Conference Series*, page 17.

Bahramian, A., Heinke, C. O., Sivakoff, G. R., Altamirano, D., Wijnands, R., Homan, J., Linares, M., Pooley, D., Degenaar, N., and Gladstone, J. C. (2014). Discovery of the Third Transient X-Ray Binary in the Galactic Globular Cluster Terzan 5. ApJ, 780:127.

Ballantyne, D. R. (2004). Reflection spectra from an accretion disc illuminated by a neutron star X-ray burst. MNRAS, 351:57–62.

Balucinska, M. and Czerny, M. (1985). Variability of emitting area during bursts from Serpens X-1. Acta Astron., 35:291–303.

Barret, D. (2012). kHz Quasi-periodic Oscillations from the 2000 and 2010 X-Ray Transients Located in the Globular Cluster Terzan 5: EXO1745-248 and IGR J17480-2446. ApJ, 753:84.

Barret, D. and Olive, J.-F. (2002). A Peculiar Spectral State Transition of 4U 1705-44: When an Atoll Looks Like a Z. ApJ, 576:391–401.

Barret, D., Olive, J. F., Boirin, L., Done, C., Skinner, G. K., and Grindlay, J. E. (2000). Hard X-Ray Emission from Low-Mass X-Ray Binaries. ApJ, 533:329–351.

Barrio, F. E., Done, C., and Nayakshin, S. (2003). On the accretion geometry of Cyg X-1 in the low/hard state. MNRAS, 342:557–563.

Bassa, C. G., Patruno, A., Hessels, J. W. T., Keane, E. F., Monard, B., Mahony, E. K., Bogdanov, S., Corbel, S., Edwards, P. G., Archibald, A. M., Janssen, G. H., Stappers, B. W., and Tendulkar, S. (2014). A state change in the low-mass X-ray binary XSS J12270-4859. MNRAS, 441:1825–1830.

Beloborodov, A. M. (1999). Plasma Ejection from Magnetic Flares and the X-Ray Spectrum of Cygnus X-1. ApJ, 510:L123–L126.

Bhattacharyya, S. and Strohmayer, T. E. (2007). Evidence of a Broad Relativistic Iron Line from the Neutron Star Low-Mass X-Ray Binary Serpens X-1. ApJ, 664:L103–L106.

Boldt, E. and Leiter, D. (1987). Constraints on possible precursor AGN sources of the cosmic X-ray background. ApJ, 322:L1–L4.

Brenneman, L. W. and Reynolds, C. S. (2006). Constraining Black Hole Spin via X-Ray Spectroscopy. ApJ, 652:1028–1043.

Cackett, E. M., Altamirano, D., Patruno, A., Miller, J. M., Reynolds, M., Linares, M., and Wijnands, R. (2009a). Broad Relativistic Iron Emission Line Observed in SAX J1808.4-3658. ApJ, 694:L21–L25.

Cackett, E. M., Altamirano, D., Patruno, A., Miller, J. M., Reynolds, M., Linares, M., and Wijnands, R. (2009b). Broad Relativistic Iron Emission Line Observed in SAX J1808.4-3658. ApJ, 694:L21–L25.

Cackett, E. M. and Miller, J. M. (2013). Broad Iron Lines in Neutrons Stars: Dynamical Broadening or Wind Scattering? ApJ, 777:47.

Cackett, E. M., Miller, J. M., Ballantyne, D. R., Barret, D., Bhattacharyya, S., Boutelier, M., Miller, M. C., Strohmayer, T. E., and Wijnands, R. (2010). Relativistic Lines and Reflection from the Inner Accretion Disks Around Neutron Stars. ApJ, 720:205–225.

Cackett, E. M., Miller, J. M., Bhattacharyya, S., Grindlay, J. E., Homan, J., van der Klis, M., Miller, M. C., Strohmayer, T. E., and Wijnands, R. (2008). Relativistic Iron Emission Lines in Neutron Star Low-Mass X-Ray Binaries as Probes of Neutron Star Radii. ApJ, 674:415–420.

Cackett, E. M., Miller, J. M., Reis, R. C., Fabian, A. C., and Barret, D. (2012). A Comparison of Broad Iron Emission Lines in Archival Data of Neutron Star Low-mass X-Ray Binaries. ApJ, 755:27.

Chiang, C.-Y., Cackett, E. M., Miller, J. M., Barret, D., Fabian, A. C., D'Aì, A., Parker, M. L., Bhattacharyya, S., Burderi, L., Di Salvo, T., Egron, E., Homan, J., Iaria, R., Lin, D., and Miller, M. C. (2016a). A Test of the Nature of the Fe K Line in the Neutron Star Low-mass X-Ray Binary Serpens X-1. ApJ, 821:105.

Chiang, C.-Y., Cackett, E. M., Miller, J. M., Barret, D., Fabian, A. C., D'Aì, A., Parker, M. L., Bhattacharyya, S., Burderi, L., Di Salvo, T., Egron, E., Homan, J., Iaria, R., Lin, D., and Miller, M. C. (2016b). A Test of the Nature of the Fe K Line in the Neutron Star Low-mass X-Ray Binary Serpens X-1. ApJ, 821:105.

Churazov, E., Gilfanov, M., Sunyaev, R., Novickov, B., Chulkov, I., Kovtunenko, V., Sheikhet, A., Sukhanov, K., Goldwurm, A., Cordier, B., Paul, J., Ballet, J., Jourdain, E., Roques, J. P., Bouchet, L., and Mandrou, P. (1997). LMXBS and black hole candidates in the Galactic Center Region. *Advances in Space Research*, 19:55–61.

Church, M. J. and Balucińska-Church, M. (2001). Results of a LMXB survey: Variation in the height of the neutron star blackbody emission region. A&A, 369:915–924.

Cornelisse, R., Casares, J., Charles, P. A., and Steeghs, D. (2013). A 2 h periodic variation in the low-mass X-ray binary Ser X-1. MNRAS, 432:1361–1366.

Cornelisse, R., Kuulkers, E., in't Zand, J. J. M., Verbunt, F., and Heise, J. (2002). A four-hours long burst from Serpens X-1. A&A, 382:174–177.

Courvoisier, T. J.-L., Walter, R., Beckmann, V., Dean, A. J., Dubath, P., Hudec, R., Kretschmar, P., Mereghetti, S., Montmerle, T., Mowlavi, N., Paltani, S., Preite Martinez, A., Produit, N., Staubert, R., Strong, A. W., Swings, J.-P., Westergaard, N. J., White, N., Winkler, C., and Zdziarski, A. A. (2003). The INTEGRAL Science Data Centre (ISDC). A&A, 411:L53–L57.

Cumming, A., Zweibel, E., and Bildsten, L. (2001a). Magnetic Screening in Accreting Neutron Stars. ApJ, 557:958–966.

Cumming, A., Zweibel, E., and Bildsten, L. (2001b). Magnetic Screening in Accreting Neutron Stars. ApJ, 557:958–966.

D'Aì, A., di Salvo, T., Ballantyne, D., Iaria, R., Robba, N. R., Papitto, A., Riggio, A., Burderi, L., Piraino, S., Santangelo, A., Matt, G., Dovčiak, M., and Karas, V. (2010a). A self-consistent approach to the hard and soft states of 4U 1705-44. A&A, 516:A36.

D'Aì, A., di Salvo, T., Ballantyne, D., Iaria, R., Robba, N. R., Papitto, A., Riggio, A., Burderi, L., Piraino, S., Santangelo, A., Matt, G., Dovčiak, M., and Karas, V. (2010b). A self-consistent approach to the hard and soft states of 4U 1705-44. A&A, 516:A36.

D'Aì, A., Iaria, R., Di Salvo, T., Matt, G., and Robba, N. R. (2009a). Disk Reflection Signatures in the Spectrum of the Bright Z-Source GX 340+0. ApJ, 693:L1–L5.

D'Aì, A., Iaria, R., Di Salvo, T., Matt, G., and Robba, N. R. (2009b). Disk Reflection Signatures in the Spectrum of the Bright Z-Source GX 340+0. ApJ, 693:L1–L5.

Dauser, T., Wilms, J., Reynolds, C. S., and Brenneman, L. W. (2010). Broad emission lines for a negatively spinning black hole. MNRAS, 409:1534–1540.

Degenaar, N., Miller, J. M., Chakrabarty, D., Harrison, F. A., Kara, E., and Fabian, A. C. (2015). A NuSTAR observation of disc reflection from close to the neutron star in 4U 1608-52. MNRAS, 451:L85–L89.

Degenaar, N. and Wijnands, R. (2012). Strong X-ray variability in the quiescent state of the neutron star low-mass X-ray binary EXO 1745-248. MNRAS, 422:581–589.

Di Salvo, T., D'Aí, A., Iaria, R., Burderi, L., Dovčiak, M., Karas, V., Matt, G., Papitto, A., Piraino, S., Riggio, A., Robba, N. R., and Santangelo, A. (2009a). A relativistically smeared spectrum in the neutron star X-ray binary 4U 1705-44: looking at the inner accretion disc with X-ray spectroscopy. MNRAS, 398:2022–2027.

Di Salvo, T., D'Aí, A., Iaria, R., Burderi, L., Dovčiak, M., Karas, V., Matt, G., Papitto, A., Piraino, S., Riggio, A., Robba, N. R., and Santangelo, A. (2009b). A relativistically smeared spectrum in the neutron star X-ray binary 4U 1705-44: looking at the inner accretion disc with X-ray spectroscopy. MNRAS, 398:2022–2027.

di Salvo, T., D'Aí, A., Iaria, R., Burderi, L., Dovčiak, M., Karas, V., Matt, G., Papitto, A., Piraino, S., Riggio, A., Robba, N. R., and Santangelo, A. (2009). A relativistically smeared spectrum in the neutron star X-ray binary 4U 1705-44: looking at the inner accretion disc with X-ray spectroscopy. MNRAS, 398:2022–2027.

Di Salvo, T., Done, C., Życki, P. T., Burderi, L., and Robba, N. R. (2001a). Probing the Inner Region of Cygnus X-1 in the Low/Hard State through Its X-Ray Broadband Spectrum. ApJ, 547:1024–1033.

Di Salvo, T., Iaria, R., Matranga, M., Burderi, L., D'Aí, A., Egron, E., Papitto, A., Riggio, A., Robba, N. R., and Ueda, Y. (2015a). Suzaku broad-band spectrum of 4U 1705-44: probing the reflection component in the hard state. MNRAS, 449:2794–2802.

Di Salvo, T., Iaria, R., Matranga, M., Burderi, L., D'Aí, A., Egron, E., Papitto, A., Riggio, A., Robba, N. R., and Ueda, Y. (2015b). Suzaku broad-band spectrum of 4U 1705-44: probing the reflection component in the hard state. MNRAS, 449:2794–2802.

Di Salvo, T., Iaria, R., Méndez, M., Burderi, L., Lavagetto, G., Robba, N. R., Stella, L., and van der Klis, M. (2005a). A Broad Iron Line in the Chandra High Energy Transmission Grating Spectrum of 4U 1705-44. ApJ, 623:L121–L124.

Di Salvo, T., Iaria, R., Méndez, M., Burderi, L., Lavagetto, G., Robba, N. R., Stella, L., and van der Klis, M. (2005b). A Broad Iron Line in the Chandra High Energy Transmission Grating Spectrum of 4U 1705-44. ApJ, 623:L121–L124.

Di Salvo, T., Robba, N. R., Iaria, R., Stella, L., Burderi, L., and Israel, G. L. (2001b). Detection of a Hard Tail in the X-Ray Spectrum of the Z Source GX 349+2. ApJ, 554:49–55.

Di Salvo, T., Stella, L., Robba, N. R., van der Klis, M., Burderi, L., Israel, G. L., Homan, J., Campana, S., Frontera, F., and Parmar, A. N. (2000a). The Discovery of a State-Dependent Hard Tail in the X-Ray Spectrum of the Luminous Z Source GX 17+2. ApJ, 544:L119–L122.

Di Salvo, T., Stella, L., Robba, N. R., van der Klis, M., Burderi, L., Israel, G. L., Homan, J., Campana, S., Frontera, F., and Parmar, A. N. (2000b). The Discovery of a State-Dependent Hard Tail in the X-Ray Spectrum of the Luminous Z Source GX 17+2. ApJ, 544:L119–L122.

Dickey, J. M. and Lockman, F. J. (1990). H I in the Galaxy. ARA&A, 28:215–261.

Done, C. and Gierliński, M. (2006). Truncated disc versus extremely broad iron line in XTE J1650-500. MNRAS, 367:659–668.

Done, C., Gierliński, M., and Kubota, A. (2007). Modelling the behaviour of accretion flows in X-ray binaries. Everything you always wanted to know about accretion but were afraid to ask. *The Astronomy and Astrophysics Review*, 15:1–66.

Egron, E., di Salvo, T., Burderi, L., Papitto, A., Barragán, L., Dauser, T., Wilms, J., D'Aì, A., Riggio, A., Iaria, R., and Robba, N. R. (2011a). X-ray spectroscopy of MXB 1728-34 with XMM-Newton. A&A, 530:A99.

Egron, E., di Salvo, T., Burderi, L., Papitto, A., Barragán, L., Dauser, T., Wilms, J., D'Aì, A., Riggio, A., Iaria, R., and Robba, N. R. (2011b). X-ray spectroscopy of MXB 1728-34 with XMM-Newton. A&A, 530:A99.

Egron, E., Di Salvo, T., Motta, S., Burderi, L., Papitto, A., Duro, R., D'Aì, A., Riggio, A., Belloni, T., Iaria, R., Robba, N. R., Piraino, S., and Santangelo, A. (2013a). Testing reflection features in 4U 1705-44 with XMM-Newton, BeppoSAX, and RXTE in the hard and soft states. A&A, 550:A5.

Egron, E., Di Salvo, T., Motta, S., Burderi, L., Papitto, A., Duro, R., D'Aì, A., Riggio, A., Belloni, T., Iaria, R., Robba, N. R., Piraino, S., and Santangelo, A. (2013b). Testing reflection features in 4U 1705-44 with XMM-Newton, BeppoSAX, and RXTE in the hard and soft states. A&A, 550:A5.

Esin, A. A., McClintock, J. E., and Narayan, R. (1997). Advection-Dominated Accretion and the Spectral States of Black Hole X-Ray Binaries: Application to Nova Muscae 1991. ApJ, 489:865–889.

Evans, P. A., Beardmore, A. P., Page, K. L., Osborne, J. P., O'Brien, P. T., Willingale, R., Starling, R. L. C., Burrows, D. N., Godet, O., Vetere, L., Racusin, J., Goad, M. R., Wiersema, K., Angelini, L., Capalbi, M., Chincarini, G., Gehrels, N., Kennea, J. A., Margutti, R., Morris, D. C., Mountford, C. J., Pagani, C., Perri, M., Romano, P., and Tanvir, N. (2009). Methods and results

of an automatic analysis of a complete sample of Swift-XRT observations of GRBs. MNRAS, 397:1177–1201.

Fabian, A. C., Iwasawa, K., Reynolds, C. S., and Young, A. J. (2000). Broad Iron Lines in Active Galactic Nuclei. PASP, 112:1145–1161.

Fabian, A. C., Rees, M. J., Stella, L., and White, N. E. (1989). X-ray fluorescence from the inner disc in Cygnus X-1. MNRAS, 238:729–736.

Ferraro, F. R., Dalessandro, E., Mucciarelli, A., Beccari, G., Rich, R. M., Origlia, L., Lanzoni, B., Rood, R. T., Valenti, E., Bellazzini, M., Ransom, S. M., and Cocozza, G. (2009). The cluster Terzan 5 as a remnant of a primordial building block of the Galactic bulge. Nature, 462:483–486.

Ferraro, F. R., Massari, D., Dalessandro, E., Lanzoni, B., Origlia, L., Rich, R. M., and Mucciarelli, A. (2016). The age of the young bulge-like population in the stellar system Terzan 5: linking the Galactic bulge to the high-z Universe. ApJ.

Ferraro, F. R., Pallanca, C., Lanzoni, B., Cadelano, M., Massari, D., Dalessandro, E., and Mucciarelli, A. (2015). Probing the MSP Prenatal Stage: The Optical Identification of the X-Ray Burster EXO 1745-248 in Terzan 5. ApJ, 807:L1.

Ferrigno, C., Bozzo, E., Papitto, A., Rea, N., Pavan, L., Campana, S., Wieringa, M., Filipović, M., Falanga, M., and Stella, L. (2014). Hiccup accretion in the swinging pulsar IGR J18245-2452. A&A, 567:A77.

Fiocchi, M., Bazzano, A., Ubertini, P., and Zdziarski, A. A. (2007). The First Detection of Compton Reflection in the Low-Mass X-Ray Binary 4U 1705-44 with INTEGRAL and BeppoSax. ApJ, 657:448–452.

Friedman, H., Byram, E. T., and Chubb, T. A. (1967). Distribution and Variability of Cosmic X-Ray Sources. *Science*, 156:374–378.

Galloway, D. K., Muno, M. P., Hartman, J. M., Psaltis, D., and Chakrabarty, D. (2008). Thermonuclear (Type I) X-Ray Bursts Observed by the Rossi X-Ray Timing Explorer. ApJS, 179:360–422.

García, J., Dauser, T., Lohfink, A., Kallman, T. R., Steiner, J. F., McClintock, J. E., Brenneman, L., Wilms, J., Eikmann, W., Reynolds, C. S., and Tombesi, F. (2014). Improved Reflection Models of Black Hole Accretion Disks: Treating the Angular Distribution of X-Rays. ApJ, 782:76.

García, J., Dauser, T., Reynolds, C. S., Kallman, T. R., McClintock, J. E., Wilms, J., and Eikmann, W. (2013). X-Ray Reflected Spectra from Accretion Disk Models. III. A Complete Grid of Ionized Reflection Calculations. ApJ, 768:146.

García, J. and Kallman, T. R. (2010). X-ray Reflected Spectra from Accretion Disk Models. I. Constant Density Atmospheres. ApJ, 718:695–706.

Geppert, U. and Urpin, V. (1994). Accretion-driven magnetic field decay in neutron stars. MNRAS, 271.

Harrison, F. A., Craig, W. W., Christensen, F. E., Hailey, C. J., Zhang, W. W., Boggs, S. E., Stern, D., Cook, W. R., Forster, K., Giommi, P., Grefenstette, B. W., Kim, Y., Kitaguchi, T., Koglin, J. E., Madsen, K. K., Mao, P. H., Miyasaka, H., Mori, K., Perri, M., Pivovaroff, M. J., Puccetti, S., Rana, V. R., Westergaard, N. J., Willis, J., Zoglauer, A., An, H., Bachetti, M., Barrière, N. M., Bellm, E. C., Bhalerao, V., Brejnholt, N. F., Fuerst, F., Liebe, C. C., Markwardt, C. B., Nynka, M., Vogel, J. K., Walton, D. J., Wik, D. R., Alexander, D. M., Cominsky, L. R., Hornschemeier, A. E., Hornstrup, A., Kaspi, V. M., Madejski, G. M., Matt, G., Molendi, S., Smith, D. M., Tomsick, J. A., Ajello, M., Ballantyne, D. R., Baloković, M., Barret, D., Bauer, F. E., Blandford, R. D., Brandt, W. N., Brenneman, L. W., Chiang, J., Chakrabarty, D., Chenevez, J., Comastri, A., Dufour, F., Elvis, M., Fabian, A. C., Farrah, D., Fryer, C. L., Gotthelf, E. V., Grindlay, J. E., Helfand, D. J., Krivonos, R., Meier, D. L., Miller, J. M., Natalucci, L., Ogle, P., Ofek, E. O., Ptak, A., Reynolds, S. P., Rigby, J. R., Tagliaferri, G., Thorsett, S. E., Treister, E., and Urry, C. M. (2013). The Nuclear Spectroscopic Telescope Array (NuSTAR) High-energy X-Ray Mission. ApJ, 770:103.

Hasinger, G. and van der Klis, M. (1989a). Two patterns of correlated X-ray timing and spectral behaviour in low-mass X-ray binaries. A&A, 225:79–96.

Hasinger, G. and van der Klis, M. (1989b). Two patterns of correlated X-ray timing and spectral behaviour in low-mass X-ray binaries. A&A, 225:79–96.

Hasinger, G., van der Klis, M., Ebisawa, K., Dotani, T., and Mitsuda, K. (1990). Multifrequency observations of Cygnus X-2 - X-ray observations with GINGA. A&A, 235:131–146.

Heinke, C. O., Edmonds, P. D., Grindlay, J. E., Lloyd, D. A., Cohn, H. N., and Lugger, P. M. (2003a). A Chandra X-Ray Study of the Dense Globular Cluster Terzan 5. ApJ, 590:809–821.

Heinke, C. O., Grindlay, J. E., Lugger, P. M., Cohn, H. N., Edmonds, P. D., Lloyd, D. A., and Cool, A. M. (2003b). Analysis of the Quiescent Low-Mass X-Ray Binary Population in Galactic Globular Clusters. ApJ, 598:501–515.

Heinke, C. O., Wijnands, R., Cohn, H. N., Lugger, P. M., Grindlay, J. E., Pooley, D., and Lewin, W. H. G. (2006). Faint X-Ray Sources in the Globular Cluster Terzan 5. ApJ, 651:1098–1111.

Heitler, W. (1954). *Quantum theory of radiation.*

Herold, H. (1979). Compton and Thomson scattering in strong magnetic fields. Phys. Rev. D, 19:2868–2875.

Hessels, J. W. T., Ransom, S. M., Stairs, I. H., Freire, P. C. C., Kaspi, V. M., and Camilo, F. (2006). A Radio Pulsar Spinning at 716 Hz. *Science*, 311:1901–1904.

Iaria, R., Burderi, L., Di Salvo, T., La Barbera, A., and Robba, N. R. (2001). A Hard Tail in the X-Ray Broadband Spectrum of Circinus X-1 at the Periastron: A Peculiar Z Source. ApJ, 547:412–419.

Iaria, R., D'Aí, A., di Salvo, T., Robba, N. R., Riggio, A., Papitto, A., and Burderi, L. (2009). A ionized reflecting skin above the accretion disk of GX 349+2. A&A, 505:1143–1151.

Iaria, R., Di Salvo, T., Robba, N. R., and Burderi, L. (2002). Study of the Circinus X-1 Broadband Spectrum at Orbital Phases Close to the Apoastron. ApJ, 567:503–509.

in 't Zand, J. J. M., Verbunt, F., Strohmayer, T. E., Bazzano, A., Cocchi, M., Heise, J., van Kerkwijk, M. H., Muller, J. M., Natalucci, L., Smith, M. J. S., and Ubertini, P. (1999). A new X-ray outburst in the globular cluster NGC 6440: SAX J1748.9-2021. A&A, 345:100–108.

Jansen, F., Lumb, D., Altieri, B., Clavel, J., Ehle, M., Erd, C., Gabriel, C., Guainazzi, M., Gondoin, P., Much, R., Munoz, R., Santos, M., Schartel, N., Texier, D., and Vacanti, G. (2001). XMM-Newton observatory. I. The spacecraft and operations. A&A, 365:L1–L6.

Johnston, H. M. and Kulkarni, S. R. (1991). On the detectability of pulsars in close binary systems. ApJ, 368:504–514.

Kalogera, V. and Baym, G. (1996). The Maximum Mass of a Neutron Star. ApJ, 470:L61.

King, A. L., Tomsick, J. A., Miller, J. M., Chenevez, J., Barret, D., Boggs, S. E., Chakrabarty, D., Christensen, F. E., Craig, W. W., Fürst, F., Hailey, C. J., Harrison, F. A., Parker, M. L., Stern, D., Romano, P., Walton, D. J., and Zhang, W. W. (2016). Measuring a Truncated Disk in Aquila X-1. ApJ, 819:L29.

Kippenhahn, R. and Weigert, A. (1990). *Stellar Structure and Evolution*.

Kluzniak, W. (1993). Mechanisms of hard X-ray emission from accreting neutron stars. A&AS, 97:265–267.

Kolehmainen, M., Done, C., and Díaz Trigo, M. (2011a). Modelling the high-mass accretion rate spectra of GX 339-4: black hole spin from reflection? MNRAS, 416:311–321.

Kolehmainen, M., Done, C., and Díaz Trigo, M. (2011b). Modelling the high-mass accretion rate spectra of GX 339-4: black hole spin from reflection? MNRAS, 416:311–321.

Konar, S. and Bhattacharya, D. (1997). Magnetic field evolution of accreting neutron stars. MNRAS, 284:311–317.

Koyama, K., Tsunemi, H., Dotani, T., Bautz, M. W., Hayashida, K., and et al. (2007). X-Ray Imaging Spectrometer (XIS) on Board Suzaku. PASJ, 59:23–33.

Kuulkers, E., den Hartog, P. R., in't Zand, J. J. M., Verbunt, F. W. M., Harris, W. E., and Cocchi, M. (2003). Photospheric radius expansion X-ray bursts as standard candles. A&A, 399:663–680.

Laor, A. (1991). Line profiles from a disk around a rotating black hole. ApJ, 376:90–94.

Lebrun, F., Leray, J. P., Lavocat, P., Crétolle, J., Arquès, M., Blondel, C., Bonnin, C., Bouère, A., Cara, C., Chaleil, T., Daly, F., Desages, F., Dzitko, H., Horeau, B., Laurent, P., Limousin, O., Mathy, F., Mauguen, V., Meignier, F., Molinié, F., Poindron, E., Rouger, M., Sauvageon, A., and Tourrette, T.

(2003). ISGRI: The INTEGRAL Soft Gamma-Ray Imager. A&A, 411:L141–L148.

Lewin, W. H. G. and Joss, P. C. (1983). X-Ray Bursters and the X-Ray Sources of the Galactic Bulge. In Lewin, W. H. G. and van den Heuvel, E. P. J., editors, *Accretion-Driven Stellar X-ray Sources*, page 41.

Li, F., Lewin, W. H. G., and Doxsey, R. (1976). X-Ray Bursts. IAU Circ., 2983.

Lightman, A. P. and Zdziarski, A. A. (1987). Pair production and Compton scattering in compact sources and comparison to observations of active galactic nuclei. ApJ, 319:643–661.

Lin, D., Remillard, R. A., and Homan, J. (2010). Suzaku and BeppoSAX X-ray Spectra of the Persistently Accreting Neutron-star Binary 4U 1705-44. ApJ, 719:1350–1361.

Lin, D. N. C. and Papaloizou, J. (1979). On the structure of circumbinary accretion disks and the tidal evolution of commensurable satellites. MNRAS, 188:191–201.

Linares, M., Chakrabarty, D., Marshall, H., Bahramian, A., Heinke, C., Sivakoff, G., Patruno, D. A. A., Wijnands, R., Degenaar, N., and Sanna, A. (2015). Swift refined location points to the neutron star transient EXO 1745-248 as the source currently active in Terzan 5. *The Astronomer's Telegram*, 7247.

Ludlam, R. M., Miller, J. M., Cackett, E. M., Fabian, A. C., Bachetti, M., Parker, M. L., Tomsick, J. A., Barret, D., Natalucci, L., Rana, V., and Harrison, F. A. (2016). NuSTAR and XMM-Newton Observations of the Neutron Star X-Ray Binary 1RXS J180408.9-34205. ApJ, 824:37.

Lund, N., Budtz-Jørgensen, C., Westergaard, N. J., Brandt, S., Rasmussen, I. L., Hornstrup, A., Oxborrow, C. A., Chenevez, J., Jensen, P. A., Laursen, S., Andersen, K. H., Mogensen, P. B., Rasmussen, I., Omø, K., Pedersen, S. M., Polny, J., Andersson, H., Andersson, T., Kämäräinen, V., Vilhu, O., Huovelin, J., Maisala, S., Morawski, M., Juchnikowski, G., Costa, E., Feroci, M., Rubini, A., Rapisarda, M., Morelli, E., Carassiti, V., Frontera, F., Pelliciari, C., Loffredo, G., Martínez Núñez, S., Reglero, V., Velasco, T., Larsson, S., Svensson, R., Zdziarski, A. A., Castro-Tirado, A., Attina, P., Goria, M., Giulianelli, G., Cordero, F., Rezazad, M., Schmidt, M., Carli, R., Gomez, C., Jensen,

P. L., Sarri, G., Tiemon, A., Orr, A., Much, R., Kretschmar, P., and Schnopper, H. W. (2003). JEM-X: The X-ray monitor aboard INTEGRAL. A&A, 411:L231–L238.

Magdziarz, P. and Zdziarski, A. A. (1995). Angle-dependent Compton reflection of X-rays and gamma-rays. MNRAS, 273:837–848.

Makishima, K., Ohashi, T., Inoue, H., Koyama, K., Matsuoka, M., Murakami, T., Oda, M., Ogawara, Y., Shibazaki, N., Tanaka, Y., Kondo, I., Hayakawa, S., Kunieda, H., Makino, F., Masai, K., Nagase, F., Tawara, Y., Miyamoto, S., Tsunemi, H., and da Yamashita, K. (1981). Discovery of two new X-ray burst sources in the globular clusters Terzan 1 and Terzan 5. ApJ, 247:L23–L25.

Markoff, S., Nowak, M. A., and Wilms, J. (2005). Going with the Flow: Can the Base of Jets Subsume the Role of Compact Accretion Disk Coronae? ApJ, 635:1203–1216.

Markwardt, C. B. and Swank, J. H. (2000). EXO 1745-248 = Xb 1745-25. IAU Circ., 7454.

Masetti, N., Frontera, F., Stella, L., Orlandini, M., Parmar, A. N., Del Sordo, S., Amati, L., Palazzi, E., Dal Fiume, D., Cusumano, G., Pareschi, G., Lapidus, I., and Remillard, R. A. (2000). Hard X-rays from Type II bursts of the Rapid Burster and its transition toward quiescence. A&A, 363:188–197.

Matt, G., Perola, G. C., Piro, L., and Stella, L. (1992). Iron K-alpha line from X-ray illuminated relativistic disks. A&A, 257:63–68.

Merloni, A., Fabian, A. C., and Ross, R. R. (2000). On the interpretation of the multicolour disc model for black hole candidates. MNRAS, 313:193–197.

Meylan, G. and Heggie, D. C. (1997). Internal dynamics of globular clusters. A&A Rev., 8:1–143.

Miller, J. M., D'Aì, A., Bautz, M. W., Bhattacharyya, S., Burrows, D. N., Cackett, E. M., Fabian, A. C., Freyberg, M. J., Haberl, F., Kennea, J., Nowak, M. A., Reis, R. C., Strohmayer, T. E., and Tsujimoto, M. (2010). On Relativistic Disk Spectroscopy in Compact Objects with X-ray CCD Cameras. ApJ, 724:1441–1455.

Miller, J. M., Parker, M. L., Fuerst, F., Bachetti, M., Barret, D., and et al. (2013). Constraints on the Neutron Star and Inner Accretion Flow in Serpens X-1 Using NuSTAR. ApJ, 779:L2.

Mitsuda, K., Bautz, M., Inoue, H., Kelley, R. L., Koyama, K., Kunieda, H., Makishima, K., Ogawara, Y., Petre, R., Takahashi, T., Tsunemi, H., White, N. E., Anabuki, N., Angelini, L., Arnaud, K., Awaki, H., Bamba, A., Boyce, K., Brown, G. V., Chan, K.-W., Cottam, J., Dotani, T., Doty, J., Ebisawa, K., Ezoe, Y., Fabian, A. C., Figueroa, E., Fujimoto, R., Fukazawa, Y., Furusho, T., Furuzawa, A., Gendreau, K., Griffiths, R. E., Haba, Y., Hamaguchi, K., Harrus, I., Hasinger, G., Hatsukade, I., Hayashida, K., Henry, P. J., Hiraga, J. S., Holt, S. S., Hornschemeier, A., Hughes, J. P., Hwang, U., Ishida, M., Ishisaki, Y., Isobe, N., Itoh, M., Iyomoto, N., Kahn, S. M., Kamae, T., Katagiri, H., Kataoka, J., Katayama, H., Kawai, N., Kilbourne, C., Kinugasa, K., Kissel, S., Kitamoto, S., Kohama, M., Kohmura, T., Kokubun, M., Kotani, T., Kotoku, J., Kubota, A., Madejski, G. M., Maeda, Y., Makino, F., Markowitz, A., Matsumoto, C., Matsumoto, H., Matsuoka, M., Matsushita, K., McCammon, D., Mihara, T., Misaki, K., Miyata, E., Mizuno, T., Mori, K., Mori, H., Morii, M., Moseley, H., Mukai, K., Murakami, H., Murakami, T., Mushotzky, R., Nagase, F., Namiki, M., Negoro, H., Nakazawa, K., Nousek, J. A., Okajima, T., Ogasaka, Y., Ohashi, T., Oshima, T., Ota, N., Ozaki, M., Ozawa, H., Parmar, A. N., Pence, W. D., Porter, F. S., Reeves, J. N., Ricker, G. R., Sakurai, I., Sanders, W. T., Senda, A., Serlemitsos, P., Shibata, R., Soong, Y., Smith, R., Suzuki, M., Szymkowiak, A. E., Takahashi, H., Tamagawa, T., Tamura, K., Tamura, T., Tanaka, Y., Tashiro, M., Tawara, Y., Terada, Y., Terashima, Y., Tomida, H., Torii, K., Tsuboi, Y., Tsujimoto, M., Tsuru, T. G., Turner, M. J. L. ., Ueda, Y., Ueno, S., Ueno, M., Uno, S., Urata, Y., Watanabe, S., Yamamoto, N., Yamaoka, K., Yamasaki, N. Y., Yamashita, K., Yamauchi, M., Yamauchi, S., Yaqoob, T., Yonetoku, D., and Yoshida, A. (2007). The X-Ray Observatory Suzaku. PASJ, 59:S1–S7.

Motta, S., D'Aı, A., Papitto, A., Riggio, A., di Salvo, T., Burderi, L., Belloni, T., Stella, L., and Iaria, R. (2011). X-ray bursts and burst oscillations from the slowly spinning X-ray pulsar IGR J17480-2446 (Terzan 5). MNRAS, 414:1508–1516.

Mukherjee, A. and Bhattacharyya, S. (2011). Highly Coherent Kilohertz Quasi-periodic Oscillations from the Neutron Star X-ray Binary EXO 1745-248. ApJ, 730:L32.

Ng, C., Díaz Trigo, M., Cadolle Bel, M., and Migliari, S. (2010). A systematic analysis of the broad iron Kα line in neutron-star LMXBs with XMM-Newton. A&A, 522:A96.

Olive, J.-F., Barret, D., and Gierliński, M. (2003). Correlated Timing and Spectral Behavior of 4U 1705-44. ApJ, 583:416–423.

Oosterbroek, T., Barret, D., Guainazzi, M., and Ford, E. C. (2001). Simultaneous BeppoSAX and RXTE observations of the X-ray burst sources GX 3+1 and Ser X-1. A&A, 366:138–145.

Origlia, L., Massari, D., Rich, R. M., Mucciarelli, A., Ferraro, F. R., Dalessandro, E., and Lanzoni, B. (2013). The Terzan 5 Puzzle: Discovery of a Third, Metal-poor Component. ApJ, 779:L5.

Ortolani, S., Barbuy, B., Bica, E., Zoccali, M., and Renzini, A. (2007). Distances of the bulge globular clusters Terzan 5, Liller 1, UKS 1, and Terzan 4 based on HST NICMOS photometry. A&A, 470:1043–1049.

Özel, F., Güver, T., and Psaltis, D. (2009). The Mass and Radius of the Neutron Star in EXO 1745-248. ApJ, 693:1775–1779.

Palmeri, P., Mendoza, C., Kallman, T. R., Bautista, M. A., and Meléndez, M. (2003). Modeling of iron K lines: Radiative and Auger decay data for Fe II-Fe IX. A&A, 410:359–364.

Pandel, D., Kaaret, P., and Corbel, S. (2008a). Relativistic Iron Line Emission from the Neutron Star Low-mass X-Ray Binary 4U 1636-536. ApJ, 688:1288–1294.

Pandel, D., Kaaret, P., and Corbel, S. (2008b). Relativistic Iron Line Emission from the Neutron Star Low-mass X-Ray Binary 4U 1636-536. ApJ, 688:1288–1294.

Pandel, D., Kaaret, P., and Corbel, S. (2008c). Relativistic Iron Line Emission from the Neutron Star Low-Mass X-Ray Binary 4U 1636-536. ApJ, 688:1288–1294.

Papaloizou, J. and Pringle, J. E. (1977). Tidal torques on accretion discs in close binary systems. MNRAS, 181:441–454.

Papitto, A., D'Aì, A., Di Salvo, T., Egron, E., Bozzo, E., Burderi, L., Iaria, R., Riggio, A., and Menna, M. T. (2013a). The accretion flow to the intermittent accreting millisecond pulsar, HETE J1900.1-2455, as observed by XMM-Newton and RXTE. MNRAS, 429:3411–3422.

Papitto, A., D'Aì, A., Di Salvo, T., Egron, E., Bozzo, E., Burderi, L., Iaria, R., Riggio, A., and Menna, M. T. (2013b). The accretion flow to the intermittent accreting millisecond pulsar, HETE J1900.1-2455, as observed by XMM-Newton and RXTE. MNRAS, 429:3411–3422.

Papitto, A., D'Aì, A., Motta, S., Riggio, A., Burderi, L., di Salvo, T., Belloni, T., and Iaria, R. (2011). The spin and orbit of the newly discovered pulsar IGR J17480-2446. A&A, 526:L3.

Papitto, A., Di Salvo, T., Burderi, L., Belloni, T. M., Stella, L., Bozzo, E., D'Aì, A., Ferrigno, C., Iaria, R., Motta, S., Riggio, A., and Tramacere, A. (2012). The pulse profile and spin evolution of the accreting pulsar in Terzan 5, IGR J17480-2446, during its 2010 outburst. MNRAS, 423:1178–1193.

Papitto, A., Di Salvo, T., D'Aì, A., Iaria, R., Burderi, L., Riggio, A., Menna, M. T., and Robba, N. R. (2009a). XMM-Newton detects a relativistically broadened iron line in the spectrum of the ms X-ray pulsar SAX J1808.4-3658. A&A, 493:L39–L43.

Papitto, A., Di Salvo, T., D'Aì, A., Iaria, R., Burderi, L., Riggio, A., Menna, M. T., and Robba, N. R. (2009b). XMM-Newton detects a relativistically broadened iron line in the spectrum of the ms X-ray pulsar SAX J1808.4-3658. A&A, 493:L39–L43.

Papitto, A., Ferrigno, C., Bozzo, E., Rea, N., Pavan, L., Burderi, L., Burgay, M., Campana, S., di Salvo, T., Falanga, M., Filipović, M. D., Freire, P. C. C., Hessels, J. W. T., Possenti, A., Ransom, S. M., Riggio, A., Romano, P., Sarkissian, J. M., Stairs, I. H., Stella, L., Torres, D. F., Wieringa, M. H., and Wong, G. F. (2013c). Swings between rotation and accretion power in a binary millisecond pulsar. Nature, 501:517–520.

Papitto, A., Riggio, A., di Salvo, T., Burderi, L., D'Aì, A., Iaria, R., Bozzo, E., and Menna, M. T. (2010a). The X-ray spectrum of the newly discovered accreting millisecond pulsar IGR J17511-3057. MNRAS, 407:2575–2588.

Papitto, A., Riggio, A., di Salvo, T., Burderi, L., D'Aì, A., Iaria, R., Bozzo, E., and Menna, M. T. (2010b). The X-ray spectrum of the newly discovered accreting millisecond pulsar IGR J17511-3057. MNRAS, 407:2575–2588.

Patruno, A., Alpar, M. A., van der Klis, M., and van den Heuvel, E. P. J. (2012). The Peculiar Evolutionary History of IGR J17480-2446 in Terzan 5. ApJ, 752:33.

Patruno, A. and Watts, A. L. (2012). Accreting Millisecond X-Ray Pulsars. *ArXiv e-prints*.

Peterson, L. E. and Jacobson, A. S. (1966). The Spectrum of Scorpius XR-1 to 50 KEV. ApJ, 145:962.

Pintore, F., Di Salvo, T., Bozzo, E., Sanna, A., Burderi, L., D'Aì, A., Riggio, A., Scarano, F., and Iaria, R. (2015a). Study of the reflection spectrum of the accreting neutron star GX 3+1 using XMM-Newton and INTEGRAL. MNRAS, 450:2016–2024.

Pintore, F., Di Salvo, T., Bozzo, E., Sanna, A., Burderi, L., D'Aì, A., Riggio, A., Scarano, F., and Iaria, R. (2015b). Study of the reflection spectrum of the accreting neutron star GX 3+1 using XMM-Newton and INTEGRAL. MNRAS, 450:2016–2024.

Pintore, F., Sanna, A., Di Salvo, T., Del Santo, M., Riggio, A., D'Aì, A., Burderi, L., Scarano, F., and Iaria, R. (2016a). Broad-band spectral analysis of the accreting millisecond X-ray pulsar SAX J1748.9-2021. MNRAS, 457:2988–2998.

Pintore, F., Sanna, A., Di Salvo, T., Del Santo, M., Riggio, A., D'Aì, A., Burderi, L., Scarano, F., and Iaria, R. (2016b). Broad-band spectral analysis of the accreting millisecond X-ray pulsar SAX J1748.9-2021. MNRAS, 457:2988–2998.

Pintore, F., Sanna, A., Di Salvo, T., Guainazzi, M., D'Aì, A., Riggio, A., Burderi, L., Iaria, R., and Robba, N. R. (2014). Testing rate-dependent corrections on timing mode EPIC-pn spectra of the accreting neutron star GX 13+1. MNRAS, 445:3745–3754.

Piraino, S., Santangelo, A., di Salvo, T., Kaaret, P., Horns, D., Iaria, R., and Burderi, L. (2007). BeppoSAX observation of 4U 1705-44: detection of hard X-ray emission in the soft state. A&A, 471:L17–L20.

Piraino, S., Santangelo, A., Ford, E. C., and Kaaret, P. (1999). BeppoSAX observations of the atoll X-ray binary 4U 0614+091. A&A, 349:L77–L81.

Piraino, S., Santangelo, A., Kaaret, P., Mück, B., D'Aì, A., Di Salvo, T., Iaria, R., Robba, N., Burderi, L., and Egron, E. (2012). A relativistic iron emission line from the neutron star low-mass X-ray binary GX 3+1. A&A, 542:L27.

Pols, O. R., Schröder, K.-P., Hurley, J. R., Tout, C. A., and Eggleton, P. P. (1998). Stellar evolution models for Z = 0.0001 to 0.03. MNRAS, 298:525–536.

Pols, O. R., Tout, C. A., Eggleton, P. P., and Han, Z. (1995). Approximate input physics for stellar modelling. MNRAS, 274:964–974.

Pringle, J. E. and Rees, M. J. (1972). Accretion Disc Models for Compact X-Ray Sources. A&A, 21:1.

Ransom, S. M., Hessels, J. W. T., Stairs, I. H., Freire, P. C. C., Camilo, F., Kaspi, V. M., and Kaplan, D. L. (2005). Twenty-One Millisecond Pulsars in Terzan 5 Using the Green Bank Telescope. *Science*, 307:892–896.

Reis, R. C., Fabian, A. C., and Miller, J. M. (2010). Black hole accretion discs in the canonical low-hard state. MNRAS, 402:836–854.

Reis, R. C., Fabian, A. C., and Young, A. J. (2009). Relativistically broadened iron line in the Suzaku observation of the neutron star X-ray binary 4U 1705-44. MNRAS, 399:L1–L5.

Ross, R. R. and Fabian, A. C. (2005a). A comprehensive range of X-ray ionized-reflection models. MNRAS, 358:211–216.

Ross, R. R. and Fabian, A. C. (2005b). A comprehensive range of X-ray ionized-reflection models. MNRAS, 358:211–216.

Ross, R. R., Fabian, A. C., and Young, A. J. (1999). X-ray reflection spectra from ionized slabs. MNRAS, 306:461–466.

Sanna, A., Hiemstra, B., Méndez, M., Altamirano, D., Belloni, T., and Linares, M. (2013). Broad iron line in the fast spinning neutron-star system 4U 1636-53. MNRAS, 432:1144–1161.

Serino, M., Mihara, T., Matsuoka, M., Nakahira, S., Sugizaki, M., Ueda, Y., Kawai, N., and Ueno, S. (2012a). Superburst with Outburst from EXO 1745-248 in Terzan 5 with MAXI. PASJ, 64.

Serino, M., Mihara, T., Matsuoka, M., Nakahira, S., Sugizaki, M., Ueda, Y., Kawai, N., and Ueno, S. (2012b). Superburst with Outburst from EXO 1745-248 in Terzan 5 with MAXI. PASJ, 64.

Shakura, N. I. and Sunyaev, R. A. (1973). Black holes in binary systems. Observational appearance. A&A, 24:337–355.

Shaposhnikov, N., Titarchuk, L., and Laurent, P. (2009). Discovery of Red-skewed K Iron Line in Cyg X-2 with Suzaku. ApJ, 699:1223–1228.

Sunyaev, R. A. and Titarchuk, L. (1989). X ray burster spectra in the state of the persistent flux level. Two temperature models of the neutron star atmosphere. In Hunt, J. and Battrick, B., editors, *Two Topics in X-Ray Astronomy, Volume 1: X Ray Binaries. Volume 2: AGN and the X Ray Background*, volume 296 of *ESA Special Publication*.

Taam, R. E. and van den Heuvel, E. P. J. (1986). Magnetic field decay and the origin of neutron star binaries. ApJ, 305:235–245.

Takahashi, T., Abe, K., Endo, M., Endo, Y., Ezoe, Y., and et al. (2007). Hard X-Ray Detector (HXD) on Board Suzaku. PASJ, 59:35–51.

Tauris, T. M. and van den Heuvel, E. P. J. (2006). *Formation and evolution of compact stellar X-ray sources*, pages 623–665.

Tavani, M., Mukherjee, R., Mattox, J. R., Halpern, J., Thompson, D. J., Kanbach, G., Hermsen, W., Zhang, S. N., and Foster, R. S. (1997). Discovery of a non-blazar gamma-ray transient in the Galactic plane. In Dermer, C. D., Strickman, M. S., and Kurfess, J. D., editors, *Proceedings of the Fourth Compton Symposium*, volume 410 of *American Institute of Physics Conference Series*, pages 1253–1256.

Testa, V., di Salvo, T., D'Antona, F., Menna, M. T., Ventura, P., Burderi, L., Riggio, A., Iaria, R., D'Aì, A., Papitto, A., and Robba, N. (2012). The near-IR counterpart of IGR J17480-2446 in Terzan 5. A&A, 547:A28.

Tetarenko, A. J., Bahramian, A., Sivakoff, G. R., Tremou, E., Linares, M., Tudor, V., Miller-Jones, J. C. A., Heinke, C. O., Chomiuk, L., Strader, J., Altamirano, D., Degenaar, N., Maccarone, T., Patruno, A., Sanna, A., and Wijnands, R. (2016). Disc-Jet Coupling in the Terzan 5 Neutron Star X-ray Binary EXO 1745-248. MNRAS.

Titarchuk, L., Mastichiadis, A., and Kylafis, N. D. (1997). X-Ray Spectral Formation in a Converging Fluid Flow: Spherical Accretion into Black Holes. ApJ, 487:834–846.

Titarchuk, L. and Zannias, T. (1998). The Extended Power Law as an Intrinsic Signature for a Black Hole. ApJ, 493:863–872.

Tomsick, J. A., Yamaoka, K., Corbel, S., Kaaret, P., Kalemci, E., and Migliari, S. (2009). Truncation of the Inner Accretion Disk Around a Black Hole at Low Luminosity. ApJ, 707:L87–L91.

Tremou, E., Sivakoff, G., Bahramian, A., Heinke, C., Tetarenko, A., Wijnands, R., Degenaar, N., Linares, M., Miller-Jones, J., Patruno, A., Chomiuk, L., Strader, J., Altamirano, D., Maccarone, T., and Sanna, A. (2015). VLA observations identify the currently active source in Terzan 5 as the neutron star transient EXO 1745-248. *The Astronomer's Telegram*, 7262.

Ubertini, P., Lebrun, F., Di Cocco, G., Bazzano, A., Bird, A. J., Broenstad, K., Goldwurm, A., La Rosa, G., Labanti, C., Laurent, P., Mirabel, I. F., Quadrini, E. M., Ramsey, B., Reglero, V., Sabau, L., Sacco, B., Staubert, R., Vigroux, L., Weisskopf, M. C., and Zdziarski, A. A. (2003). IBIS: The Imager on-board INTEGRAL. A&A, 411:L131–L139.

Valenti, E., Ferraro, F. R., and Origlia, L. (2007). Near-Infrared Properties of 24 Globular Clusters in the Galactic Bulge. AJ, 133:1287–1301.

van der Klis, M. (2000). Millisecond Oscillations in X-ray Binaries. ARA&A, 38:717–760.

van der Klis, M. (2006). Overview of QPOs in neutron-star low-mass X-ray binaries. *Advances in Space Research*, 38:2675–2679.

van Paradijs, J., Penninx, W., and Lewin, W. H. G. (1988). On the relation between X-ray burst properties and the persistent X-ray luminosity. MNRAS, 233:437–450.

van Paradijs, J. and van der Klis, M. (1994). Luminosity dependence of the hardness of the 13-80 keV X-ray spectra of low-mass X-ray binaries. A&A, 281:L17–L20.

Vaughan, B. A., van der Klis, M., Wood, K. S., Norris, J. P., Hertz, P., Michelson, P. F., van Paradijs, J., Lewin, W. H. G., Mitsuda, K., and Penninx, W. (1994). Searches for millisecond pulsations in low-mass X-ray binaries, 2. ApJ, 435:362–371.

Verbunt, F., Bunk, W., Hasinger, G., and Johnston, H. M. (1995). The ROSAT XRT Sky Survey of X-ray sources in globular clusters. A&A, 300:732.

Verbunt, F. and Hut, P. (1987). The Globular Cluster Population of X-Ray Binaries. In Helfand, D. J. and Huang, J.-H., editors, *The Origin and Evolution of Neutron Stars*, volume 125 of *IAU Symposium*, page 187.

Verner, D. A., Ferland, G. J., Korista, K. T., and Yakovlev, D. G. (1996). Atomic Data for Astrophysics. II. New Analytic FITS for Photoionization Cross Sections of Atoms and Ions. ApJ, 465:487.

Voges, W., Aschenbach, B., Boller, T., Bräuninger, H., Briel, U., Burkert, W., Dennerl, K., Englhauser, J., Gruber, R., Haberl, F., Hartner, G., Hasinger, G., Kürster, M., Pfeffermann, E., Pietsch, W., Predehl, P., Rosso, C., Schmitt, J. H. M. M., Trümper, J., and Zimmermann, H. U. (1999). The ROSAT all-sky survey bright source catalogue. A&A, 349:389–405.

Warwick, R. S., Norton, A. J., Turner, M. J. L., Watson, M. G., and Willingale, R. (1988). A survey of the galactic plane with EXOSAT. MNRAS, 232:551–564.

Wijnands, R. and van der Klis, M. (1998). A millisecond pulsar in an X-ray binary system. Nature, 394:344–346.

Wilms, J., Allen, A., and McCray, R. (2000a). On the Absorption of X-Rays in the Interstellar Medium. ApJ, 542:914–924.

Wilms, J., Allen, A., and McCray, R. (2000b). On the Absorption of X-Rays in the Interstellar Medium. ApJ, 542:914–924.

Winkler, C., Courvoisier, T. J.-L., Di Cocco, G., Gehrels, N., Giménez, A., Grebenev, S., Hermsen, W., Mas-Hesse, J. M., Lebrun, F., Lund, N., Palumbo, G. G. C., Paul, J., Roques, J.-P., Schnopper, H., Schönfelder, V., Sunyaev, R., Teegarden, B., Ubertini, P., Vedrenne, G., and Dean, A. J. (2003a). The INTEGRAL mission. A&A, 411:L1–L6.

Winkler, C., Courvoisier, T. J.-L., Di Cocco, G., Gehrels, N., Giménez, A., Grebenev, S., Hermsen, W., Mas-Hesse, J. M., Lebrun, F., Lund, N., Palumbo, G. G. C., Paul, J., Roques, J.-P., Schnopper, H., Schönfelder, V., Sunyaev, R., Teegarden, B., Ubertini, P., Vedrenne, G., and Dean, A. J. (2003b). The INTEGRAL mission. A&A, 411:L1–L6.

Wood, K. S., Norris, J. P., Hertz, P., Vaughan, B. A., Michelson, P. F., Mitsuda, K., Lewin, W. H. G., van Paradijs, J., Penninx, W., and van der Klis, M. (1991). Searches for millisecond pulsations in low-mass X-ray binaries. ApJ, 379:295–309.

Woosley, S. E., Heger, A., Cumming, A., Hoffman, R. D., Pruet, J., Rauscher, T., Fisker, J. L., Schatz, H., Brown, B. A., and Wiescher, M. (2004). Models for Type I X-Ray Bursts with Improved Nuclear Physics. ApJS, 151:75–102.

Yan, Z., Lin, J., Yu, W., Zhang, W., and Zhang, H. (2015). A hard-to-soft state transition is going on in neutron star transient EXO 1745-248. *The Astronomer's Telegram*, 7430.

Yoshida, K., Mitsuda, K., Ebisawa, K., Ueda, Y., Fujimoto, R., and et al. (1993). Low state properties of the low-mass X-ray binary X1608-522 observed with GINGA. PASJ, 45:605–616.

Young, A. J., Fabian, A. C., Ross, R. R., and Tanaka, Y. (2001). A complete relativistic ionized accretion disc in Cygnus X-1. MNRAS, 325:1045–1052.

Zdziarski, A. A., Johnson, W. N., and Magdziarz, P. (1996). Broad-band γ-ray and X-ray spectra of NGC 4151 and their implications for physical processes and geometry. MNRAS, 283:193–206.

Zdziarski, A. A., Lubiński, P., and Smith, D. A. (1999). Correlation between Compton reflection and X-ray slope in Seyferts and X-ray binaries. MNRAS, 303:L11–L15.

Życki, P. T., Done, C., and Smith, D. A. (1999a). The 1989 May outburst of the soft X-ray transient GS 2023+338 (V404 Cyg). MNRAS, 309:561–575.

Życki, P. T., Done, C., and Smith, D. A. (1999b). The 1989 May outburst of the soft X-ray transient GS 2023+338 (V404 Cyg). MNRAS, 309:561–575.

List of Figures

List of Tables

Ringraziamenti

Desidero ringraziare la mia tutor professoressa Tiziana Di Salvo, per essere stata un continuo stimolo e per l'attenzione e la disponibilitá impagabile dimostratami per tutta la durata del dottorato. Grazie a lei per avermi messo a disposizione competenze senza cui non avrei potuto svolgere questo lavoro.

Ringrazio il prof. Rosario Iaria per aver seguito da vicino tutte le fasi del mio lavoro, apportando importanti contributi al mio bagaglio di conoscenze sugli oggetti compatti.

Un ringraziamento, inoltre, va al gruppo di Astrofisica delle Alte Energie dell'ICE di Barcellona, per la calorosa accoglienza e l'opportunitá datami di approfondire particolari aspetti del mio lavoro di tesi. Tra questi, un particolare ringraziamento va al dott. Diego Torres ed al dott. Alessandro Papitto.

Ringrazio gli amici e colleghi, ed in particolare Angelo, per l'attenzione e l'affetto dimostratomi specialmente nei momenti difficili, e per aver seguito con interesse gli sviluppi del mio lavoro.

Ultimo, ma non meno importante, ringrazio la mia famiglia per avermi dato la possibilitá di seguire gli studi universitari e per essermi stata sempre vicina moralmente e concretamente.